Title

Patterned electrical stimulation of primate retina for the development of retinal prostheses

Author

Jepson, Lauren Hruby

Publication Date

2012

UNIVERSITY OF CALIFORNIA, SAN DIEGO

Patterned Electrical Stimulation of Primate Retina for the Development of Retinal Prostheses

A dissertation submitted in partial satisfaction of the
requirements for the degree
Doctor of Philosophy

in

Bioengineering

by

Lauren Hruby Jepson

Committee in charge:

Professor Gabriel A. Silva, Chair
Professor E.J. Chichilnisky, Co-Chair
Professor Gert Cauwenberghs
Professor Todd P. Coleman
Professor Massimo Scanziani

2012

The dissertation of Lauren Hruby Jepson is approved, and it is acceptable in quality and form for publication on microfilm and electronically:

Co-Chair

Chair

University of California, San Diego

2012

DEDICATION

In Loving Memory of my Dad,
Mark R. Hruby, MD

TABLE OF CONTENTS

LIST OF FIGURES

ACKNOWLEDGEMENTS

First, I would like to thank my doctoral adviser, EJ Chichilnisky, for years of exactly the right amount of guidance–just enough to allow me to explore different research possibilities, while still always being accessible for input and advice. I also thank him for taking the risk of accepting a graduate student with little or no experience with electrophysiological recording or programming. Lastly, I would never have made it through my PhD without his constant and unwavering support and encouragement. I feel truly lucky to have had the privilege to work under the guidance of EJ for the past five years.

This work would not have been possible without the invaluable contributions of my coauthors, including many associated with the Santa Cruz Institute for Particle Physics at the University of California, Santa Cruz. Of special note, Pawel Hottowy designed and tested the electrical stimulation system that was crucial for all of the data presented in this thesis, as well as the Labview software required to run the stimulation and recording system and the core Matlab software to read and sort the electrical stimulation data. In addition, Pawel helped to run several of the early experiments using the system, and has provided valuable input on experiment planning and analysis throughout my thesis research. Keith Mathieson and Debbie Gunning fabricated the electrode arrays used in all of the electrical stimulation experiments, helped to train me in the use of the stimulation system, helped to install and debug the stimulation system at the Salk Institute, and provided assistance in several experiments. Debbie Gunning also hosted me for a series of experiments performed at UC Santa Cruz.

I would also like to thank the past and present fellow lab members of the Systems Neurobiology Laboratories at the Salk Institute for Biological studies, for patiently answering my endless stream of questions and lending a hand whenever possible. In particular, I would like to thank former post-doctoral fellow Chris Sekirnjak for initially teaching me how to perform electrical stimulation experiments, and for sharing his extensive knowledge of the retinal prosthesis field. Martin Greschner, Peter Li, and Jeff Gauthier all provided considerable support in Matlab programming, and Matlab software written by them was used at various points throughout my analysis. Fig. 2.1 was generated using a new spike-sorting analysis developed and performed by Martin Greschner.

Clare Hulse, our lab technician, provided essential experimental support and encouragement, particularly during primate experiments. She, along with undergraduate volunteer Gaby Cruz, also performed analysis of electrical stimulation data presented in Chapter 3. Matthew Grivich shared his extensive knowledge of all things related to the electronics and programming involved in running the stimulation and recording system, along with contributing to software development. Additional technical development was provided by Tomasz Fiutowski, Sergei Kachiguine, Andrzej Skoczen, and Alexander Sher. Access to primate retinas was provided by Howard Fox, Mike Taffe, Ed Callaway, John Reynolds, and Rich Krauzlis. Salk machinist Steve Barry provided much of the custom machined lab equipment used in our experiments.

Finally, I gratefully acknowledge funding provided by the NEI, Sanofi-Aventis, the Joseph Alexander Foundation, and the Charles Lee Powell Foundation.

Chapter 2, in full, is currently being prepared for submission for publication of the material. Jepson L.H., Hottowy P., Mathieson K., Gunning D.E., Dabrowski W., Litke A., Chichilnisky, E.J. The dissertation author was the primary investigator and author of this material.

Chapter 3, in part, is a reprint, with permission, of the published conference proceedings "Spatially patterned electrical stimulation of the retina for improved specificity." Jepson L.H., Hottowy P., Gunning D.E., Mathieson K., Dabrowski W., Litke A., and Chichilnisky, E.J. *Proceedings of the 5th International IEEE/EMBS Conference on Neural Engineering*, 2011 ©IEEE 2011. The dissertation author was the primary investigator and author of this paper.

Chapter 3, in part, is currently being prepared for submission for publication of the material. Jepson L.H., Hottowy P., Mathieson K., Gunning D.E., Dabrowski W., Litke A., Chichilnisky, E.J. The dissertation author was the primary investigator and author of this material.

VITA

2004	Systems Integration Intern, Beckman Coulter Inc., Chaska, MN
2005	B. S. in Biochemistry, University of St. Thomas, St. Paul, MN
2005-2006	Assistant Research Fellow, Otago University, Dunedin, New Zealand
2007-2012	Graduate Research Assistant, University of California, San Diego
2007-2009	Graduate Teaching Assistant, University of California, San Diego
2010	Summer Intern, Brain Corporation, San Diego, California
2012	Ph. D. in Bioengineering, University of California, San Diego

ABSTRACT OF THE DISSERTATION

Patterned Electrical Stimulation of Primate Retina for the Development of Retinal Prostheses

by

Lauren Hruby Jepson

Doctor of Philosophy in Bioengineering

University of California, San Diego, 2012

Professor Gabriel A. Silva, Chair
Professor E.J. Chichilnisky, Co-Chair

Epiretinal prostheses are designed to restore vision to people blinded by retinal degenerations, using electrical stimulation with an array of electrodes implanted on the surface of the retina to convey artificial visual signals to the brain. Current clinical prostheses provide limited visual function, in part because the activity that they generate is different from natural retinal responses to visual stimuli. An ideal retinal prosthesis would stimulate the retinal ganglion cells (RGCs) in a way that veridically recreates the precise, cell-type dependent spatiotemporal spiking patterns present in the retina. This requires RGC activation at the native temporal and spatial resolution of the retina.

We sought to better understand how electrical stimulation with high-density electrode arrays can be used to control RGC activity using an *in vitro* retina preparation to simultaneously stimulate and record from primate RGCs. The five numerically dominant RGC types, the ON and OFF midget, ON and OFF parasol, and small bistratified cells, could be activated to fire single, precisely-timed spikes using brief current pulses that fell within established safe charge density limits. Single-cell activation, which would prevent the simultaneous activation of different RGC types, was possible in roughly half of the tested RGCs.

We further investigated whether simultaneous patterned current injection through multiple electrodes could be used to improve spatial selectivity. The majority of RGC responses to simultaneous current injection through multiple electrodes could be described by a simple model in which currents from different electrodes combine linearly to produce RGC responses. Observed nonlinearities could be effectively captured by extending the model to include multiple regions of stimulus space, in which each region contained a different linear tradeoff between currents passed through the electrodes. The usefulness of the model for improving spatial selectivity was examined by using it to predict which combinations of currents would most selectively activate a cell. The selectivity of the pattern chosen using the model was much higher than with single-electrode stimulation, and was nearly identical to that of the optimal pattern. Collectively, these findings support the feasibility of using epiretinal stimulation to control retinal activity at or near its native spatial and temporal resolution, and suggest a strategy to improve spatial resolution beyond what can be achieved using individual electrodes.

Chapter 1

Introduction

1.1 Introduction to visual prostheses

Visual prostheses are designed to restore vision to patients blinded by disease or injury by recreating healthy light-driven neural activity in the remaining portion of the visual system. Typically, visual prostheses attempt to control neural activity using electrical pulses applied with implanted electrodes, although optogenetic (genetic manipulation that allows for control of neuronal activity with light) [1–3], neurotransmitter-based [4, 5], and photochemical [6, 7] control of retinal activity have been proposed recently as alternatives to electrical stimulation.

The use of electrical stimulation to produce visual sensations (phosphenes) was first demonstrated in 1755 by passing current through the eye of a blind man [8]. Early in the 20th century, a pair of neurosurgeons demonstrated that phosphenes could also be induced by electrically stimulating the visual cortex [9, 10]. Attempts at restoring vision using a chronic implant began in the 1960s, when an array of 80 electrodes was implanted onto the surface of a blind patient's visual cortex in the first chronic human experiment [11]. Serious limitations to the cortical approach, including the unpredictability of elicited phosphenes, the risk of inducing epileptic seizures, and surgical risks such as intracranial infection and hemorrhage [12], have led to the exploration of additional electrical stimulation targets in other parts of the visual system.

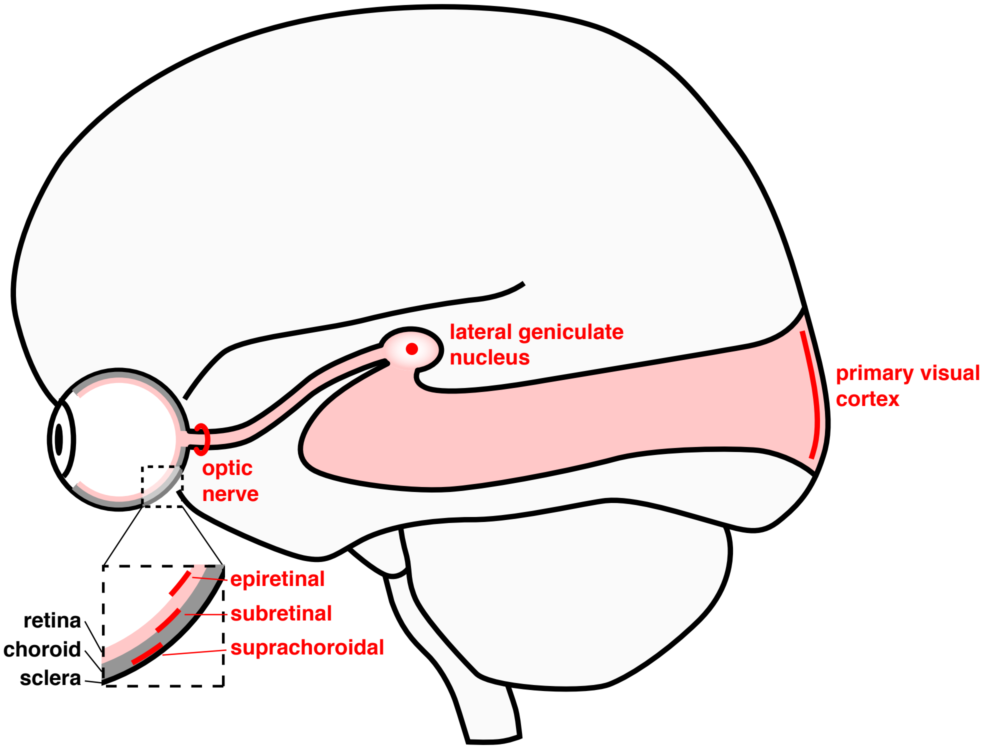

Figure 1.1: Anatomical locations being pursued as targets of visual prostheses. Within the eye, the structure targeted by electrical stimulation is the retina, a thin sheet of neural tissue that absorbs incoming light and performs initial processing of the visual input. Electrodes targeting the retina may be placed on the inner (epiretinal) or outer (subretinal) surface of the retina, or behind the choroid (suprachoroidal), the sheet of connective tissue that provides oxygen and nourishment to the outer portion of the retina. Outside of the eye, visual prostheses may target the optic nerve, which carries visual information from eye to brain; the lateral geniculate nucleus, the neural relay between the retina and the visual cortex; or the primary visual cortex, the earliest cortical area in the visual system.

1.2 Potential locations for visual prostheses

Stimulation sites currently being pursued in visual prosthesis development include the retina, optic nerve [13–17], lateral geniculate nucleus [18, 19] and visual cortex [12, 20–22], (Fig. 1.1). Within the retina, multiple electrode configurations are being investigated, including placement of electrodes between the outer retina and retinal pigment epithelium (subretinal) [23–25], on the inner surface of the retina (epiretinal) [26–30], or on the outer surface of the choroid (suprachoroidal) [31–34](Fig. 1.1). Each of these stimulation targets has inherent benefits and limitations, such as the degree and location of functional loss that can be tolerated by the prostheses and the complexity of visual encoding at different locations in the visual system. To allow for a degree of focus, the following discussion will be limited to epiretinal prostheses.

1.3 Background

1.3.1 Structure and function of the mammalian retina

Vision refers to the process of transforming the light that enters the eye into neural signals that result in the subjective experience of “seeing.” This process starts with retina, the thin sheet of neural tissue that lines the back of the eye. An image of the external world is focused by the optics of the eye onto the retina, where it is absorbed by the first neurons of the visual system: the photoreceptors (Fig. 1.2). These highly specialized sensory neurons transduce incoming light into neural signals that can be passed on to the retinal interneurons. The retinal interneurons, comprised of the horizontal, bipolar and amacrine cells, form the neural circuitry that processes the visual information captured by the photoreceptors and divides it into parallel pathways [35]. These processed visual signals are then integrated by the retinal ganglion cells (RGCs), which generate the retinal output in the form of patterns of action potentials [36]. The optic nerves, which are made up of the collection of RGC axons, transmit these spiking patterns from the retina to several targets in the brain [37], where they are further processed and ultimately lead to

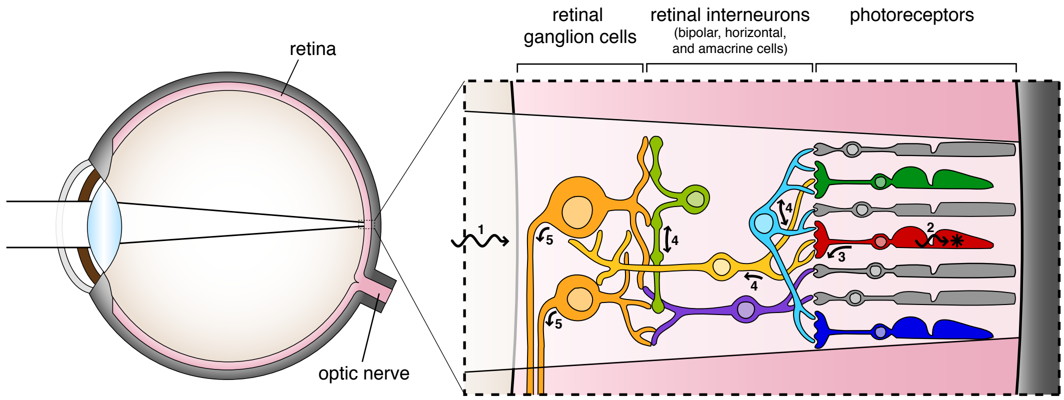

Figure 1.2: Overview of retinal anatomy and function. Light passes through the retina (1) and is absorbed by the photoreceptors (2), which transduce the light into a neural signal. This neural signal is then passed on to the retinal interneurons (3), which perform initial processing on the visual input (4). Finally, the processed visual information is integrated by the RGCs (5) and transmitted from the eye to the brain through the optic nerve.

visual perception.

1.3.2 Outer retinal degenerations are a target for retinal prostheses

A number of diseases can lead to complete or partial loss of vision through the impairment of structures in the visual system. For a visual prosthesis to be effective, both the neurons targeted by electrical stimulation and the neural structures that lie downstream in the visual system must retain the ability to transmit and process visual information. Epiretinal prostheses typically target the RGCs, although there is evidence that retinal interneurons are also activated by current clinical prostheses [38]. Therefore, the causes of blindness that are amenable to vision restoration with an epiretinal prostheses are diseases that primarily affect the photoreceptors, such as retinitis pigmentosa and age-related macular degeneration.

The cause of blindness in the majority of patients implanted with retinal prostheses to date is retinitis pigmentosa. Retinitis pigmentosa is actually not a single disease, but a collection of inherited diseases that are characterized by progressive degeneration of photoreceptors. Approximately 1 in 3700 people born in the United States is affected by retinitis pigmentosa [39]. The most common form of the disease manifests itself initially as “night blindness,” due to the death of the rods, the photoreceptor type responsible for vision under low-light conditions. Later, degeneration of the remaining photoreceptors in the peripheral regions of the retina lead to complete peripheral vision loss [40]. Finally, vision loss progresses to the central visual field, resulting in complete blindness.

A second retinal degenerative disease that is amenable to vision restoration with an epiretinal prostheses is age-related macular degeneration (AMD), the leading cause of new vision loss in the elderly population [41]. Like retinitis pigmentosa, this disease primarily affects the photoreceptors. However, because even patients severely affected by AMD typically retain some visual function in their peripheral retinas, it is unlikely that retinal prostheses will be used for the treatment of AMD until significant advancements in the quality of the restored vision have been demonstrated.

Although the retinal cells most severely affected in retinitis pigmentosa and AMD are the photoreceptors, other retinal cells are also affected. Upon the death of photoreceptors, significant rewiring of the remaining retinal cells occurs, including retraction and extension of neuronal processes and neuronal migration [42]. In addition, a fraction of the retinal interneurons and RGCs are lost. In retinitis pigmentosa, the percentage of RGCs remaining ranges from 20-75% [43–45], and in AMD, approximately 50-100% of RGCs remain [46]. Nevertheless, acute epiretinal stimulation studies and clinical trials of epiretinal prostheses have shown that the remaining RGCs are sufficient to generate visual perception.

1.4 Clinical epiretinal prostheses

1.4.1 Clinical outcomes to date

Work toward stimulation of the retina for sight restoration began in the late 1980s with the formation of three independent research teams in the United States [47]. The first acute tests of electrical stimulation applied by an epiretinal electrode were performed in the 1990s and revealed that epiretinal stimulation was capable of eliciting perception of localized phosphenes in patients blinded by retinal degeneration [48]. Since then, the field has grown rapidly, spawning a number of companies, consortia, and research laboratories across the globe dedicated to the development of retinal prostheses.

The company that has performed the most extensive clinical trials of epiretinal prosthesis to date is Second Sight Medical Products, Inc. In 2002, Second Sight began a clinical trial of their first generation device, the Argus I, which consists of an epiretinal array of 16 platinum electrodes, spaced 800 μm apart and either 260 or 520 μm in diameter, connected by a cable to electronics encased outside the eye [49]. An external camera mounted on a pair of glasses captures video of the patient's surroundings, which is then converted into a series of electrical stimulation commands by a portable processing unit and wirelessly transmitted to the implant. In total, 6 patients with advanced retinal degeneration were chronically implanted with the Argus I. All patients perceived discrete phosphenes upon injection of current pulses through individual electrodes of the implant [50], and patients tested for performance on simple visual tasks, such as detecting the orientation of a visual stimulus [51] and discriminating between a set of simple objects [52], performed better than chance.

Based on the success of these initial implants, Second Sight developed a second generation implant, the Argus II, increasing the number of electrodes to 60, slightly decreasing the electrode size to 200 μm in diameter and decreasing the center-to-center electrode spacing to 575 μm [53]. The company launched a clinical trial in 2006 to test the safety and efficacy of the Argus II, and have since implanted the prosthesis in 32 patients in several locations in the US, Europe and Mexico [54, 55]. Results to date have shown significant improvements in the ability of patients to perform a range of visual tasks, from tracing simple outlines on a computer screen [26] to walking to a door across a room [54]. Two of the highest-performing patients were even capable of reading short (4-word) sentences presented in a large font (4.5 cm) on an LCD screen [56]. In 2011, the Argus II became the first retinal prosthesis to receive CE Marking, allowing it to be sold in

Europe as a medical device [57]. Second Sight has plans to create a third-generation prosthesis with at least 250 electrodes.

Two other groups have launched less extensive clinical trials of epiretinal prostheses. A 25-electrode prosthesis developed by a group of researchers in Germany, the EPIRET3, was tested in a 4-week clinical trial in 2006. Four of six patients receiving the EPIRET3 implant consistently reported experiencing visual sensations upon stimulation with safe levels of current, and three were capable of distinguishing between simple stimulation patterns, such as simultaneous stimulation with sets of electrodes oriented in different directions [28].

Separately, the German company Intelligent Medical Implants, GmbH, developed an epiretinal implant with 49 electrode that was implanted in 7 patients. Informal tests suggested that implant recipients were capable of discriminating between current pulses injected through different electrodes and between stimulation with different patterns of electrodes [58, 59], although the details of the discrimination tasks have not been published.

1.4.2 Shortcomings of clinical epiretinal prostheses

While results of early clinical trials confirm that some degree of visual function may be restored using epiretinal stimulation, the quality of the restored vision achieved thus far has been relatively rudimentary. Even in the best performing subjects implanted with the Argus II, the clinical prosthesis with the best results to date, reading a single 4-letter word displayed in large lettering required 20-40 seconds on average after 2 months of training [56]. In addition, the visual percepts generated by epiretinal stimulation have been highly inconsistent, varying in shape, color and transience between patients [28, 53]) and even between different stimulation electrodes in a single patient [60, 61].

The most likely cause of the failure to recreate consistent, high quality vision is the fact that little attempt is made at mimicking the natural neural signals that encode visual information in the retina. Most publications describing the performance of patients on camera-based visual tasks omit information about how the video is transformed into an electrical stimulus. However, publications describing percepts elicited by directly-controlled electrical stimuli suggest that very simple schemes are used, such as encoding image brightness as variations in pulse amplitude or frequency [61, 62]. In addition, due to the large size of the stimulation electrodes in current clinical implants relative to the size and density of the targeted RGCs, each current pulse is likely to elicit neural responses in hundreds of RGCs simultaneously, generating a retinal output that is very different from the complex spatiotemporal spiking patterns that carry visual information from retina to brain in a healthy visual system (Fig. 1.3, discussed further in Section 1.5.2).

1.5 Proposal for a high-resolution epiretinal prosthesis

An ideal retinal prosthesis would be capable of veridically recreating the natural RGC spiking patterns generated by a healthy retina, replacing the function of the bypassed photoreceptors and retinal circuitry. Successful transference of information about a visual scene to a patient's visual system can be broken down into two main challenges: translating the visual information captured by a camera into the native spiking output of healthy retina (encoding), and manipulating the activity of the patient's RGCs to mimic this spiking output (transmission).

1.5.1 Encoding

In order to mimic the natural RGC activity elicited by a particular visual scene, the processing normally provided by the retinal circuitry must be applied to the captured video before the visual information is transmitted to the RGCs. Essentially, this involves predicting, given a particular visual scene, the resulting pattern of RGC spikes of a healthy retina. Several computational models have been constructed in an attempt to do this [63–70], and some have been shown to predict healthy RGC responses with high fidelity. However, these models are often validated on simplistic visual stimuli. Further research is required to establish optimal models that perform well for more natural visual stimuli. In addition, models of retinal processing typically only emulate a subset of the total number of RGC types that exist in the primate retina, so complete replication of the retinal output will require the remaining RGC types to be characterized and modeled. Although the challenge of mimicking the encoding naturally performed by a healthy retina is critical to recreating natural RGC activity with an epiretinal prosthesis, it is not the focus of the research presented in this thesis.

1.5.2 Transmission

Once the appropriate RGC activity pattern of the retina has been determined for a particular visual stimulus, the prosthesis must be able to induce this activity in the population of RGCs in the patient's retina. This requires a method for controlling the activity of RGCs. The standard method for modulating neural activity with clinical devices is electrical stimulation using implanted electrodes. Pulses of current delivered through these electrodes alter neural activity by establishing a local electrical field in the surrounding tissue, which generates currents within and across the membranes of nearby neurons, causing neural excitation or suppression [71, 72]. Electrical stimulation has been used successfully for decades in a variety of neural prostheses such as cochlear implants [73] and deep brain stimulators [74]. However, no existing neural stimulation devices have achieved the spatial resolution of neural control that would be required to veridically recreate the natural activity of the retina.

Transmission: spatial resolution

Unlike other neural prostheses, restoration of high-resolution vision will require an unprecedented level of spatial resolution of neuronal activation. Ideally, the prosthesis would be able to independently control the activity of each RGC, rather than simultaneously activating hundreds or more neurons, as is likely the case in other neural prostheses and in current clinical epiretinal prosthesis. Targeting individual RGCs has the obvious advantage of increasing spatial resolution of the artificial vision provided by a retinal prosthesis. However, an equally important motivation to achieve single-cell activation is the fact that RGCs are not comprised of a homogenous population of cells, but rather several distinct spatially-intermixed types. At least 17 morphologically distinct RGC types exist in the primate retina [37], each encoding different information about a visual scene [36]. Thus, the activity of the RGCs is not a simple reflection of the visual scene, but rather several parallel representations, each conveyed to a distinct set of targets in the brain by a particular RGC type. For example, one RGC type may primarily encode information about local contrast in the visual scene, whereas a different RGC type primarily encodes color information.

The fact that the different cell types encode different aspects of visual information is reflected in their distinct response to the same visual stimulus. Figure 1.3 shows the responses of the four numerically dominant primate RGC types to repeated application of a simple visual stimulus: step increments and decrements in light intensity. The ON midget and ON parasol ganglion cells, as their names suggest, respond preferentially to the light increments, whereas the OFF midget and OFF parasol ganglion cells responds more strongly to the decrements. The responses of the different RGC types can be further distinguished by their transience: the ON and OFF midget ganglion cells exhibit sustained responses to the light steps, while the ON and OFF parasol ganglion cells respond most vigorously to the onset of the light steps [75, 76]).

Thus, to reproduce the natural retinal output with a epiretinal prosthesis, different patterns of activity must be induced in different RGC types. This is particularly difficult because the RGCs of different types are spatially intermixed in the retina. Figure 1.4 depicts the triangulated cell body location of each of the RGCs in the five highest-density cell types in a single piece of primate retina, based on a single electrophysiological recording, illustrating this spatial intermixing. Simultaneous activation of multiple neighboring RGCs with the same electrical stimulus is likely to generate nearly identical temporal patterns of spikes in the RGCs of many different types rather than the distinct cell type-specific temporal patterns (Fig. 1.3) present in natural responses. These unnatural electrically-elicited activity patterns would preclude transmission of distinct aspects of information contained

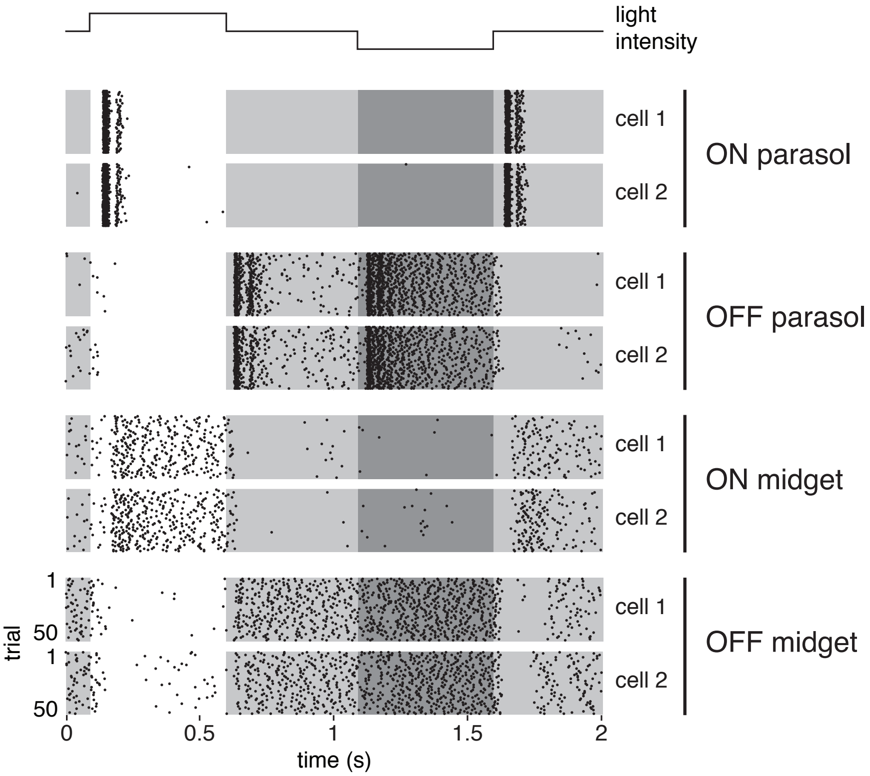

Figure 1.3: Distinct responses of different primate RGC types to the same visual stimulus. Raster plots show the spike times of each example RGC across fifty repetitions of step increments and decrements in full-field light intensity. Two example cells from each of the four numerically dominant primate RGC types are shown. All RGCs were simultaneously recorded using a multi-electrode array.

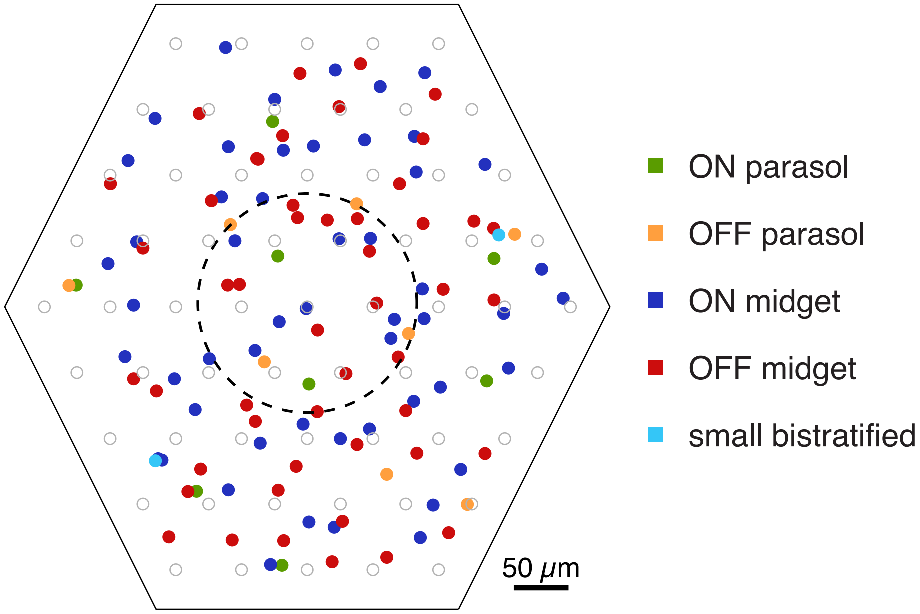

Figure 1.4: Approximate cell body location of each RGC within the five highest-density primate RGC types. Each dot represents a single RGC soma, colored according to cell type. Open grey circles show position of electrodes of the multi-electrode array. Dashed circle depicts relative size of a single electrode in the current generation Second Sight epiretinal prosthesis, the Argus II. Cell body locations are estimated from the center of mass of the electrodes recording large somatic voltage fluctuations.

in the visual scene that would normally be encoded by the distinct RGC types. Therefore, discrimination of any details of the scene beyond general spatial location would be difficult using electrodes and stimulation patterns that are unable to target individual cells, such as those used by current clinical epiretinal prostheses (Fig. 1.4 dashed outline).

1.6 Thesis scope

The primarily goals of this thesis are to gain a better understanding of how primate RGCs respond to epiretinal electrical stimulation, and to explore the potential of using spatial patterns of current injection to improve the spatial selectivity of activation. An *in vitro* preparation of a living patch of primate retina placed on an array of electrodes was used as a model of the interface between epiretinal prosthesis and retina. This preparation allowed us to inject various patterns of current pulses and simultaneously measure the responses of RGCs. The electrode diameter and pitch of the arrays used in this work were chosen to be roughly an order of magnitude smaller than those of current clinical prosthesis, in the anticipation that electrode arrays of this density will be required to approach the single-cell spatial resolution necessary to veridically recreate the natural retinal output.

The first aim of this thesis work is to characterize the response properties of the major cell types in the primate retina. The ON and OFF midget, ON and OFF parasol, and small bistratified cells, which together comprise roughly 75% of the total number of primate RGCs [37] were examined in terms of their sensitivity, response timing, and spatial selectivity. The second aim was to investigate the potential of using spatial patterns of current injection to improve spatial selectivity of RGC activation. To this end, responses to current pulses injected through multiple electrodes in different combinations of pulse amplitude and polarity were measured, and an empirical model that describes how currents combine to generate RGC responses was developed and tested.

Acknowledgments

I would like to acknowledge current and former members of the Systems Neurobiology Laboratories, EJ Chichilnisky lab at the Salk Institute of Biological studies for data used to generate Fig. 1.3 and Fig. 1.4, and Martin Greschner for assistance with the Matlab code used to generate the figures.

1.7 References

[1] Busskamp, V. and Roska, B., 2011. Optogenetic approaches to restoring visual function in retinitis pigmentosa. *Current Opinion in Neurobiology.*

[2] Greenberg, K., Pham, A., and Werblin, F., 2011. Differential targeting of optical neuromodulators to ganglion cell soma and dendrites allows dynamic control of center-surround antagonism. *Neuron*, 69:713–720.

[3] Gu, L., Shivalingaiah, S., Ficinski, M., and Wong, E., 2012. Non-viral delivery and optimized optogenetic stimulation of retinal ganglion cells led to behavioral restoration of vision. *precedingsnaturecom.*

[4] Iezzi, R., Finlayson, P., Xu, Y., and Katragadda, R., 2009. Microfluidic neurotransmiter-based neural interfaces for retinal prosthesis. *Conf Proc IEEE Eng Med Biol Soc*, 2009:4563–4565.

[5] Finlayson, P. and Iezzi, R., 2010. Glutamate stimulation of retinal ganglion cells in normal and s334ter-4 rat retinas: a candidate for a neurotransmitter-based retinal prosthesis. *Investigative Ophthalmology & Visual Science*, 51:3619–3628.

[6] Polosukhina, A., Litt, J., Tochitsky, I., and Nemargut, J., 2012. Photochemical Restoration of Visual Responses in Blind Mice. *Neuron.*

[7] Greenbaum, E. and Evans, B., 2011. Synthetic Chromophores and Neural Stimulation of the Visual System. *Visual Prosthetics: Physiology, Bioengineering and Rehabilitation*, page 193.

[8] LeRoy, C., 1755. O lon rend compte de quelques tentatives que lon a faites pour gurir plusieurs maladies par llectricit. *Hist Acad Roy Sciences (Paris), Mmoire Math Phys*, 60:87–95.

[9] Foerster, O., 1929. Beitrage zur pathophysiologie der sehbahn und der spehsphare. *J Psychol Neurol*, 39:435–463.

[10] Krause, F., 1924. Die Sehbahn in chirurgischer Beziehung und die faradische Reizung des Sehzentrums. *Journal of Molecular Medicine*, 3:1260–1265.

[11] Brindley, G. and Lewin, W., 1968. The sensations produced by electrical stimulation of the visual cortex. *The Journal of physiology*, 196:479–493.

[12] Normann, R., Greger, B., House, P., Romero, S., Pelayo, F., and Fernandez, E., 2009. Toward the development of a cortically based visual neuroprosthesis. *Journal of neural engineering*, 6:035001.

[13] Brelen, M., Duret, F., Grard, B., Delbeke, J., and Veraart, C., 2005. Creating a meaningful visual perception in blind volunteers by optic nerve stimulation. *Journal of neural engineering*, 2:S22.

[14] Sakaguchi, H., Kamei, M., and Nishida, K., 2012. Implantation of a newly developed direct optic nerve electrode device for artificial vision in rabbits. *Journal of Artificial* .

[15] Wang, K., Li, X., Li, X., Pei, W., Chen, H., and Dong, J., 2011. Efficacy and reliability of long-term implantation of multi-channel microelectrode arrays in the optical nerve sheath of rabbit eyes. *Vision research*.

[16] Wu, K., Zhang, C., Huang, W., Li, L., and Ren, Q., 2010. Current research of C-Sight visual prosthesis for the blind. *Conf Proc IEEE Eng Med Biol Soc*, 2010:5875–5878.

[17] Sun, J., Lu, Y., Cao, P., Li, X., Cai, C., Chai, X., Ren, Q., and Li, L., 2011. Spatiotemporal properties of multipeaked electrically evoked potentials elicited by penetrative optic nerve stimulation in rabbits. *Investigative Ophthalmology & Visual Science*, 52:146–154.

[18] Pezaris, J. and Reid, R., 2007. Demonstration of artificial visual percepts generated through thalamic microstimulation. *Proceedings of the National Academy of Sciences*, 104:7670.

[19] Panetsos, F., Sanchez-Jimenez, A., Cerio, E., Diaz-Guemes, I., and Sanchez, F., 2011. Consistent phosphenes generated by electrical microstimulation of the visual thalamus. An experimental approach for thalamic visual neuroprostheses. *Front Neurosci*, 5:84.

[20] Chowdhury, V., Morley, J., and Coroneo, M., 2004. Surface stimulation of the brain with a prototype array for a visual cortex prosthesis. *Journal of Clinical Neuroscience*, 11:750–755.

[21] Bradley, D., Troyk, P., Berg, J., Bak, M., Cogan, S., Erickson, R., Kufta, C., Mascaro, M., McCreery, D., and Schmidt, E., 2005. Visuotopic mapping through a multichannel stimulating implant in primate V1. *Journal of neurophysiology*, 93:1659–1670.

[22] Torab, K., Davis, T., Warren, D., House, P., Normann, R., and Greger, B., 2011. Multiple factors may influence the performance of a visual prosthesis based on intracortical microstimulation: nonhuman primate behavioural experimentation. *Journal of Neural Engineering*, 8:035001.

[23] Zrenner, E., Bartz-Schmidt, K., Benav, H., Besch, D., Bruckmann, A., Gabel, V., Gekeler, F., Greppmaier, U., Harscher, A., and Kibbel, S., 2011. Subretinal electronic chips allow blind patients to read letters and combine them to words. *Proceedings of the Royal Society B: Biological Sciences*, 278:1489–1497.

[24] Mathieson, K., Loudin, J., Goetz, G., and Huie, P., 2012. Photovoltaic retinal prosthesis with high pixel density. *Nature Photonics*.

[25] Rizzo, J.r., Shire, D., Kelly, S., Troyk, P., Gingerich, M., McKee, B., Priplata, A., Chen, J., Drohan, W., Doyle, P., Mendoza, O., Theogarajan, L., Cogan, S., and Wyatt, J., 2011. Overview of the boston retinal prosthesis: challenges and opportunities to restore useful vision to the blind. *Conf Proc IEEE Eng Med Biol Soc*, 2011:7492–7495.

[26] Barry, M. and Dagnelie, G., 2012. Use of the Argus II Retinal Prosthesis to Improve Visual Guidance of Fine Hand Movements. *Investigative Ophthalmology & Visual Science*, 53.

[27] Keserue, M., Feucht, M., Bornfeld, N., Laube, T., Walter, P., Roessler, G., Velikay-Parel, M., Hornig, R., and Richard, G., 2012. Acute electrical stimulation of the human retina with an epiretinal electrode array. *Acta Ophthalmologica*.

[28] Klauke, S., Goertz, M., Rein, S., Hoehl, D., Thomas, U., Eckhorn, R., Bremmer, F., and Wachtler, T., 2011. Stimulation with a wireless intraocular epiretinal implant elicits visual percepts in blind humans. *Investigative Ophthalmology & Visual Science*, 52:449–455.

[29] Abramian, M., Lovell, N., Morley, J., Suaning, G., and Dokos, S., 2011. Activation of retinal ganglion cells following epiretinal electrical stimulation with hexagonally arranged bipolar electrodes. *Journal of Neural Engineering*, 8:035004.

[30] Hadjinicolaou, A., Leung, R., Garrett, D., and Ganesan, K., 2012. Electrical stimulation of retinal ganglion cells with diamond and the development of an all diamond retinal prosthesis. *Biomaterials*.

[31] Fujikado, T., Kamei, M., Sakaguchi, H., Kanda, H., Morimoto, T., Ikuno, Y., Nishida, K., Kishima, H., Maruo, T., and Konoma, K., 2011. Testing of semichronically implanted retinal prosthesis by suprachoroidal-transretinal stimulation in patients with retinitis pigmentosa. *Investigative Ophthalmology & Visual Science*, 52:4726–4733.

[32] Morimoto, T., Kamei, M., Nishida, K., Sakaguchi, H., Kanda, H., Ikuno, Y., Kishima, H., Maruo, T., Konoma, K., and Ozawa, M., 2011. Chronic Implantation of Newly Developed Suprachoroidal-Transretinal Stimulation Prosthesis in Dogs. *Investigative Ophthalmology & Visual Science*, 52:6785–6792.

[33] Cicione, R., Shivdasani, M., Fallon, J., Luu, C., Allen, P., Rathbone, G., Shepherd, R., and Williams, C., 2012. Visual cortex responses to suprachoroidal electrical stimulation of the retina: effects of electrode return configuration. *J Neural Eng*, 9:036009.

[34] Wong, Y., Chen, S., Seo, J., Morley, J., Lovell, N., and Suaning, G., 2009. Focal activation of the feline retina via a suprachoroidal electrode array. *Vision research*, 49:825–833.

[35] Masland, R., 2001. The fundamental plan of the retina. *Nat Neurosci*, 4:877–886.

[36] Field, G. and Chichilnisky, E., 2007. Information processing in the primate retina: circuitry and coding. *Annu Rev Neurosci*, 30:1–30.

[37] Dacey, D., 2004. Origins of perception: retinal ganglion cell diversity and the creation of parallel visual pathways. In M.S. Gazzaniga, editor, The Cognitive Neurosciences, pages 281–301. MIT Press, Cambridge, MA.

[38] Chen, S., Mahadevappa, M., Roizenblatt, R., Weiland, J., and Humayun, M., 2006. Neural responses elicited by electrical stimulation of the retina. *Trans Am Ophthalmol Soc*, 104:252–259.

[39] Margalit, E. and Sadda, S., 2003. Retinal and optic nerve diseases. *Artificial organs*, 27:963–974.

[40] Hamel, C., 2006. Retinitis pigmentosa. *Orphanet J Rare Dis*, 1:40.

[41] Gehrs, K., Anderson, D., Johnson, L., and Hageman, G., 2006. Age-related macular degeneration–emerging pathogenetic and therapeutic concepts. *Ann Med*, 38:450–471.

[42] Jones, B. and Marc, R., 2005. Retinal remodeling during retinal degeneration. *Exp Eye Res*, 81:123–137.

[43] Humayun, M.S., Prince, M., de Juan, E., J., Barron, Y., Moskowitz, M., Klock, I.B., and Milam, A.H., 1999. Morphometric analysis of the extramacular retina from postmortem eyes with retinitis pigmentosa. *Invest Ophthalmol Vis Sci*, 40:143–148.

[44] Stone, J.L., Barlow, W.E., Humayun, M.S., de Juan, E.J., and Milam, A., 1992. Morphometric analysis of macular photoreceptors and ganglion cells in retinas with retinitis pigmentosa. *Arch Ophthalmol*, 110:1634–1639.

[45] Santos, A., Humayun, M.S., de Juan, E., J., Greenburg, R.J., Marsh, M.J., Klock, I.B., and Milam, A.H., 1997. Preservation of the inner retina in retinitis pigmentosa. A morphometric analysis. *Arch Ophthalmol*, 115:511–515.

[46] Medeiros, N. and Curcio, C., 2001. Preservation of ganglion cell layer neurons in age-related macular degeneration. *Investigative ophthalmology & visual science*, 42:795–803.

[47] Rizzo, J., Wyatt, J., Humayun, M., de Juan, E., Liu, W., Chow, A., Eckmiller, R., Zrenner, E., Yagi, T., and Abrams, G., 2001. Retinal prosthesis: an encouraging first decade with major challenges ahead. *Ophthalmology*, 108(1):13.

[48] Humayun, M.S., de Juan, E., J., Dagnelie, G., Greenberg, R.J., Propst, R.H., and Phillips, D.H., 1996. Visual perception elicited by electrical stimulation of retina in blind humans. *Arch Ophthalmol*, 114:40–46.

[49] Humayun, M., Weiland, J.D., Fujii, G.Y., Greenberg, R.J., Williamson, R., Little, J., Mech, B., Cimmarusti, V., Van, Boemel, G., Dagnelie, G., and deJuan, Jr., E., 2003. Visual perception in a blind subject with a chronic microelectronic retinal prosthesis. *Vision Research*, 43:2573–2581.

[50] de Balthasar, C., Patel, S., Roy, A., Freda, R., Greenwald, S., Horsager, A., Mahadevappa, M., Yanai, D., McMahon, M., Humayun, M., Greenberg, R., Weiland, J., and Fine, I., 2008. Factors affecting perceptual thresholds in epiretinal prostheses. *Invest Ophthalmol Vis Sci*, 49:2303–2314.

[51] Caspi, A., Dorn, J., McClure, K., Humayun, M., Greenberg, R., and McMahon, M., 2009. Feasibility study of a retinal prosthesis: spatial vision with a 16-electrode implant. *Arch Ophthalmol*, 127:398–401.

[52] Yanai, D., Weiland, J., Mahadevappa, M., Greenberg, R., Fine, I., and Humayun, M., 2007. Visual performance using a retinal prosthesis in three subjects with retinitis pigmentosa. *Am J Ophthalmol*, 143:820–827.

[53] Fornos, A., Sommerhalder, J., Cruz, L.D., Sahel, J., Mohand-Said, S., Hafezi, F., and Pelizzone, M., 2012. Temporal Properties of Visual Perception on Electrical Stimulation of the Retina. *Investigative Ophthalmology & Visual Science*, 53:2720–2731.

[54] Humayun, M., Dorn, J., da Cruz, L., Dagnelie, G., Sahel, J., Stanga, P., Cideciyan, A., Duncan, J., Eliott, D., Filley, E., Ho, A.C., Santos, A., Safran, A., Arditi, A., Del Priore, L., and Greenberg, R., 2012. Interim results from the international trial of Second Sight's visual prosthesis. *Ophthalmology*, 119:779–788.

[55] Ahuja, A., Dorn, J., Caspi, A., McMahon, M., Dagnelie, G., Dacruz, L., Stanga, P., Humayun, M., and Greenberg, R., 2011. Blind subjects implanted with the Argus II retinal prosthesis are able to improve performance in a spatial-motor task. *Br J Ophthalmol*, 95:539–543.

[56] Sahel, J., da, Cruz, L., Hafezi, F., Stanga, P., Merlini, F., Coley, B., and Greenberg, R., 2011. Subjects Blind From Outer Retinal Dystrophies Are Able To Consistently Read Short Sentences Using The ArgusTM II Retinal Prosthesis System. *ARVO Meeting Abstracts*, 52:3420.

[57] Weiland, J., Cho, A., and Humayun, M., 2011. Retinal Prostheses: Current Clinical Results and Future Needs. *Ophthalmology*, 118:2227–2237.

[58] Richard, G., Hornig, R., Keserue, M., and Feucht, M., 2007. Chronic Epiretinal Chip Implant in Blind Patients With Retinitis Pigmentosa: Long-Term Clinical Results. *ARVO Meeting Abstracts*, 48:666.

[59] Richard, G., Keserue, M., Feucht, M., Post, N., and Hornig, R., 2008. Visual Perception After Long-Term Implantation of a Retinal Implant. *ARVO Meeting Abstracts*, 49:1786.

[60] Nanduri, D., Humayun, M., Greenberg, R., McMahon, M., and Weiland, J., 2008. Retinal prosthesis phosphene shape analysis. *Conf Proc IEEE Eng Med Biol Soc*, pages 1785–1788.

[61] Nanduri, D., Fine, I., Horsager, A., Boynton, G., Humayun, M., Greenberg, R., and Weiland, J., 2012. Frequency and amplitude modulation have different effects on the percepts elicited by retinal stimulation. *Invest Ophthalmol Vis Sci*, 53:205–214.

[62] Greenwald, S., Horsager, A., Humayun, M., Greenberg, R., McMahon, M., and Fine, I., 2009. Brightness as a function of current amplitude in human retinal electrical stimulation. *Invest Ophthalmol Vis Sci*, 50:5017–5025.

[63] Pillow, J., Paninski, L., Uzzell, V., Simoncelli, E., and Chichilnisky, E., 2004. Accounting for timing and variability of retinal ganglion cell light responses with a stochastic integrate-and-fire model. *Soc Neurosci Abstr*, 30.

[64] Pillow, J., Paninski, L., Uzzell, V., Simoncelli, E., and Chichilnisky, E., 2005. Prediction and decoding of retinal ganglion cell responses with a probabilistic spiking model. *J Neurosci*, 25:11003–11013.

[65] Pillow, J., Shlens, J., Paninski, L., Sher, A., Litke, A., Chichilnisky, E., and Simoncelli, E., 2008. Spatio-temporal correlations and visual signalling in a complete neuronal population. *Nature*, 454:995–999.

[66] Keat, J., Reinagel, P., Reid, R., and Meister, M., 2001. Predicting every spike: a model for the responses of visual neurons. *Neuron*, 30:803–817.

[67] Enroth-Cugell, C. and Robson, J., 1966. The contrast sensitivity of retinal ganglion cells of the cat. *J Physiol*, 187:517–552.

[68] Enroth-Cugell, C., Robson, J., Schweitzer-Tong, D., and Watson, A., 1983. Spatio-temporal interactions in cat retinal ganglion cells showing linear spatial summation. *J Physiol*, 341:279–307.

[69] Victor, J., 1987. The dynamics of the cat retinal X cell centre. *J Physiol*, 386:219–246.

[70] Chichilnisky, E., 2001. A simple white noise analysis of neuronal light responses. *Network: Computation in Neural Systems*, 12:199–213.

[71] Rattay, F., 1999. The basic mechanism for the electrical stimulation of the nervous system. *Neuroscience*, 89:335–346.

[72] McIntyre, C. and Grill, W., 1999. Excitation of central nervous system neurons by nonuniform electric fields. *Biophys J*, 76:878–888.

[73] Shannon, R., 2012. Advances in auditory prostheses. *Curr Opin Neurol*, 25:61–66.

[74] Fasano, A., Daniele, A., and Albanese, A., 2012. Treatment of motor and non-motor features of Parkinson's disease with deep brain stimulation. *Lancet Neurol*, 11:429–442.

[75] Wandell, B., 1995. Foundations of vision. Sinauer, Sunderland, MA.

[76] Rodieck, R., 1998. The first steps in seeing. Sinauer, Sunderland, MA.

Chapter 2

Electrical stimulation of parallel pathways in the primate retina

Abstract

Electrical stimulation of retinal neurons with an advanced retinal prosthesis may eventually provide high resolution artificial vision to the blind. However, the success of future prostheses depends on the ability to activate the major parallel visual pathways of the human visual system. Electrical stimulation of the five numerically dominant retinal ganglion cell types was investigated by simultaneous stimulation and recording of isolated macaque retina, which is highly homologous to the human retina, using multi-electrode arrays. ON and OFF midget, ON and OFF parasol, and small bistratified ganglion cells could all be activated directly to fire a single spike with sub-millisecond latency, using brief pulses of current within established safety limits. Thresholds for electrical stimulation were similar in all five cell types. In many cases, a single cell could be specifically activated without activating neighboring cells of the same type or other types. These findings support the feasibility of direct electrical stimulation of the major visual pathways at or near their native spatial and temporal resolution.

2.1 Introduction

Retinal prostheses have the potential to restore useful visual function to people blinded by diseases such as retinitis pigmentosa and age-related macular degeneration. In advanced stages of disease, photoreceptors degenerate but many other retinal neurons remain, notably a significant fraction of the retinal ganglion cells (RGCs) that normally transmit visual signals to the brain [1, 2]. Thus, vision could in principle be restored in these patients by electrically stimulating the remaining RGCs with an array of electrodes, in a manner that mimics the signals that a healthy retina would transmit to the brain. Indeed, clinical trials with prototype epiretinal prostheses have shown that electrical stimulation based on video captured by an external camera can induce artificial visual percepts and allow patients to perform simple visual tasks [3]. However, it is still unknown exactly what retinal activity is evoked by epiretinal stimulation and how this activity can be harnessed to produce high resolution visual signals in the parallel pathways of the human visual system.

Ideally, an epiretinal prosthesis would recreate the healthy RGC response to a visual scene at the native spatial and temporal precision of RGCs. A critical first step is to understand how different types of RGCs respond to electrical stimulation. This is important because the primate retina contains multiple morphologically distinct RGC types, each of which sends distinct visual information to a distinct set of targets in the brain [4]. To date, the only primate RGC types that have been shown to respond to epiretinal stimulation are the ON and OFF parasol cells [5], which comprise approximately 16% of the population. Therefore, it is unclear whether electrical stimulation can be used to create a more complete visual signal in the output of the retina. In particular, different RGC types could be differentially sensitive to electrical stimulation, a possibility which is supported by differences in the sensitivity of distinct rabbit RGC types [6], as well as differences in intrinsic electrical properties [7, 8] and morphology [9, 10] between RGC types in several species. In addition to the ON and OFF parasol cells, three cell types of particular importance in the primate retina are the ON and OFF midget cells, which are responsible for high-acuity vision and make up roughly half of the total RGC population, and the small bistratified cells (SBCs), which encode blue-yellow color information. A unified understanding of the responses to electrical stimulation of all five major RGC types, which together make up approximately 75% of primate RGCs [4], is essential for the design of retinal prostheses capable of mediating advanced artificial vision.

We probed the properties of the five major cell types by simultaneous recording and electrical stimulation of isolated primate retina using multi-electrode arrays. The results reveal that it is possible to directly stimulate ON and OFF midget, ON and OFF parasol and small bistratified RGCs using approximately 15 μm diameter electrodes with current pulses in a safe charge density range. RGCs from all five cell types exhibited similar sensitivity to brief current pulses, responding with a single, precisely timed spike, suggesting that the neural code of the retina can be reproduced with high fidelity. By recording simultaneously from midget and parasol cells while targeting midget cells for stimulation, we show that single-cell specificity in the highest density cell types is achievable in many cases. Thus, in principle it is possible to safely electrically activate RGCs in the high-resolution visual pathways at their native spatial and temporal resolution.

2.2 Methods

2.2.1 Experimental setup

Primate retinas were isolated and mounted on an array of electrodes as described previously [5, 11]. Briefly, eyes were removed from macaque monkeys (*Macaca mulatta*) that were terminally anesthetized in the course of other experiments. The vitreous and anterior portion of the eye were removed immediately in room light and the eye cup was stored in darkness in warm, oxygenated, bicarbonate-buffered Ames' solution (Sigma, St. Louis, MO). A 1-2 mm diameter segment of retina was isolated and placed RGC-side down on a custom multi-electrode array and held in place with a dialysis membrane positioned against the photoreceptor side. Data reported in this paper were compiled from 12 retinal preparations with eccentricities ranging from 7 to 15 mm taken from 11 macaque monkeys.

Dissections were performed primarily under infrared illumination, with a brief period (<5 minutes) of dim red illumination while mounting the array in the stimulation and recording system. Once mounted, the preparation was continuously superfused with oxygenated, bicarbonate-buffered Ames' solution maintained at ∼33°C, pH 7.4. The mean spike rate of the preparation was allowed to stabilize before commencing data collection. Voltage was recorded at 20 kHz on all electrodes, bandpass filtered between either 43 and 2000 Hz or 43 and 5000 Hz (-3 dB), and stored for offline analysis.

The electrode arrays used in this study have been described previously [12, 13]. They consisted of 61 indium tin oxide electrodes on a glass substrate, arranged in an x-scaled hexagonal lattice with 60-67 μm inter-electrode spacing. Electrodes were electroplated with platinum black [14] prior to each experiment, with resulting platinum electrode equivalent circular diameters of ∼11-19 μm. Light microscope images of electrodes were taken prior to each experiment for measurement of electrode areas.

2.2.2 Electrical stimulation

A custom 64-channel stimulation and recording system with stimulation artifact suppression [15] was used to apply the electrical stimuli and record RGC responses to visual and electrical stimuli. The electrical stimulus consisted of charge-balanced triphasic current pulses with phase durations of either 50 or 100 μs (150 or 300 μs total pulse duration). The sequence of relative current amplitudes for each phase was 2:-3:1 (anodal:cathodal:anodal). This pulse shape was chosen to minimize the electrical artifact generated by the stimulus [16], which in combination with the artifact-suppression circuitry, allowed the recording of sub-millisecond latency responses on the same electrode that was used for current injection (Fig. 2.2A). Reported pulse amplitudes correspond to the charge of the cathodal phase. All current pulses were monopolar, with a platinum wire encircling the recording chamber serving as the return electrode.

Electrical stimuli used to measure thresholds, selectivity, and response latencies consisted of pulses applied sequentially through each individual electrode of the array in a pseudorandom order at 7.5 or 15 ms intervals. The ordering of stimuli was restricted such that successive stimulation electrodes were at least 120 μm apart to reduce the likelihood of stimulating the same neuron(s) in sequential pulses. Fifty repetitions were applied to each stimulation electrode at each tested pulse amplitude, with 10% increments between successive amplitudes. Electrical stimuli used to check for long-latency responses consisted of pulses applied at 5 Hz on individual chosen electrodes, and contained either 25 or 50 repetitions at each pulse amplitude.

2.2.3 Visual stimulation

To measure visual response properties for cell type classification, a dynamic white noise stimulus was used, in which the color and intensity of each square stimulus pixel of a lattice was randomly and independently varied. This visual stimulus has been used [17] to simultaneously measure the spatiotemporal receptive field of many RGCs. The visual stimulus was optically reduced and focused onto the photoreceptor outer segments, and neutral density filters were used to maintain the stimulus at a low photopic intensity. Visual response data were collected for 30 minutes, digitized at 20 kHz and stored for offline analysis.

2.2.4 Spike sorting and cell type classification

Recorded spike waveforms were detected and clustered into groups representing the spike waveforms of distinct RGCs, as described previously [11, 18]. In the preparation presented in Fig. 2.1, a modified spike sorting algorithm was used, in which identified spike waveforms were iteratively subtracted from the recorded voltage traces as they were identified (Martin Greschner, personal communication).

Once the spikes were identified and clustered, a linear estimate of the spatiotemporal receptive field of each cell was determined by calculating the spike-triggered average (STA) visual stimulus from the white noise sequence [17]. Cells were clustered into groups corresponding to distinct cell types based on their STAs and spiking statistics, as described previously [11].

In figures, each STA is summarized by the 1.25 SD elliptical boundary of a Gaussian fit to the spatial profile of the STA. The punctate nature of the SBC STAs, due to their selective sampling of S cones, resulted in poor Gaussian fits in some cases. To represent the boundary of the RF for these cells, STAs were blurred with a Gaussian filter before fitting. The expansion of the fits caused by this filtering was corrected by scaling the resulting elliptical fits of all SBCs within the preparation by a common scale factor. The scale factor was selected to maintain the mean area of STA fits for cells with qualitatively similar fits to the original and blurred STAs.

2.2.5 Electrophysiologocial image

An *electrophysiological image* (EI) of the spiking of each cell [18, 19] was calculated in order to estimate its soma location and to facilitate the matching of electrically-elicited spikes with cells identified during visual stimulation (see Section 2.2.6). The EI of a cell consisted of the average voltage waveform generated by a spike in this cell on each electrode of the array. This electrical "footprint" of the cell typically consisted of high amplitude biphasic voltage waveforms on a cluster of 1-3 electrodes generated by the soma and dendrites, and smaller, triphasic, delayed waveforms on a series of electrodes extending away from this region, apparently reflecting action potential propagation along the axon.

2.2.6 Analysis of electrically-elicited responses

RGC responses to electrical stimulation were typically superimposed on an electrical artifact generated by the electrical stimulus, precluding the use of simple threshold-based spike-detection algorithms. Instead, spikes were identified using a combination of automated and manual voltage trace sorting. First, a custom automated algorithm grouped traces into 2 categories based on the spike template of the cell being analyzed (taken from the EI) and an initial estimate of the stimulus artifact: (1) traces that were more similar to the artifact estimate alone (failures) and (2) traces that were more similar to the sum of the artifact estimate and the spike template at one of a range of potential time offsets from the artifact (successes), based on least-squared error between the observed and expected voltage trace in each case. Because direct responses consistently occurred within 1 ms of stimulus onset (see Fig. 2.3), the potential spike range offsets were typically limited to the first 1.75 ms following stimulus onset. The group of traces categorized as failures were then used to generate an updated artifact estimate and the categorization step was repeated. This process was iterated until the categorization converged.

The results produced by the automated algorithm were visually inspected for a number of potential errors, and manual corrections were implemented as necessary. In some cases, poor initial artifact estimates prevented the algorithm from converging on the correct categorization, necessitating selection of a new initial artifact estimate. In cases in which other cells with a similar spike waveform were recorded on the chosen electrode, the automated algorithm often incorrectly classified spikes from those cells as spikes of the cell being analyzed. Comparison of the artifact-subtracted signal on neighboring electrodes with the EI waveforms of the cell being analyzed and other nearby cells typically allowed unambiguous identification of which cell generated the spike.

Some electrical stimuli elicited spikes in more than one cell. For cases in which the response curves of these cells were non-overlapping (i.e., cells with well-separated thresholds) and in which the cell being analyzed had the largest threshold, the waveforms of the cell(s) with lower thresholds were subtracted along with the artifact estimate. For cases with overlapping response curves, the traces were categorized into multiple groups: those containing only artifact, those containing spikes of each cell alone, and those containing spikes of combinations of cells. Only the traces containing a spike from the cell being analyzed were classified as successes for that cell. This was performed either by manual sorting or by running the automated algorithm using spike waveforms from all activated cells simultaneously.

In some cases, it was impossible to distinguish between traces containing and not containing a spike from the cell being analyzed. This occurred when the SNR was too low to distinguish between clusters of traces, the similarity of EIs of multiple cells precluded unambiguous determination of which spikes originated from the cell being analyzed, or when amplifier saturation masked part of the recording. Typically this only occurred when analyzing cells with very low-amplitude EI signals or at high pulse amplitudes. In these cases, response probabilities could not be determined and therefore were not used in the fitting of response curves.

To ensure that the manual correction was not influenced by the individual performing the analysis, the response curves of 10 total test cells, one "easy" cell and one "difficult" cell for each of the 5 cell types, were independently analyzed by two additional individuals. The mean percent difference in resulting threshold across the 10 response curves in comparison to the author's analysis was 0.55% and 0.65% for the two individuals, with a maximum threshold difference of 3.94% for any single response curve.

2.2.7 Latency measurements and fits

Latencies were measured as the time between stimulus pulse onset and the negative peak of the somatic spike signal. To generate post-stimulus time histograms (PSTHs), spike latencies were binned into 25 μs intervals. Only data from the two stimulus amplitudes whose response probabilities were closest to 0.5 were used (number of spikes per PSTH ranged from 26 to 72). To quantify spike latency precision, a function describing the impulse response of a cascade of low-pass filters was fit to each PSTH:

$$f(t) = \alpha \left(\frac{t - t_0}{\tau} \right)^n e^{-n\left(\frac{t-t_0}{\tau}-1\right)} \tag{2.1}$$

where n represents the number of filters, τ epresents the filter time constant, t_0 represents the filter latency and α the response amplitude. The functional form resulting from $n = 3$ provided an accurate fit to the PSTHs and was used for all cells. The values of τ, α and t_0 were constrained to be positive. The full width at half maximum was determined for each fit, and mean and standard error across all cells are reported.

2.2.8 Threshold measurement

Threshold values were extracted by fitting a cumulative Gaussian distribution to a set of response probabilities measured over a range of pulse amplitudes. The maximum likelihood curve parameters were determined using a standard nonlinear minimization algorithm (Nelder-Mead simplex direct search). Because spontaneous spikes that occurred in the first 1.5 ms following stimulus onset were not distinguished from electrically-elicited spikes, nonzero response rates often were measured for stimuli far below threshold, influencing the likelihood of the fits. To reduce the influence of spontaneous activity on the curve fits, the fit was performed iteratively, using only data from the range of pulse amplitudes that corresponded to between 0.1 and 0.9 response probability of the curve fit. In cases in which this iterative fitting failed to converge to a single range of tested pulse amplitudes, (i.e., oscillation between two or more ranges of amplitudes), the union of these ranges was used.

In some cases, response probabilities could not be determined over the entire pulse amplitude range required to capture the full response curve, either because it was not possible to distinguish between traces containing versus not containing a response for all pulse charge amplitudes (see Section 2.2.6) or because only part of the response curve fell within the tested pulse amplitude range. To limit the error induced by incomplete measurements, target cells that did not reach a response probability of at least 0.4 for at least one analyzed pulse amplitude were not included as stimulated target cells in the threshold and selectivity analyses. Note that this requirement was not imposed on non-target cells investigated in the selectivity analysis.

2.2.9 Selection of target cells and stimulation electrodes

For the analysis of activation thresholds and selectivity, an attempt was made to only target cells with somas positioned over the array. Because soma positions were not directly measured, the EI of each cell was used to estimate which of the cells detected in a given recording had somas positioned over the array. Cells that likely did not lie over the array appeared in the recording as either pure axonal signals, characterized by small triphasic voltage waveforms [18, 19], or as small signals recorded by electrodes on the edge of the array. The cell was classified as lying over the array if one of two criteria were met: the maximum somatic signal either (1) was detected on a non-edge electrode or (2) had an amplitude that was greater than 50% of the mean peak signal amplitude of all of the cells that met the first criterion within the same cell type in the same preparation. Note that non-target cells analyzed for potential activation in the selectivity analysis were not limited to cells classified as "over the array".

Many cells could be activated by more than one stimulation electrode. To address this, a search was performed for each cell to locate the stimulation electrode that resulted in the lowest local activation threshold. All reported threshold and selectivity results correspond to stimulation with this electrode. The search initially included the electrode with the highest amplitude EI signal (approximate soma location) and the 6 (or fewer for electrodes on the edge of the array) nearest-neighboring electrodes. If the lowest detectible threshold was in response to one of the neighboring electrodes, all electrodes neighboring this new "center" stimulation electrode were also investigated. When a neighboring electrode could not be analyzed through the pulse amplitude necessary to determine whether it resulted in a lower threshold than the center, all electrodes neighboring this additional electrode were also investigated for potential lower activation thresholds. This search was continued until a local minimum threshold was found. The stimulation electrodes located using this search method were typically very close to the estimated soma position or slightly displaced along the direction of the axon. In over half (62.1%) of the cases, the resulting stimulation electrode was the same as the electrode with the peak EI signal, and the mean distance between the stimulation electrode and the electrode with the peak EI signal was 28.97 μm.

While reported thresholds are based on stimulation with electrodes located as close as possible to the region of peak sensitivity of each cell, stimulation electrode position was limited to the 60 μm grid of electrodes on the electrode array. As a result, the precise region of peak sensitivity of each RGC occupied a particular uncontrolled physical location in relation to the stimulation electrode. Because of this lack of control over stimulation electrode position, and the fact that data for some stimulation electrodes could not be analyzed over the entire tested pulse amplitude range, the thresholds reported in Fig. 2.5 should be considered an upper bound on the threshold achievable using electrodes of this diameter. Therefore, no statistical summary or comparison of thresholds in different cell types was attempted; instead all measurements are reported.

2.2.10 Selectivity analysis

Stimulation selectivity was assessed rigorously in two preparations. In one preparation, complete or nearly complete mosaics of ON and OFF midget and ON and OFF parasol cells were recorded. In a second preparation, only the ON midget and ON parasol cell types contained complete mosaics, so the analysis was limited to these cell types. In both preparations, an attempt was made to selectively activate each recorded midget ganglion cell lying over the array (see Section 2.2.9). For each target midget cell, the stimulation electrode resulting in the lowest measurable threshold was first determined (see Section 2.2.9). Every other recorded midget and parasol cell was then checked for activation by this stimulation electrode over the range of pulse amplitudes required to activate the target midget cell. The range of pulse amplitudes for which analysis of all non-target cells was possible in each case is marked in grey in Fig. 2.7. For two of the target cells, this analyzable range was not large enough to contain any portion of the target cell activation range (i.e., the target cell did not reach 0.2 response probability in the fully analyzable amplitude range); these two cells were excluded from Fig. 2.7.

Response probabilities plotted in Fig. 2.6A,C,E are based on direct measurement of the fraction of trials containing a spike within 1.5 ms from stimulus onset in all cases except one: response probability of the activated ON parasol cell in Fig. 2.6E is based on the response curve fit because a direct measurement could not be made at this current amplitude. All nonzero response probabilities for cells depicted in Fig. 2.6A,C,E without corresponding response curves in Fig. 2.6B,D,F likely reflected spontaneous spiking, based on the fact that they did not exhibit the characteristic time-locking to the stimulus pulse of direct electrical activation (see Fig. 2.2, 2.3).

2.3 Results

To test the effectiveness of electrical stimulation in the major RGC types, we recorded and stimulated ganglion cells in isolated primate retina using multi-electrode arrays. First we identified the distinct cell types based on their light response properties, then we applied current pulses through the electrodes while recording the elicited activity.

2.3.1 Cell type classification

Distinct RGC types were identified based on their visual response properties and spike train temporal structure as described previously [11]. Briefly, in all recordings, most of the recorded cells were classified as belonging to one of five functionally distinct groups. The receptive fields of each group tiled the region of retina recorded (Fig. 2.1), indicating that each group corresponded to a morphologically distinct cell type. The five most commonly observed types were identified as ON and OFF midget, ON and OFF parasol, and small bistratified based on cell density and visual response properties. These cell types comprise approximately 75% of the visual signal transmitted to the brain. Occasionally, spiking amacrine cells and ganglion cells of unknown type were encountered, but these were not studied further.

2.3.2 Responses to electrical stimulation

RGCs of each of the five major types were directly activated by brief, low-amplitude current pulses delivered through individual electrodes. The responses

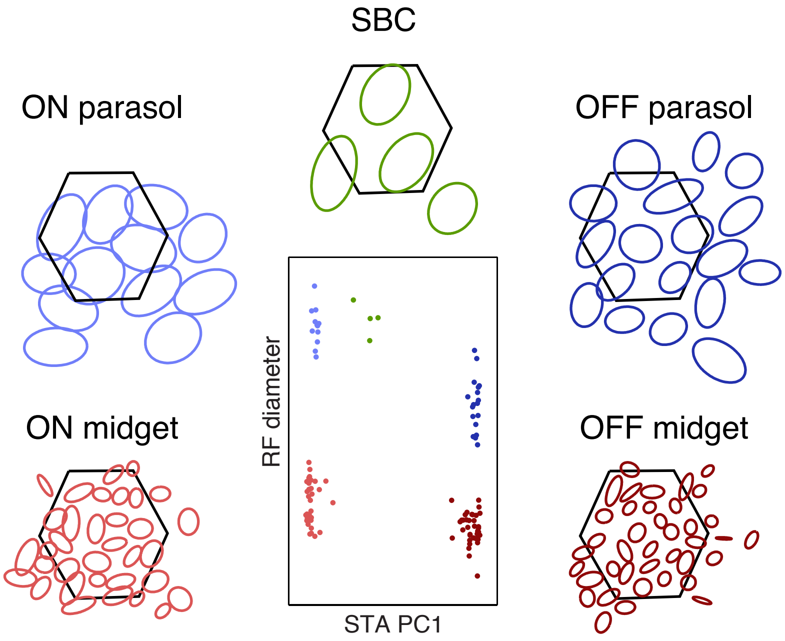

Figure 2.1: Classification of major RGC types in primate retina. Center: light response time course (STA) and receptive field (RF) size were used to cluster cells recorded in a single preparation into distinct groups. Surrounding: Receptive fields of cells within each cell type tile visual space. Ellipses depict the 1.25 SD boundaries of Gaussian fits to the spatial component of each cell's STA. For SBCs, STA blurring was performed prior to fitting to improve fit stability (see Section 2.2.4). Hexagons show position of the electrode array.

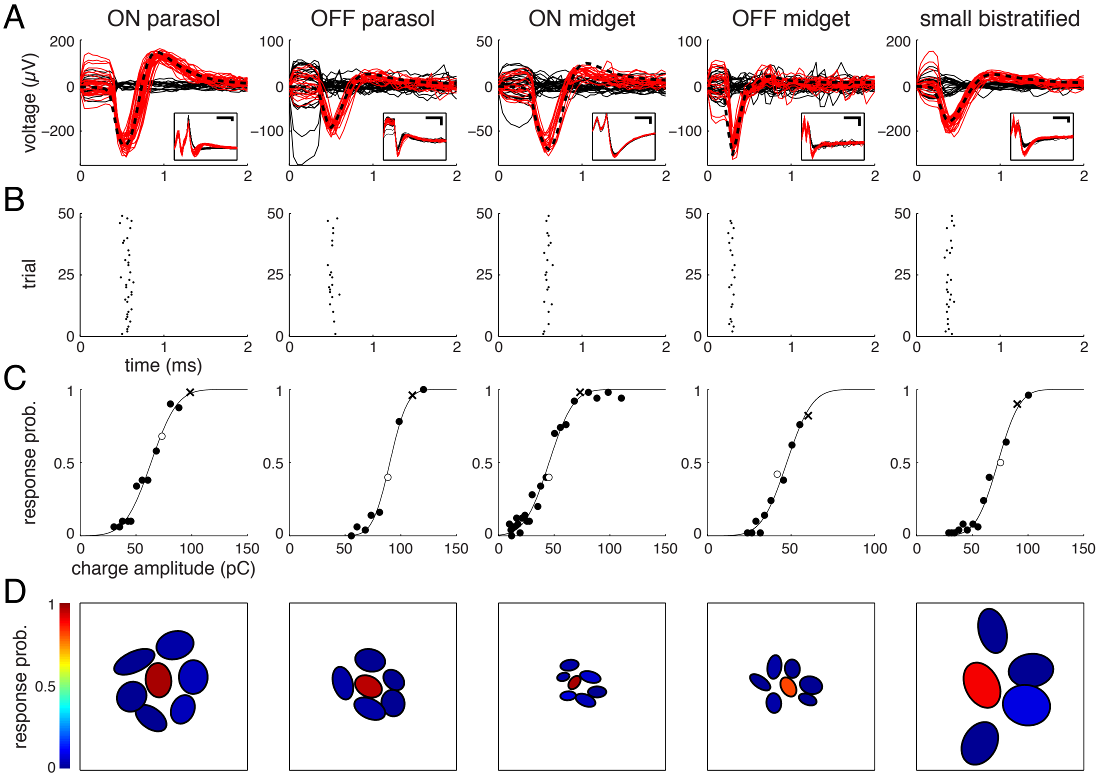

Figure 2.2: Spike detection, response timing, response curves and selectivity of one example RGC from each of the five major types. (A) Overlaid raw (inset) and artifact-subtracted voltage traces (main axes) recorded during and immediately after 50 stimulation trials, with successes (traces containing a spike) in red and failures (traces containing only stimulus artifact) in solid black. Black dashed traces show the spike template of each cell, taken from the EI (see Section 2.2.5). Voltage traces were recorded by the electrode used for stimulation in all examples except the OFF parasol, in which voltage traces were recorded by a neighboring electrode. Inset scale bars correspond to 0.5 ms and 100 μV. (B) Raster plots of responses shown in 1st row, with spike time defined as the negative peak of the spike waveform. (C) Response probabilities measured over a range of pulse amplitudes, fit by a cumulative Gaussian curve. For each cell, open circle indicates pulse charge amplitude applied in A and B, and x symbol indicates amplitude applied in D. (D) Selective activation of the example cell among neighboring cells of the same type. Each cell is represented by an elliptical fit to its receptive field, and the color of the fit indicates the fraction of trials in which the current pulse elicited a response.

elicited in one sample cell of each type are summarized in Fig. 2.2. The collection of voltage traces recorded during and immediately after 50 applications of a triphasic current pulse were typically separated into two distinct groups based on waveform (see Section 2.2.6, Fig. 2.2A). These two groups corresponded to trials in which the cell fired a spike in response to the pulse (successes), and trials in which it did not (failures). The electrical recording artifact produced by the current pulse was removed from all traces by subtracting the mean of the traces identified as failures. In each case, the resulting response waveform in each trial identified as a success closely matched the waveform of the spikes of a specific cell recorded during visual stimulation (Fig 2.2A, dashed waveforms). The artifact-reduction circuitry built into the stimulation and recording system [15] and the triphasic current pulse shape [16] reduced the artifact size significantly, avoiding amplifier saturation and revealing RGC spikes as early as 50 μs after current injection on the electrode used to apply the current pulse as well as on other electrodes.

At sufficiently high pulse amplitudes, nearly all examined cells of each type could be stimulated reliably and with high temporal precision (Fig. 2.2B, also see below). Decreases in pulse amplitude resulted in a sigmoidal decline in the fraction of trials in which the cell responded (Fig. 2.2C) as observed in previous work [5, 6, 20]. In many cases, cells could be activated with high spatial selectivity: a particular pulse amplitude reliably activated one cell without activating any of the neighboring cells of that type (Fig. 2.2D) [5]. Selectivity is treated more extensively below.

Responses to electrical stimulation always occurred within 1 ms of stimulus onset, similar to previous results for electrical stimulation of ON and OFF parasol RGCs reported in Sekirnjak et al. 2008 [5] (note the difference in spike time definition). Latencies from stimulus onset for all cells successfully activated in this study are summarized in Fig. 2.3. For each cell, the mean latency was always below 1 ms, and the typical variability in latency was very low; the mean width at half maximum value was 76±4 μs. These short and reproducible latencies were previously found to reflect direct electrical activation of RGCs rather than indirect activation via retinal interneurons, and suggest that electrical stimulation has the

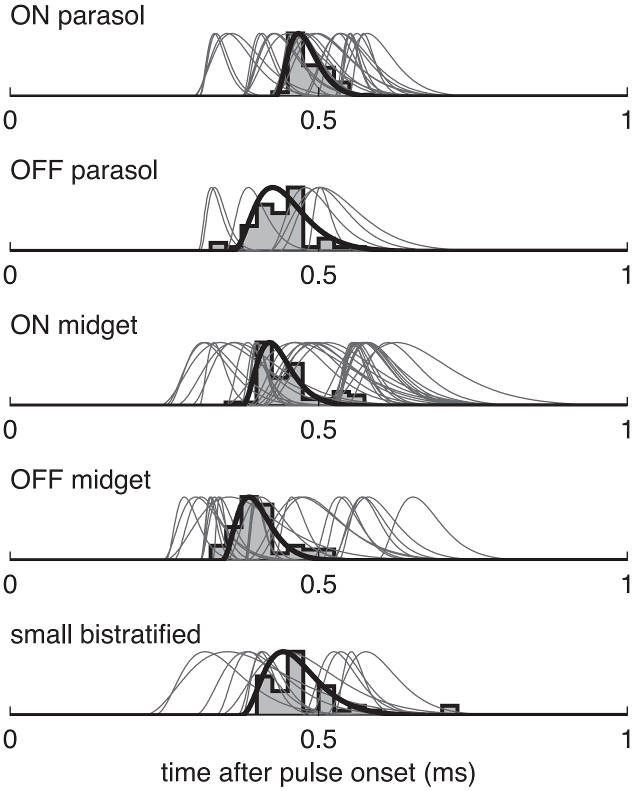

Figure 2.3: Latency and temporal precision of RGC activation. The PSTH of a representative cell from each cell type is shown with corresponding fit in black (see Section 2.2.7). Fits for all other cells are in grey. Spike times are defined by the negative peak of the spike waveform (rather than onset of spike waveform, as was used in Sekirnjak et al. 2008 [5]).

capacity to faithfully reproduce the temporal code of RGCs [13, 21] (see Section 2.4.1).

To investigate the possibility of additional indirect, longer-latency responses due to electrical activation of interneurons, RGC activity was examined over a period of 100 ms following pulse onset for three cells of each type over a range of stimulus amplitudes, including those high enough to directly activate each cell with greater than 0.99 probability. Of the fifteen cells investigated, only one showed any sign of activation at latencies >1 ms. For this cell, a small fraction (<20%) of the initial (<1 ms latency) spikes were followed by a second spike roughly 2 ms later. These second spikes were most likely a consequence of the intrinsic membrane dynamics of the cell, as has been observed previously [13], rather than indirect activation via retinal interneurons. This conclusion is based on two observations. First, these longer-latency spikes did not occur above chance in trials that did not also contain a short-latency spike, suggesting that the first spike was required to elicit the second spike. In addition, the timing of the second spike relative to the first spike closely matched a peak in the autocorrelation function of the cell obtained during responses to visual stimulation, indicating that similar spike pairs frequently occurred in the absence of electrical stimulation (data not shown).

2.3.3 Comparison of thresholds in different cell types

To determine whether different RGC types exhibit different sensitivity to electrical stimulation, the thresholds for electrical activation of cells of each type were compared in four preparations. In each preparation, a subset of the five major cell types was examined; cell types with partial mosaics of receptive fields were not analyzed to avoid potential sampling bias. Threshold was defined as the pulse charge amplitude required to elicit spikes in 50% of trials.

Initial examination of the responses of ON and OFF midget and ON and OFF parasol cells in a single retinal preparation indicates that these cell types have similar sensitivity to electrical stimulation. Responses of a representative cell of each of these types are shown in Fig. 2.4. The threshold pulse charge amplitudes of these cells all fell within a two-fold range. Comparison of thresholds within a

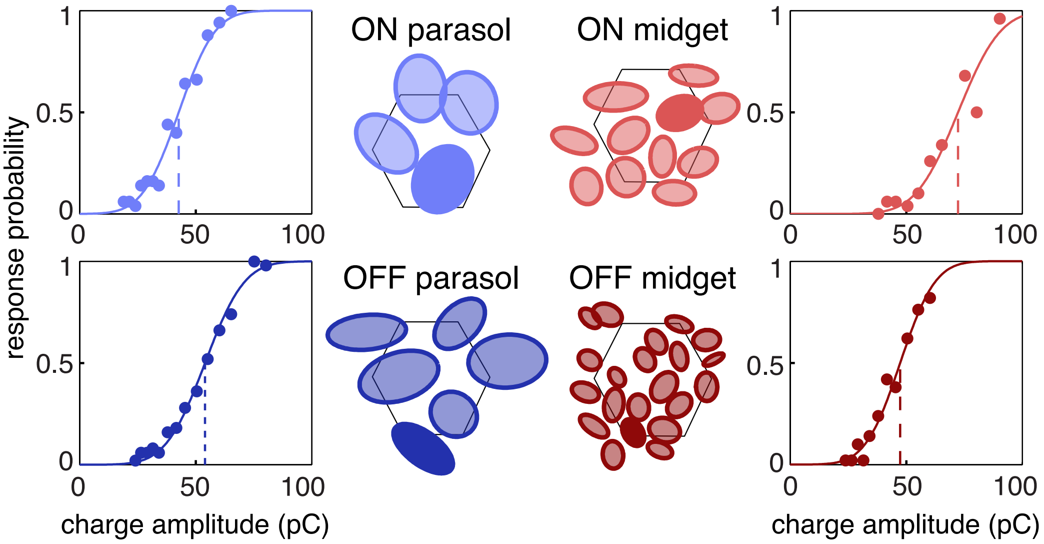

Figure 2.4: Activation thresholds of representative ON and OFF midget and ON and OFF parasol cells recorded in the same retinal preparation. Response curve of one representative cell of each type is shown. Receptive fields of cells positioned over the array are depicted as elliptical fits. Receptive fields of different cell types are plotted separately for clarity, with the array position indicated by a hexagonal outline. Receptive field corresponding to each example response curve is indicated with a solid fill.

preparation eliminated the potential influence of differences in health or physical placement of different retinal preparations.

The results of stimulation of all ON and OFF midget and ON and OFF parasol cells in this preparation are summarized in Fig. 2.5A. Nearly all of the cells (38 of 42) were successfully activated within the tested pulse amplitude range, and the range of measured activation thresholds for the different cell types was largely overlapping. The examined cells represent essentially all of the ON and OFF midget and ON and OFF parasol cells in this retinal region, as indicated by the even tiling of receptive fields of each cell type (Fig. 2.4). An attempt was made to find the electrode that resulted in the minimum threshold for each cell; however, the actual minimum achievable threshold may be slightly lower due to limitations in the precise location of stimulation electrodes relative to the region of peak sensitivity of each cell (see Section 2.2.9). ON and OFF midget ganglion cells exhibited a slightly broader distribution of thresholds than ON and OFF parasol cells.

Similar to the first preparation, the measured activation thresholds of midget and parasol cells in the second preparation overlapped significantly, with a slightly wider spread of midget thresholds than parasol thresholds (Fig. 2.5B). A smaller fraction of the ON midget ganglion cells in this preparation had measurable responses to electrical stimulation than in the first preparation. This is likely attributable to the fact that a smaller range of pulse charge amplitudes was applied in this preparation (Fig. 2.5 grey regions signify untested pulse amplitudes). This explanation is supported by the observation that the fraction of ON midget ganglion cells with thresholds falling below the maximum charge amplitude applied in the second preparation was similar in the first and second preparations (55.6% and 64.5%, respectively).

To determine whether the sensitivity of SBCs to electrical stimulation is comparable to that of other cell types, two additional preparations with nearly complete mosaics of SBCs were analyzed. In these preparations, analysis was limited to the ON parasols and the SBCs, using the ON parasol cells as a benchmark. The range of SBC thresholds was similar to the range of ON parasol thresholds in

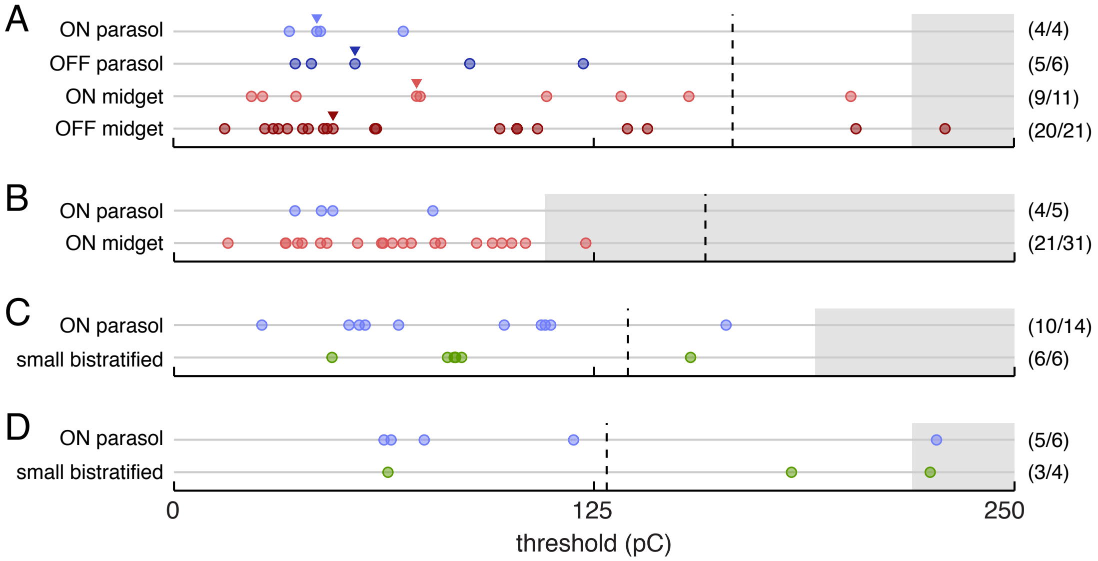

Figure 2.5: Comparison of measured activation thresholds of different cell types within four preparations. (A) Thresholds of all activated cells from the preparation represented in Fig. 2.4. Thresholds corresponding to example response curves shown in Fig. 2.4 are marked with triangles. (B,C,D) Measured thresholds for all cells from examined cell types in three additional retinal preparations. Values in parentheses indicate the fraction of cells lying over the array with measurable thresholds. Dashed vertical lines mark the conservative platinum charge density limit of 0.1 mC/cm^2 based on the mean geometric area of the electrodes used in each preparation. Grey regions indicate untested pulse charge amplitude ranges.

these preparations (Fig. 2.5C,D). The fact that the ON parasol and SBC thresholds measured in the fourth preparation were slightly higher than the thresholds in the other three preparations highlights the importance of within-preparation comparisons. The overlap between SBC and ON parasol threshold ranges within these two preparations suggests that the sensitivity of SBCs to electrical stimulation is similar to the other 4 cell types examined in this study.

A common concern regarding the use of small-diameter electrodes for electrical stimulation is the safety of the charge densities required to activate cells. In this study, all measured activation thresholds fell well within the commonly cited platinum charge density limit of 0.3-0.35 μA/cm^2 [22], and the majority of thresholds fell within the more conservative 0.1 mC/cm^2 platinum charge density limit (Fig. 2.5 dashed lines) [23]. Furthermore, these activation threshold charge densities are likely to be significantly overestimated (see Section 2.4.3).

2.3.4 Spatial selectivity

While previous work has shown that individual ON and OFF parasol cells can be selectively activated without activating neighboring parasol cells [5], it is unclear whether this level of spatial specificity is achievable when the much higher-density ON and OFF midget ganglion cells are considered simultaneously. Similarly, in the results presented in Fig. 2.2D, although it was possible to selectively activate single cells of each type without activating neighboring cells of the same type, activation of nearby cells of different types was not addressed.

As a more stringent test of spatial selectivity, every individual midget cell lying over the array in two preparations was probed to determine whether it could be activated without also activating any other cells of the same type or other types. A range of selectivity across cells was revealed by this analysis. Three example target cells illustrating this range are shown in Fig. 2.6. The first (Fig. 2.6A,B) is an example of complete selectivity. The response probabilities of the target OFF midget cell, along with all other ON and OFF midget and parasol cells recorded in this preparation, are shown for a stimulation electrode and pulse amplitude that reliably activated the target cell. While the target cell was activated in essentially

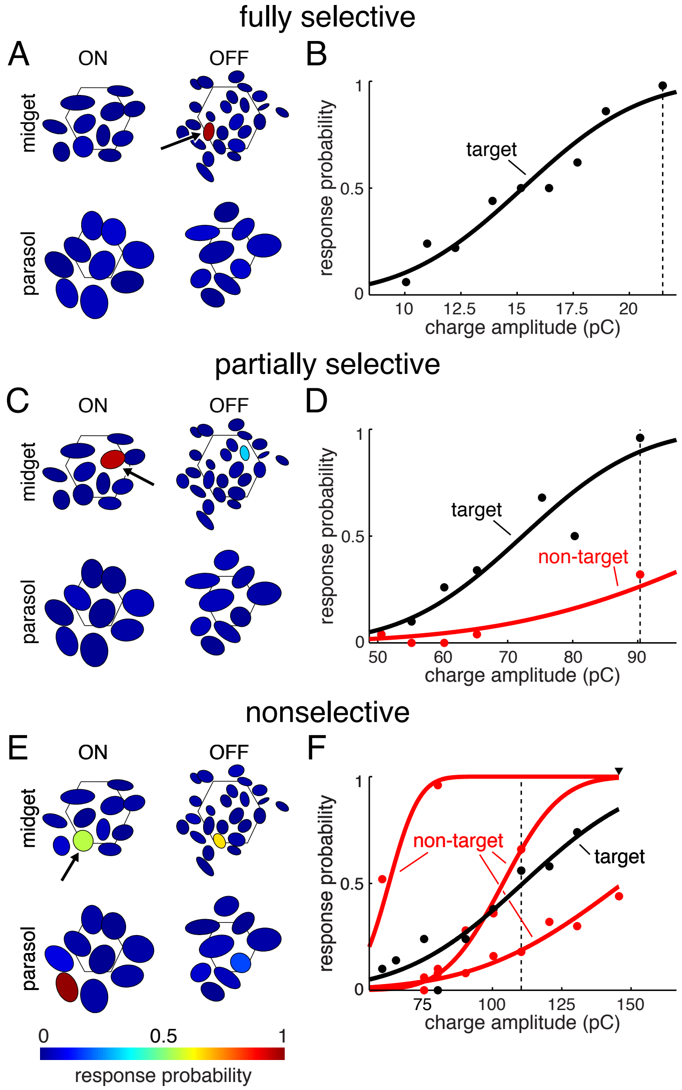

Figure 2.6: Example target cells illustrating different degrees of selectivity. (A,C,E) Response probability of each cell for a specific stimulation electrode and pulse amplitude. Cells are represented by elliptical fits to their visual receptive fields, and each target cell is marked with an arrow. Fill colors indicate response probabilities. Mosaics of receptive fields are separated and midget mosaics are enlarged 25% relative to parasol mosaics for clarity. The position of the array is shown as a hexagonal outline. (B,D,F) Response curves of activated cells. Vertical dashed lines indicate charge amplitudes plotted in A,C,E. Nonzero response probabilities in A,C,E for cells not represented in B,D,F were ≤ 0.08 and were consistent with spontaneous activity.

all of the trials, none of the other ON or OFF midget or ON or OFF parasol cells in the region responded to the current pulse.

The second example (Fig. 2.6C,D) illustrates a case of partial selectivity. In this example, the target ON midget cell was activated at lower pulse amplitudes than any other midget or parasol cell. However, one non-target cell (OFF midget) was activated by this stimulation electrode, although its response curve overlapped only slightly with that of the target cell (Fig 2.6D). At a pulse amplitude sufficient to reliably activate the target cell, the non-target cell responded in only a small fraction of the trials (Fig. 2.6C).

The final example target cell could not be selectively activated (Fig. 2.6E,F). In this case, two non-target cells (ON parasol, OFF midget) were activated at lower pulse amplitudes than the target cell, and a third non-target cell (OFF parasol), was activated at slightly higher but still largely overlapping pulse amplitudes (Fig. 2.6F). The response probability for each of these cells, along with all other ON and OFF midget and parasol cells recorded in this preparation, are shown for a stimulus amplitude near the threshold of the target cell (Fig. 2.6E). The non-target ON parasol and OFF midget cell were more strongly activated than the target ON midget cell at this amplitude, and the non-target OFF parasol was weakly activated.

The fact that the activated non-target cells in these examples had receptive fields positioned close to the target cell receptive field suggests that the somas of the non-target cells were located near the stimulation electrode. This was verified by examining the putative soma location of each activated non-target cell, based on the location of peak voltage deflection of the electrophysiological image of the cell (data not shown), a proxy for soma location. However, in some examples of poor selectivity, one or more of the activated non-target cell(s) were distant from the target cell. All cases of distant cell activation appeared to be due to axon stimulation, a conclusion based on proximity of the stimulation electrode to the axon of the activated non-target cell inferred from the electrophysiological image (data not shown). In total, axonal stimulation, classified as activation in which the stimulation electrode was >150 μm from the peak somatic signal of the non-target cell, accounted for roughly half of the total number of cases of non-target activation in this study. It is expected that many additional axons, originating from distant RGCs not recorded in these preparations, were present and potentially activated (see Section 2.4.4).

The selectivity results for all of the ON and OFF midget cells in this preparation are summarized in Fig. 2.7A. Data from each cell are summarized by the cell's activation range: the range of pulse amplitudes corresponding to 0.2-0.8 response probability for that cell and stimulation electrode. Half (16) of the total number of midget ganglion cells positioned over the array in this preparation could be activated with high selectivity: specifically, high target cell activation probability (>0.8) without significant activation probability (<0.2) of any non-target cells. The overall selectivity achievable when targeting ON midget cells was qualitatively similar to the selectivity achievable for OFF midget target cells.

In the second preparation, a smaller proportion of the midget cells positioned over the array could be verifiably activated with high selectivity (11 of 31). This is most likely due to the fact that the maximum charge amplitude applied in this preparation was only about half of the maximum charge amplitude applied in the first preparation. As a result, roughly one third of the midget cells were not activated above threshold (see Section 2.3.3). In addition, four cells with measurable thresholds could potentially have been activated with full selectivity at higher charge amplitudes but could not be investigated through their entire activation range (Fig. 2.7B, bottom 4 target cells). When considering only the target cells that could be analyzed through their entire activation range, the proportion of selectively activated cells in the first and second preparations was similar (16 of 26 and 11 of 17 respectively).

2.4 Discussion

The five highest-density primate RGC types were activated by brief epiretinal current pulses applied with a high-density multielectrode array. All stimulated cells exhibited precisely timed spiking responses characteristic of direct RGC

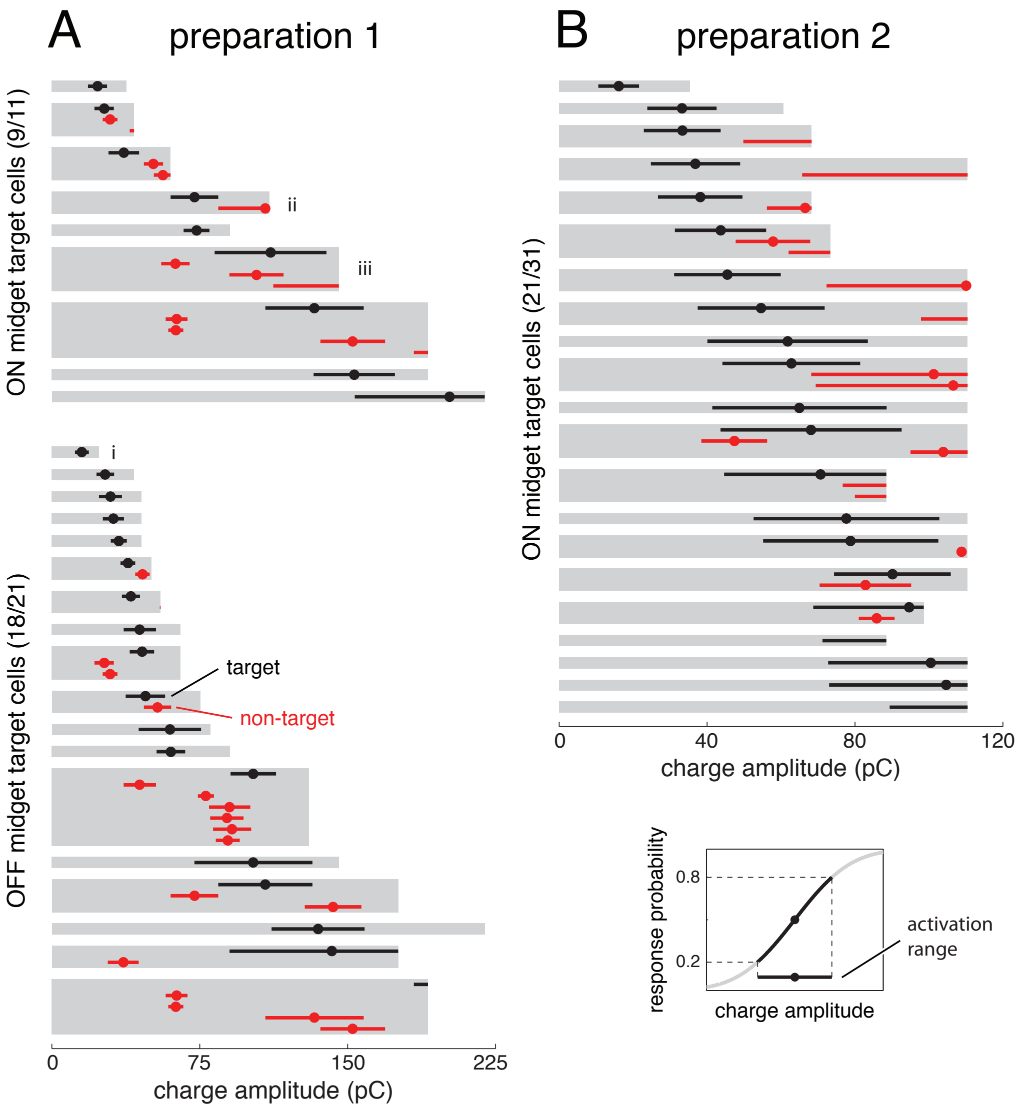

Figure 2.7: Summary of selectivity achievable for all ON and OFF midget ganglion cells recorded in two preparations. Each grey region indicates the analyzed range of charge amplitudes for the stimulation electrode associated with a particular target cell. Circles and horizontal bars show the threshold and activation range, defined as the range of charge amplitudes that resulted in response probabilities between 0.2 and 0.8 (see lower right inset), of each activated cell, with target cells in black and non-target cells in red. Selectivity attempts marked with i, ii and iii correspond to examples in Fig. 2.6 A/B, C/D and E/F respectively.

activation. In general, the activation thresholds fell within conservative charge density limits for platinum electrodes. Within-preparation comparisons of thresholds revealed similar sensitivity to electrical stimulation in the different cell types. Selective activation of a single RGC without activation of its neighbors was possible in some cases, while in other cases neighboring somas and/or axons were also activated.

2.4.1 Direct RGC activation

The precisely timed, sub-millisecond latency single spike responses observed in this study are characteristic of direct RGC activation by the electrical stimulus rather than indirect activation mediated by presynaptic retinal cells [13, 20, 21]. In some stimulation paradigms, epiretinal stimulation can elicit RGC activity via activation of presynaptic cells. Such activity is typically characterized by one or more bursts of activity at latencies $\geq$3 ms [24, 25]. There was no evidence for indirect excitation of RGCs in the 15 cells examined for responses over a 100 ms period following the stimulus. One cell responded to electrical stimulation with a pair of spikes in a fraction of the trials; this was likely a result of intrinsic membrane dynamics (see Section 2.3.2).

The absence of indirect responses is not surprising, given the short pulse widths (50 or 100 μs/phase) and small electrodes ($\sim$15 μm diameter) used in this study. It has been well established that shorter current pulses preferentially elicit direct RGC responses in comparison to longer pulse widths [21, 25–27]. In addition, the small electrodes used in this study are expected to generate relatively focal electrical fields, whereas the electric field generated by a larger diameter planar electrode at the same voltage is expected to extend deeper into the retinal tissue [28], more effectively activating interneurons in addition to RGCs.

2.4.2 Activation thresholds

Because different RGC types convey distinct visual information to different regions of the brain [4, 29], an understanding of how each specific cell type responds to electrical stimulation is crucial to the development of effective retinal prostheses. In addition, it may be possible to exploit particular differences in response properties, if they exist, in order to preferentially activate certain cell types. A number of cell type-specific characteristics could potentially influence sensitivity to electrical stimulation. Different RGC types have been shown to have distinct intrinsic membrane properties [7, 8] which are likely mediated in part by differential expression of ion channels [30, 31]. Cell-type specific differences in the length of the high sodium channel density region of initial segments, the region thought to be most sensitive to electrical stimulation, have been observed in rabbit [6]. Because most of these cell type specific characteristics have not been measured directly in primates, it is difficult to know what effect they might have on the response properties of the RGC types examined here.

Previous data on direct activation thresholds of different RGC types have been inconsistent. A recent study reporting the thresholds of three rabbit RGC types [6] showed significant differences in threshold between types. Another study found an inverse correlation between soma size and stimulation threshold in mouse [32], suggesting a possible correlation between RGC type and stimulation threshold in this species. In contrast, other studies report no significant differences in direct stimulation threshold between putative cell types in rabbit [20] or mouse [33], although the reported groupings (ON, OFF, ON-OFF) probably represent groups of cell types, potentially masking sensitivity differences between the true individual cell types. Finally, a study comparing ON and OFF parasol RGCs in primate found no significant difference in direct activation threshold [5].

In the current study, no clear differences in direct activation thresholds between cell types were observed. There are at least two possible explanations for the difference between the current results and those reported in Fried et al. 2009 [6]. First, at least two of the three cell types examined in the Fried study (ON-OFF direction selective, local edge detector) are, based on their light response properties, unlikely to be homologous to the primate cell types examined in this study. Therefore, the different result may simply reflect the fact that certain RGC types have distinct thresholds while others have similar thresholds. Second, the distance between the stimulation electrode and the region of highest sensitivity of each RGC was less controllable in this study; the potential stimulation electrode positions were constrained to a fixed grid with 60 μm spacing, whereas the Fried et al. 2009 study searched for the lowest threshold using 10μm steps. This experimental difference probably underlies the greater range of thresholds measured within individual cell types in this study. Still, any differences in sensitivity to electrical stimulation of these five cell types would have to be small to be masked by this variability. Furthermore, it is unclear whether future clinical prostheses will have the spatial resolution required to exploit such subtle differences in stimulation thresholds.

Midget ganglion cells exhibited a greater range of measured thresholds than parasol ganglion cells. There are a couple of potential explanations for this observation. First, because the precise location of the stimulation electrode relative to each RGC could not be controlled, the measured thresholds correspond to a range of distances between stimulation electrode and location of maximum sensitivity. A recent study found the size of the region of high sensitivity to be cell-type dependent [6]. Thus, greater threshold variability in midget ganglion cells may reflect a more localized region of high sensitivity. Alternatively, some aspects of midget ganglion cell morphology or membrane properties may simply be more variable than parasol ganglion cells, resulting in a larger variability in sensitivity to extracellular stimulation. Future studies examining the spatial spread of parasol and midget ganglion cell sensitivity, similar to those performed previously for non-primate RGCs [6, 34], must be performed in order to determine the underlying cause of these differences.

2.4.3 Stimulation safety

The use of small electrodes in neural prosthetics can be damaging to both electrodes and neural tissue if the charge densities required to activate cells are high enough to generate irreversible electrochemical reactions at the electrode surface [35]. In this study, the majority of cells examined had activation thresholds that fell within the conservative platinum charge density limit of 0.1 mC/cm^2 determined by Rose and Robblee [23], based on geometric electrode area. However, the electrodes used in the Rose and Robblee study had much lower roughness factors (ratio of actual area to geometric area) (1-5x) than the estimated roughness factor (100x) of the fractal-like platinum electrode surfaces generated by the electroplating process used in this study [36]. As a result, the actual charge densities at the activation thresholds measured in the this study likely fell well below the actual charge densities near the safety limits determined by Rose and Robblee. In addition, the 0.1 mC/cm^2 charge density limit is relatively conservative; other studies examining the charge density necessary to generate significant adverse electrochemical reactions at the surface of platinum electrodes have suggested that densities of up to 0.30-0.35 mC/cm^2 are safe [22], and a recent study of high-frequency stimulation in rat retina with platinum electrodes found no significant histological changes to the retina at all tested charge densities, up to 0.68 mC/cm^2, [37]. Finally, other electrode materials such as iridium oxide may be used in place of platinum to extend the range of charge densities that can be injected without inducing unwanted electrochemical reactions at the electrode surface [38, 39].

In addition to adverse electrochemical reactions occurring at the electrode surface, stimulation-induced tissue damage may occur as a result of excessive neural activation [35]. This “mass action theory” mechanism of tissue damage is highly unlikely when using electrodes and pulse charge amplitudes on the scale of those used in this study, due to the highly focal nature of the excitation. This assertion is supported by findings that much higher charge densities can be applied with smaller electrodes before observable neural damage occurs [40].

2.4.4 Spatial selectivity

An ideal retinal prosthesis would be able to veridically recreate the natural spatiotemporal RGC activity patterns generated in a healthy retina in response to a visual scene. This would require precise control over the timing of spikes in individual RGCs. Highly precise temporal control over the spike timing has been demonstrated in this study and in previous studies [5, 21], but it is less clear whether single-cell spatial resolution is possible, even with much higher density electrode arrays than those used in current clinical prostheses. Studies examining the relationship between stimulation electrode position and direct RGC activation using electrodes similar in size to those used in this study have shown that the area of highest sensitivity of direct RGC activation is a localized region near the axon initial segment [6], with cathodal stimulation thresholds increasing as a power-law function of lateral distance with exponents of ∼2.5-3.2 for distances >50 μm [34]. Sekirnjak et al. [13] noted that thresholds increased by an average of ∼300% when stimulating with an electrode 60 μm from the electrode yielding the lowest threshold. However, single-cell activation may still be difficult due to the large cell-to-cell variability in direct stimulation threshold and the high density of RGCs in the primate retina.

Few attempts have been made to directly record the RGCs that are activated by focal epiretinal stimulation. A recent study in salamander found that even small stimulation electrodes (10 μm) simultaneously activated many RGCs over a relatively large retinal region. However, the pulse widths used for these measurements ($\geq$ 400 μs) were shown to activate RGCs through a combination of direct and indirect stimulation [41]. A study in rat [13] found no direct activation of cells further than 60 μm from the stimulation electrode when using stimuli with amplitudes slightly above the mean threshold (∼0.1 mC/cm^2). However, no attempt was made to measure the proportion of total RGCs that were recorded, and unrecorded cells may have been activated. A more recent study [5] found that ON and OFF parasol cells could be individually activated. In this study, the presence of clear mosaics of receptive fields within each cell type was used to confirm that all parasol cells in the region were successfully recorded. However, the parasol cells only make up a fraction (∼16%) [4] of the total number of primate retinal ganglion cells, so it is possible that RGCs of other cell types that were not examined were activated.

The ON and OFF midget ganglion cells, which are the two most numerous cell types in the primate retina and are thought to mediate high-acuity vision, provide a more stringent test of single-cell selectivity. Together with the ON and OFF parasol cells, these cell types constitute nearly 70% of the total number of retinal ganglion cells [4]. The successful recording of complete or nearly complete populations of the examined cell types was confirmed in the current study based on receptive field tiling. In the two preparations examined in this study, selective activation was achievable in roughly half of midget cells with detectible thresholds.

Putative axon stimulation accounted for roughly half of the cells that were inadvertently activated when targeting a particular RGC. If axonal activation thresholds are relatively constant along their length as they course towards the optic nerve, it is likely that many additional axons, originating from distant RGCs not recorded in these preparations, were activated in at least a portion of the selective activation attempts. As a result, the proportion of cells that can be truly selectively activated in a full retina would probably be lower than these measurements suggest. In addition, these experiments were performed on peripheral retina (9-9.5 mm), where RGC density is relatively low. Selective activation would be more difficult to achieve in the central retina, where retinal prostheses are typically located, and where RGC density is significantly higher.

The difficulty in selectively activating some of the individual RGCs under these conditions suggests that simple single-electrode stimulation with an electrode array of 60 μm or larger spacing will not be sufficient to veridically recreate natural RGC activity patterns on a cell-by-cell basis. Single-cell selectivity of all RGCs will require either higher density electrode arrays, novel electrode geometries or more sophisticated stimulation patterns [42, 43] (see Chapter 3).

2.4.5 Retinal degeneration

Due to the lack of primate models of outer retinal degeneration, only healthy retinal tissue was used in this study. Outer retinal degeneration results in extensive remodeling of the retinal circuitry [44]. However, RGC morphology and intrinsic membrane dynamics appear to be largely preserved [45, 46], suggesting that thresholds and kinetics of direct RGC activation may be relatively stable during degeneration. On the other hand, physiological recordings in animal models of retinal degeneration have uncovered aberrant synaptic inputs to RGCs which have been shown to underly rhythmic firing and contribute to elevated spontaneous firing rates [47–50]. The resulting changes in RGC resting membrane state, along with intrinsic elevation of hyperactivity observed in a subset of RGCs [49, 50], may alter their sensitivity to electrical stimuli.

Several studies have found that outer retinal degeneration can increase RGC activation thresholds to electrical stimulation; however, the majority of these studies examined indirect activation [51–57], or activation that couldn't be definitively classified as direct or indirect [58–61]. The studies examining direct RGC response thresholds have had inconsistent results. One study of epiretinal stimulation in a mouse model of rapid degeneration found significantly elevated thresholds, although this elevation appeared to be at least partially due to complications with the dissection of the fragile degenerate retinas [33]. Studies investigating rat models of retinal degeneration found similar direct activation thresholds at moderate [53] and advanced [62] stages of degeneration, in comparison to healthy retinas. Measurements of activity in the superior colliculus [63] and visual cortex [64] that likely reflected direct RGC activation found significantly elevated thresholds, although activity in these central structures may have required simultaneous activation of multiple RGCs, so increased thresholds may have been a reflection of decreased RGC density [63] rather than decreased sensitivity of individual RGCs. It remains to be determined whether the response properties of primate RGCs to direct electrical activation will be altered in the course of outer retinal degeneration.

Acknowledgements

This work would not have been possible without the invaluable contributions of my coauthors, including many associated with the Santa Cruz Institute for Particle Physics at the University of California, Santa Cruz. Of special note, Pawel Hottowy designed and tested the electrical stimulation system that was crucial for all of the data presented in this thesis, as well as the Labview software required to run the stimulation and recording system and the core Matlab software to read and sort the electrical stimulation data. In addition, Pawel helped to run several of the early experiments using the system, and has provided valuable

input on experiment planning and analysis. Keith Mathieson and Debbie Gunning fabricated the electrode arrays used in all of the electrical stimulation experiments, helped to train me in the use of the stimulation system, helped to install and debug the stimulation system at the Salk Institute, and provided assistance in several experiments.

I would like to acknowledge Martin Greschner for data analysis; Matthew Grivich for software development; Clare Hulse for technical assistance; Tomasz Fiutowski, Sergei Kachiguine, Andrzej Skoczen and Alexander Sher for technical development; Steve Barry for machining; and Howard Fox, Mike Taffe, Ed Callaway, John Reynolds, and Rich Krauzlis for access to primate retinas.

This work was supported by NEI Grant R01EY021271 (EJC, LHJ), a Sanofi-aventis Discovery Grant (EJC, LHJ), the Salk Institute for Biological Studies (EJC, LHJ), the Joseph Alexander Foundation (EJC, LHJ), the Charles Lee Powell Foundation (LHJ), NIH Grant R21-EB004410 (AL), NSF Grant PHY-0750525 (AL), the McKnight Foundation (EJC, AL), EPSRC Grant EP/E039731/1 (DEG), a Royal Society of Edinburgh fellowship (KM), a RCUK funded SU2P fellowship (KM), EPSRC Grant GR/R89189/01 (KM), and the Polish Ministry of Science and Higher Education (WD).

EJ Chichilnisky is on the scientific advisory boards of Pixium and Nanovision.

Chapter 2, in full, is currently being prepared for submission for publication of the material. Jepson L.H., Hottowy P., Mathieson K., Gunning D.E., Dabrowski W., Litke A., Chichilnisky, E.J. The dissertation author was the primary investigator and author of this material.

2.5 References

[1] Santos, A., Humayun, M.S., de Juan, E., J., Greenburg, R.J., Marsh, M.J., Klock, I.B., and Milam, A.H., 1997. Preservation of the inner retina in retinitis pigmentosa. A morphometric analysis. *Arch Ophthalmol*, 115:511–515.

[2] Medeiros, N. and Curcio, C., 2001. Preservation of ganglion cell layer neurons in age-related macular degeneration. *Investigative ophthalmology & visual science*, 42:795–803.

[3] Weiland, J., Cho, A., and Humayun, M., 2011. Retinal Prostheses: Current Clinical Results and Future Needs. *Ophthalmology*, 118:2227–2237.

[4] Dacey, D., 2004. Origins of perception: retinal ganglion cell diversity and the creation of parallel visual pathways. In M.S. Gazzaniga, editor, The Cognitive Neurosciences, pages 281–301. MIT Press, Cambridge, MA.

[5] Sekirnjak, C., Hottowy, P., Sher, A., Dabrowski, W., Litke, A., and Chichilnisky, E., 2008. High-resolution electrical stimulation of primate retina for epiretinal implant design. *J Neurosci*, 28:4446–4456.

[6] Fried, S., Lasker, A., Desai, N., Eddington, D., and Rizzo, J.r., 2009. Axonal sodium-channel bands shape the response to electric stimulation in retinal ganglion cells. *J Neurophysiol*, 101:1972–1987.

[7] Margolis, D. and Detwiler, P., 2007. Different mechanisms generate maintained activity in ON and OFF retinal ganglion cells. *J Neurosci*, 27:5994–6005.

[8] A, I., 2003. Retinal Ganglion Cell Excitability. In C.L. JS and Verner, editors, Visual Neurosciences, pages 422–450. MIT Press.

[9] Dacey, D. and Petersen, M., 1992. Dendritic field size and morphology of midget and parasol ganglion cells of the human retina. *Proc Natl Acad Sci U S A*, 89:9666–9670.

[10] Dacey, D., 1993. Morphology of a small-field bistratified ganglion cell type in the macaque and human retina. *Vis Neurosci*, 10:1081–1098.

[11] Field, G., Sher, A., Gauthier, J., Greschner, M., Shlens, J., Litke, A., and Chichilnisky, E., 2007. Spatial properties and functional organization of small bistratified ganglion cells in primate retina. *J Neurosci*, 27:13261–13272.

[12] Litke, A., 1998. The retinal readout system: an application of microstrip detector technology to neurobiology. *Nucl Instrum Methods Phys Res A*, 418:203–209.

[13] Sekirnjak, C., Hottowy, P., Sher, A., Dabrowski, W., Litke, A., and Chichilnisky, E., 2006. Electrical stimulation of mammalian retinal ganglion cells with multielectrode arrays. *J Neurophysiol*, 95:3311–3327.

[14] Cunningham, W., Mathieson, K., McEwan, F., Blue, A., McGeachy, R., McLeod, J., Morris-Ellis, C., O'shea, V., Smith, K., and Litke, A., 2001. Fabrication of microelectrode arrays for neural measurements from retinal tissue. *Journal of Physics D: Applied Physics*, 34:2804.

[15] Hottowy, P., Dabrowski, W., Skoczen, A., and Wiacek, P., 2008. An integrated multichannel waveform generator for large-scale spatio-temporal stimulation of neural tissue. *Analog Integrated Circuits and Signal Processing*, 55:239–248.

[16] Hottowy, P., Beggs, J., Chichilnisky, E., Dabrowski, W., Fiutowski, T., Gunning, D., Hobbs, J., Jepson, L., Kachiguine, S., Mathieson, K., Rydygier, P., Sher, A., Skoczen, A., and Litke, A., 2010. 512-electrode MEA System For Spatio-Temporal Distributed Stimulation and Recording of Neural Activity. *7th Int Meeting on Substrate-Integrated Microelectrode Arrays*, pages 327–330.

[17] Chichilnisky, E., 2001. A simple white noise analysis of neuronal light responses. *Network: Computation in Neural Systems*, 12:199–213.

[18] Litke, A., Bezayiff, N., Chichilnisky, E., Cunningham, W., Dabrowski, W., Grillo, A., Grivich, M., Grybos, P., Hottowy, P., Kachiguine, S., Kalmar, R., Mathieson, K., Petrusca, D., Rahman, M., and Sher, A., 2004. What does the eye tell the brain? Development of a system for the large scale recording of retinal output activity. *IEEE Trans Nucl Sci*, 51:1434–1440.

[19] Petrusca, D., Grivich, M., Sher, A., Field, G., Gauthier, J., Greschner, M., Shlens, J., Chichilnisky, E., and Litke, A., 2007. Identification and characterization of a Y-like primate retinal ganglion cell type. *J Neurosci*, 27:11019–11027.

[20] Tsai, D., Morley, J., Suaning, G., and Lovell, N., 2009. Direct activation and temporal response properties of rabbit retinal ganglion cells following subretinal stimulation. *J Neurophysiol*, 102:2982–2993.

[21] Fried, S., Hsueh, H., and Werblin, F., 2006. A method for generating precise temporal patterns of retinal spiking using prosthetic stimulation. *J Neurophysiol*, 95:970–978.

[22] Brummer, S.B. and Turner, M.J., 1977. Electrical stimulation with Pt electrodes: II-estimation of maximum surface redox (theoretical non-gassing) limits. *IEEE Trans Biomed Eng*, 24:440–443.

[23] Rose, T.L. and Robblee, L.S., 1990. Electrical stimulation with Pt electrodes. VIII. Electrochemically safe charge injection limits with 0.2 ms pulses. *IEEE Trans Biomed Eng*, 37:1118–1120.

[24] Jensen, R.J., Ziv, O.R., and Rizzo, J.F., 2005. Thresholds for activation of rabbit retinal ganglion cells with relatively large, extracellular microelectrodes. *Invest Ophthalmol Vis Sci*, 46:1486–1496.

[25] Ahuja, A., Behrend, M., Kuroda, M., Humayun, M., and Weiland, J., 2008. An in vitro model of a retinal prosthesis. *IEEE Trans Biomed Eng*, 55:1744–1753.

[26] Greenberg, R., 1998. Analysis of electrical stimulation of the vertebrate retina - work towards a retinal prosthesis [dissertation]. Ph.D. thesis, John Hopkins University, Baltimore, MD.

[27] Margalit, E. and Thoreson, W., 2006. Inner retinal mechanisms engaged by retinal electrical stimulation. *Invest Ophthalmol Vis Sci*, 47:2606–2612.

[28] Wiley, J. and Webster, J., 1982. Analysis and control of the current distribution under circular dispersive electrodes. *IEEE Trans Biomed Eng*, 29:381–385.

[29] Field, G. and Chichilnisky, E., 2007. Information processing in the primate retina: circuitry and coding. *Annu Rev Neurosci*, 30:1–30.

[30] Kaneda, M. and Kaneko, A., 1991. Voltage-gated sodium currents in isolated retinal ganglion cells of the cat: relation between the inactivation kinetics and the cell type. *Neurosci Res*, 11:261–275.

[31] AV, G., DA, V.d.L., LM, C., and WM, U., 2009. Kv1.2 and HCN1 potassium channels are selectively expressed in a subset of large retinal ganglion cells in the macaque monkey. *Society for Neuroscience Annual Meeting Abstracts*, 848.25.

[32] Cho, A., Sampath, A., and Weiland, J., 2011. Physiological response of mouse retinal ganglion cells to electrical stimulation: effect of soma size. *Conf Proc IEEE Eng Med Biol Soc*, 2011:1081–1084.

[33] Margalit, E., Babai, N., Luo, J., and Thoreson, W., 2011. Inner and outer retinal mechanisms engaged by epiretinal stimulation in normal and rd mice. *Vis Neurosci*, 28:145–154.

[34] Jensen, R.J., Rizzo, J.F., Ziv, O.R., Grumet, A., and Wyatt, J., 2003. Thresholds for activation of rabbit retinal ganglion cells with an ultrafine, extracellular microelectrode. *Invest Ophthalmol Vis Sci*, 44:3533–3543.

[35] Merrill, D., Bikson, M., and Jefferys, J., 2005. Electrical stimulation of excitable tissue: design of efficacious and safe protocols. *J Neurosci Methods*, 141:171–198.

[36] Mathieson, K., Kachiguine, S., Adams, C., Cunningham, W., Gunning, D., OShea, V., Smith, K.M., Chichilnisky, E.J., Litke, A.M., Sher, A., and Rahman, M., 2004. Large-Area Microelectrode Arrays for Recording of Neural Signals. *IEEE Trans Nuc Sci*, 51:2027–2031.

[37] Ray, A., Lee, E., Humayun, M., and Weiland, J., 2011. Continuous electrical stimulation decreases retinal excitability but does not alter retinal morphology. *J Neural Eng*, 8:045003.

[38] Beebe, X. and Rose, T., 1988. Charge injection limits of activated iridium oxide electrodes with 0.2 ms pulses in bicarbonate buffered saline. *IEEE Trans Biomed Eng*, 35:494–495.

[39] Weiland, J., Anderson, D., and Humayun, M., 2002. In vitro electrical properties for iridium oxide versus titanium nitride stimulating electrodes. *IEEE Trans Biomed Eng*, 49:1574–1579.

[40] McCreery, D.B., Agnew, W.F., Yuen, T.G., and Bullara, L., 1990. Charge density and charge per phase as cofactors in neural injury induced by electrical stimulation. *IEEE Trans Biomed Eng*, 37:996–1001.

[41] Behrend, M., Ahuja, A., Humayun, M., Chow, R., and Weiland, J., 2011. Resolution of the epiretinal prosthesis is not limited by electrode size. *IEEE Trans Neural Syst Rehabil Eng*, 19:436–442.

[42] Rattay, F. and Resatz, S., 2004. Effective electrode configuration for selective stimulation with inner eye prostheses. *IEEE Trans Biomed Eng*, 51:1659–1664.

[43] Grumet, A.E., 1999. Electric stimulation parameters for an epi-retinal prosthesis. Ph.D. thesis, Massachusetts Institute Of Technology, Cambridge, MA.

[44] Jones, B., Watt, C., Frederick, J., Baehr, W., Chen, C., Levine, E., Milam, A., Lavail, M., and Marc, R., 2003. Retinal remodeling triggered by photoreceptor degenerations. *J Comp Neurol*, 464:1–16.

[45] Mazzoni, F., Novelli, E., and Strettoi, E., 2008. Retinal ganglion cells survive and maintain normal dendritic morphology in a mouse model of inherited photoreceptor degeneration. *J Neurosci*, 28:14282–14292.

[46] Margolis, D., Newkirk, G., Euler, T., and Detwiler, P., 2008. Functional stability of retinal ganglion cells after degeneration-induced changes in synaptic input. *J Neurosci*, 28:6526–6536.

[47] Margolis, D. and Detwiler, P., 2011. Cellular origin of spontaneous ganglion cell spike activity in animal models of retinitis pigmentosa. *J Ophthalmol*, 2011.

[48] Borowska, J., Trenholm, S., and Awatramani, G., 2011. An intrinsic neural oscillator in the degenerating mouse retina. *J Neurosci*, 31:5000–5012.

[49] Stasheff, S.F. and Andrews, M.P., 2010. A Subpopulation of Retinal Ganglion Cells Sustains Spontaneous Hyperactivity Through Non-Synaptic Mechanisms in Mice With Retinal Degeneration. *ARVO Meeting Abstracts*, 51:5798.

[50] Sekirnjak, C., Jepson, L., Hottowy, P., Sher, A., Dabrowski, W., Litke, A., and Chichilnisky, E., 2011. Changes in physiological properties of rat ganglion cells during retinal degeneration. *J Neurophysiol*, 105:2560–2571.

[51] Ye, J., Ryu, S., Kim, K., and Goo, Y., 2010. Retinal ganglion cell (RGC) responses to different voltage stimulation parameters in rd1 mouse retina. *Conf Proc IEEE Eng Med Biol Soc*, 2010:6761–6764.

[52] Goo, Y., Ye, J., Lee, S., Nam, Y., Ryu, S., and Kim, K., 2011. Retinal ganglion cell responses to voltage and current stimulation in wild-type and rd1 mouse retinas. *J Neural Eng*, 8:035003.

[53] Pangratz-Fuehrer, S., Naik, N., and Palanker, D., 2011. Selectivity of epiretinal stimulation of retinal ganglion cells can be controlled by pulse width. *Society for Neuroscience Abstracts*, 482.08.

[54] Jensen, R. and Rizzo, J., 2008. Activation of retinal ganglion cells in wild-type and rd1 mice through electrical stimulation of the retinal neural network. *Vision Res*, 48:1562–1568.

[55] Jensen, R. and Rizzo, J., 2009. Activation of ganglion cells in wild-type and rd1 mouse retinas with monophasic and biphasic current pulses. *J Neural Eng*, 6:035004.

[56] Jensen, R. and Rizzo, J.r., 2011. Effects of GABA receptor antagonists on thresholds of P23H rat retinal ganglion cells to electrical stimulation of the retina. *J Neural Eng*, 8:035002.

[57] Jensen, R., 2012. Activation of ganglion cells in wild-type and P23H rat retinas with a small subretinal electrode. *Exp Eye Res*, 99:71–77.

[58] Ye, J., Kim, K., and Goo, Y., 2008. Comparison of electrically-evoked ganglion cell responses in normal and degenerate retina. *Conf Proc IEEE Eng Med Biol Soc*, 2008:2465–2468.

[59] Rizzo, J.F., Wyatt, J., Loewenstein, J., Kelly, S., and Shire, D., 2003. Perceptual efficacy of electrical stimulation of human retina with a microelectrode array during short-term surgical trials. *Invest Ophthalmol Vis Sci*, 44:5362–5369.

[60] O'Hearn, T., Sadda, S., Weiland, J., Maia, M., Margalit, E., and Humayun, M., 2006. Electrical stimulation in normal and retinal degeneration (rd1) isolated mouse retina. *Vision Res*, 46:3198–3204.

[61] Suzuki, S., Humayun, M.S., Weiland, J.D., Chen, S.J., Margalit, E., Piyathaisere, D.V., and de Juan, E., J., 2004. Comparison of electrical stimulation thresholds in normal and retinal degenerated mouse retina. *Jpn J Ophthalmol*, 48:345–349.

[62] Sekirnjak, C., Hulse, C., Jepson, L., Hottowy, P., Sher, A., Dabrowski, W., Litke, A., and Chichilnisky, E., 2009. Loss of responses to visual but not electrical stimulation in ganglion cells of rats with severe photoreceptor degeneration. *J Neurophysiol*, 102:3260–3269.

[63] Chan, L., Lee, E., Humayun, M., and Weiland, J., 2011. Both electrical stimulation thresholds and SMI-32-immunoreactive retinal ganglion cell density correlate with age in S334ter line 3 rat retina. *J Neurophysiol*, 105:2687–2697.

[64] Chen, S., Mahadevappa, M., Roizenblatt, R., Weiland, J., and Humayun, M., 2006. Neural responses elicited by electrical stimulation of the retina. *Trans Am Ophthalmol Soc*, 104:252–259.

Chapter 3

Spatially patterned electrical stimulation for improved spatial selectivity of retinal activation

Abstract

Current clinical retinal prostheses suffer from a lack of spatial specificity, resulting in indiscriminate stimulation of many distinct retinal ganglion cell (RGC) types over a large region of the retina. Re-creation of the complex natural spatiotemporal activity patterns of RGCs requires single-cell spatial resolution, because neighboring RGCs of different types often have very distinct responses to a visual stimulus. Single-cell resolution is difficult to achieve with monopolar stimulation, even using high-density electrode arrays. Here we investigate the potential of simultaneous current injection with spatial patterns of electrodes for improving spatial specificity, using an *in vitro* model of the epiretinal interface. We found that current injection through pairs and triplets of neighboring electrodes modulated RGC activation thresholds, and that this modulation could be described by a simple empirical model. We demonstrated that spatial patterns of current injection could improve selectivity of activation in comparison to single-electrode stimulation, using the model to accurately predict which among a set of tested spatial

patterns provided the greatest selectivity. Thus, simultaneous current injection through patterns of electrodes may be useful for improving the selectivity achievable with epiretinal prostheses, allowing for more accurate recreation of natural RGC activity patterns.

3.1 Introduction

Retinal prostheses have the potential to restore visual function to patients with photoreceptor degenerations, such as retinitis pigmentosa and age-related macular degeneration. In a healthy retina, the photoreceptors perform the initial transduction of incoming light into neural signals [1]. These signals are then processed by the retinal interneurons and finally transmitted to the brain by the retinal ganglion cells (RGCs). Epiretinal prostheses are designed to provide an alternative to light-driven input in retinas with degenerated photoreceptors by electrically activating the remaining inner retinal cells with an array of electrodes implanted on the inner surface of the retina [2].

Current epiretinal prostheses designed for clinical use have relatively large electrodes (100-520 μm in diameter) that are coarsely spaced (300-800 μm center-to-center) [3–6]. These electrode densities are vastly lower than the density of the RGCs. As a result, each electrode is likely to stimulate hundreds of RGCs indiscriminately. Indiscriminate activation of groups of neighboring RGCs not only decreases the spatial resolution of the visual information transmitted from the prosthesis to the visual system, but also generates highly unnatural patterns of activity in the RGCs. In a healthy human retina, RGCs that are physically located near each other in the retina often respond very differently to a visual stimulus. This is because different aspects of visual information are transmitted by $\sim$20 different RGC types [7], and these RGC types are spatially intermixed in the retina (see Section 1.5.2). Therefore, it is not surprising that patients with current clinical implants, which are likely to simultaneously activate a mixture of several different RGC types with each stimulus pulse, experience variable percepts [3, 4, 8, 9] and can only perform relatively simple visual tasks [4, 10–14].

To improve the quality of the artificial visual signal provided by an epiretinal prosthesis, electrical stimulation should faithfully reproduce the complex spatiotemporal activity patterns that occur naturally in RGCs. An ideal prosthesis would be capable of independently stimulating each RGC with high temporal precision, allowing for recreation of arbitrary activity patterns in the population of RGCs. Our examination of the responses of the highest-density primate RGC types suggest that single-cell selectivity is only sometimes possible using individual electrodes with a distant return (monopolar stimulation), even when using much higher density MEAs than current clinical prostheses, and in the peripheral retina where RGC density is relatively low (see Section 2.3.4). Although advances in array fabrication that lead to higher density clinical MEAs may improve the selectivity of monopolar stimulation, approaching the density of RGCs near the fovea is likely to be a challenge, so other methods to improve the spatial resolution of stimulation will always be valuable.

Therefore, we explored the potential of using more complex electrical stimuli to improve the selectivity of RGC activation. Specifically, we examined whether current passed through multiple electrodes simultaneously in particular spatial patterns and current ratios could modulate the responses of RGCs in predictable ways that could potentially be used to improve selectivity. This approach, sometimes referred to as “current steering” or “current focusing” has been used successfully at coarser scales in other neural stimulation devices, such as cochlear prostheses [15, 16] and deep brain stimulation [17, 18], to more precisely control the region of neural tissue activated by electrical stimulation. It is currently unclear, however, whether this approach would still be useful for improving spatial selectivity when using electrodes sizes and densities that approach the size and density of the targeted neurons.

Here, we demonstrate that current passed simultaneously through spatial patterns of electrodes spaced 30 or 60 μm apart can be used to modulate the activation thresholds of individual RGCs. We propose a simple empirical model to describe threshold modulation by current injection with electrode pairs, and show that the measured modulatory effects of electrode pairs accurately predict responses to more complex spatial patterns of electrodes. We then investigated the relationship of the model parameters to axon orientation and to the signal generated by spikes of the target RGC on each electrode of the array. Finally, we demonstrate the utility of spatial patterns of current injection for improving selectivity in comparison to monopolar stimulation by showing that the empirical model can be used to accurately predict spatial patterns that optimize selectivity for a particular RGC.

3.2 Methods

3.2.1 Experimental setup

Isolated primate retina patches were mounted on a multielectrode array (MEA), as described previously [19, 20] (see Section 2.2.1). Briefly, the eyes of terminally anesthetized macaque monkeys (*Macaca mulatta*) were removed and immediately hemisected in room light. After removing the vitreous, the posterior portion of the eye was maintained in darkness in oxygenated bicarbonate-buffered Ames' solution (Sigma, St. Louis, MO). Under infrared illumination, 1-2 mm diameter patches of intact retina were isolated and placed RGC-side down on a custom MEA. A dialysis membrane placed on the photoreceptor side of the retina membrane held the retina in place against the MEA. Dim red illumination was used briefly while mounting the MEA in the electrical stimulation and recording system. Throughout the experiment, the retina was superfused with $\sim 33^\circ$C Ames' solution. In total, data 15 RGCs recorded in 10 preparations from 10 monkeys were collected and analyzed.

3.2.2 Electrical stimulation and recording

A custom multichannel electrical stimulation system [21] was used in conjunction with MEAs to electrically stimulate and record from the isolated retina. The MEAs consist of 61 hexagonally-packed indium tin oxide electrodes on a glass substrate, electroplated with platinum black [22–24]. Final platinum electrode

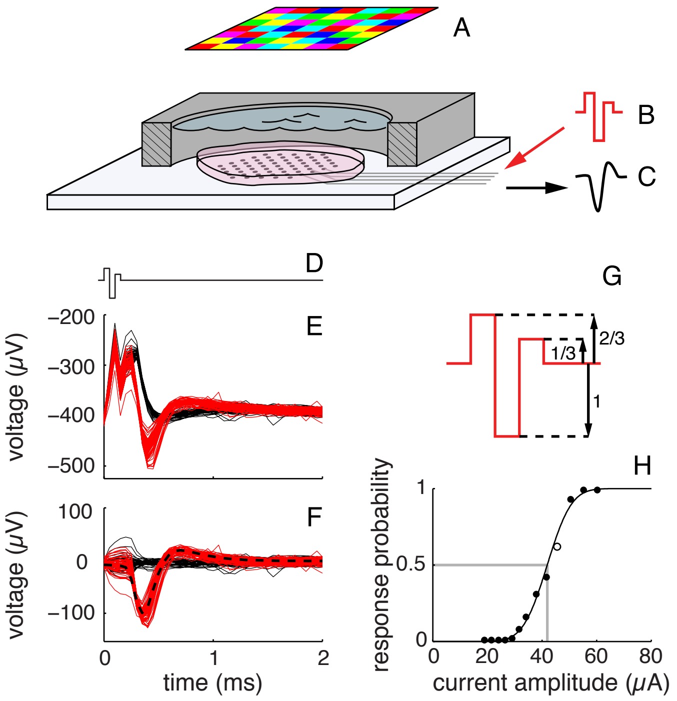

Figure 3.1: *In vitro* retinal preparation schematic and analysis of responses to electrical stimulation. RGC spikes were recorded (C) with a 61-electrode MEA while either electrical (B) or visual (A) stimuli were applied. (G) Triphasic current pulse waveform with relative phase amplitudes. (E) Raw voltage traces recorded on the stimulus electrode during and after 100 stimulation trials in which a single current pulse (D) is applied. Red traces denote successes and black traces denote failures. (F) The same 100 trials, after subtracting the average electrical artifact trace. Dashed black line shows the spike waveform of the RGC, based on spikes recording during visual stimulation. (H) Response curve, showing the measured response probabilities over a range of current pulse amplitudes and the cumulative Gaussian fit. Open circle denotes stimulus amplitude applied in E and F. ©IEEE 2011.

diameters ranged from ~10-20 μm, and were spaced either 30-33.5 or 60-67 μm apart. The stimulation and recording system was used to independently control the current injected through each electrode, while simultaneously recording from all electrodes. Artifact-reduction circuitry prevented saturation of recorded voltages during pulse application, permitting detection of low-latency (<1 ms) RGC responses on all electrodes including the electrode used for stimulation. Charge-balanced triphasic current pulses with 50 or 100 μs phase widths were chosen to further minimize electrical artifacts (Fig. 3.1G) [25]. All reported pulse amplitudes reflect the amplitude of the second phase. A ring of platinum wire around the edge of the recording chamber served as a distant ground. MEA recordings were band-pass filtered between 43 and 2000 Hz or 43 and 5000 Hz (-3 dB), amplified and digitized at 20 kHz for offline analysis.

3.2.3 Visual stimulation

As described previously [26] (Section 2.2.3), a randomly flickering checkerboard stimulus was used to elicit RGC responses for RGC identification and measurement of visual response properties. The stimulus, which was displayed on a cathode ray tube computer monitor, was optically reduced and focused through a microscope objective onto the photoreceptor outer segments. The stimulus was maintained at low photopic intensity with neutral density filters.

3.2.4 Spike sorting

Spike waveforms of individual RGCs were extracted from recordings of responses to visual stimulation, as described previously [19]. Briefly, potential RGC spikes recorded during visual stimulation were detected by thresholding the voltage trace at 4 times the root mean square of the noise on each electrode. Waveform vectors for each potential spike were generated by extracting the voltage recorded on the electrode that recorded the threshold-crossing event and the 6 nearest-neighboring electrodes within a brief time window around the threshold crossing. Waveform vectors were projected onto the first five principal components and clustered by fitting a mixture of Gaussians model using expectation maximization. The clusters of threshold-crossing events that contained no or few refractory period violations and that exceeded a minimum spike rate were interpreted as spikes generated by individual RGCs.

3.2.5 Electrophysiological image

An *electrophysiological image* (EI), the average voltage waveforms generated on the electrodes of the MEA each time a particular RGC spikes, was calculated from the visual response data, as described previously [27] (section 2.2.5). The EI of each RGC was used to estimate the soma location and axon orientation. The EI waveforms on electrodes in the vicinity of the soma of an RGC were characterized by a biphasic shape and large amplitude (Fig. 3.2). Signals recorded by electrodes near the axon of an RGC had a distinct initial positive deflection, characteristic of axonal signals, and were displaced in time relative to the somatic signal as a result of spike propagation down the axon [28].

3.2.6 Analysis of electrically-evoked responses

RGC responses to electrical stimuli were determined by clustering trials of each stimulus pattern and amplitude according to voltage waveform (Fig. 3.1E) into trials containing only stimulus artifact (“failures” Fig. 3.1E black traces) and trials containing a spike from the target RGC in addition to the stimulus artifact (“successes” Fig. 3.1E red traces). This clustering was performed using a combination of automated and manual spike-sorting, as described previously (section 2.2.6). Briefly, a custom automated algorithm was used to classify traces based on an initial estimate of the artifact waveform and the spike waveform taken from the of the targeted cell. All clustering results were visually inspected for errors and manually corrected when necessary. Following clustering, the electrical artifact, calculated as the mean of the voltage traces not containing a spike, was subtracted from all voltage traces, revealing the uncontaminated spike waveform (Fig. 3.1F red traces). This uncontaminated waveform was then compared to the spike wave-

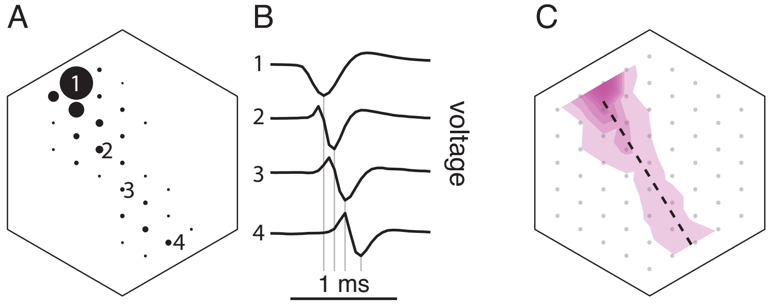

Figure 3.2: Estimation of soma position and axon orientation from the EI. (A) The amplitude (absolute value) of the EI waveform on each electrode of the MEA, represented as the diameter of the black circle at each electrode position. The large amplitude signal on electrode 1 corresponds with the soma location, and the smaller signals on electrodes extending down and to the right correspond with the axon location. (B) EI voltage waveforms of the 4 electrodes labeled in (A), showing the signature biphasic somatic signal (1) and triphasic axon signals (2-4) at time delays that increase with distance from the soma as a result of action potential propagation. Voltages have been scaled to have equal amplitude. (C) An example of an estimated axon orientation, fit by eye (dashed line). Shading depicts contours based on the EI waveform amplitude on each electrode.

form of the targeted RGC (Fig. 3.1F black dashed line) to confirm the identity of the responding RGC.

3.2.7 Threshold measurement

After measuring the response probability of a target RGC to a particular stimulus pattern over a range of pulse amplitudes, a cumulative Gaussian distribution was fit to the data (Fig. 3.1H), as described previously (section 3.2.7). The threshold current amplitude, defined as the current amplitude required to elicit a response with 0.5 probability, was extracted from the curve fit. Activation ranges depicted as shaded regions in Fig. 3.3, 3.4 and 3.5 correspond to stimulus amplitudes of the fit cumulative Gaussian lying between 0.16 and 0.84 response probability.

3.2.8 Stimulus patterns

Electrical stimuli consisted of current pulses applied through a single electrode or simultaneously through 2-3 electrodes in chosen amplitude ratios (spatial patterns). For each targeted RGC, a “primary” electrode was chosen. With one exception (see below), the primary electrode was the electrode that resulted in the lowest activation threshold, as identified by analyzing the responses of the RGC to single-electrode stimulation with electrodes near the estimated soma position (see Section 2.2.9). In one case, two RGCs were activated by the same primary electrode, and one of these two RGCs was activated with lower threshold by a neighboring electrode. Spatial patterns of current amplitudes using this primary electrode and one or more of the nearest-neighboring (“secondary”) electrodes were then generated. Each spatial pattern was defined by relative current amplitudes on a set of 2-3 stimulus electrodes, in which the secondary electrode amplitudes were defined relative to the primary electrode amplitude. Spatial patterns were applied over a chosen range of primary electrode pulse amplitudes (“base” amplitudes) in 10% increments. The amplitude of a particular secondary electrode in the pattern was the product of this base amplitude and the relative amplitude of that secondary electrode.

At each base amplitude, the entire set of spatial patterns was applied in random order for 50 or 100 repetitions. Sequential spatial patterns associated with a particular primary electrode were applied in 30 ms intervals. When more than one primary electrode was used to generate spatial patterns in a single preparation, the patterns associated with each primary electrode were interleaved, with either 15 ms (2 primary electrodes) or 10 ms (3 primary electrodes) between sequential patterns.

3.2.9 Linear model fitting (single region)

The linear model parameters λ_i and $f^{-1}(0.5)$ (see Eqn. 3.5) were determined for each secondary electrode by fitting a line to the thresholds measured in response to the set of tested current combinations. The line was fit by minimizing the sum of the squared distances from each measured threshold to the line, where distances were measured perpendicular to the line, using a standard nonlinear search algorithm (Nelder-Mead simplex direct search). The linear fits for each set of 6 secondary electrodes were constrained to intersect the axis defined by 0 secondary current at the same location (i.e., $f^{-1}(0.5)$ of Eqn. 3.5 was constrained to be equal for all secondary electrodes).

3.2.10 Nonlinearity index

A nonlinearity index was calculated to assess the quality of the linear fit for each secondary electrode. This value was defined as the sum of the squared distance of each measured threshold from the fit line (used as the objective function for fitting the linear model, see Section 3.2.9), normalized by (1) the number of measured thresholds being fit and (2) the squared diagonal distance of stimulus space containing measured thresholds (the sum of the squared range of the set of threshold primary current amplitudes and the squared range of the set of threshold secondary current amplitudes):

$$\frac{1}{NR^2}\sum_{j}^{N} D\left(I_{0j}, I_{ij}\right)^2 \tag{3.1}$$

where R represents the diagonal distance of the stimulus space (see Eqn. 3.2), N indicates the number of measured thresholds, i is the secondary electrode index, and $D(I_{0j}, I_{i,j})$ is the perpendicular distance from the measured threshold of the jth tested current ratio to the fit line.

$$R^2 = \left[\Big(\max_j\left(\{I_{0j}\}\right) - \min_j\left(\{I_{0j}\}\right)\Big)^2 + \Big(\max_j\left(\{I_{ij}\}\right) - \min_j\left(\{I_{ij}\}\right)\Big)^2\right] \tag{3.2}$$

Here, $\min_j(I_{0j})$ and $\max_j(I_{0j})$ are the minimum and maximum of the set of threshold primary electrode current amplitudes and $\min_j(I_{ij})$ and $\max_j(I_{ij})$ are the minimum and maximum of the set of threshold secondary electrode current amplitudes.

3.2.11 Piecewise linear model fitting

A piecewise linear model was fit to a subset of the paired electrode data to account for observed large nonlinearities. To avoid overfitting, only secondary electrodes with a nonlinearity index greater than 2x10^{-4} were considered for fitting with a piecewise linear model. For secondary electrodes that met this criterion, if a measurable threshold (minimum observed response probability of 0.4 for at least one stimulus amplitude) existed for stimulation with the secondary electrode alone within the range of tested current values (for either pulse polarity), an additional linear model was added for the region of stimulus space containing this threshold. If the cell did not have a measurable threshold to stimulation with the secondary electrode alone, it was excluded from the piecewise linear model fitting. The full piecewise linear model was then fit based on the sum of squared minimum distance objective function described above (Section 3.2.9), with each measured threshold assigned to one of the regions of stimulus space according to which set of assignments yielded the minimum value of the objective function. If any region of the resulting fits contained only one threshold, resulting in an underconstrained linear model for the region, the linear model for the region was removed and the fitting repeated using only the remaining linear models. Of the 6 secondary electrodes that both exceeded the threshold nonlinearity index and contained at least one measured threshold to stimulation with the secondary electrode alone, 5 were successfully fit with a piecewise linear model. Attempts at fitting the remaining RGC resulted in an underconstrained linear model region.

3.2.12 Analysis of electrode triplet patterns

Responses to electrode triplet patterns were assessed by comparing measured activation thresholds to those predicted by the full linear model, using the model parameters ($f^{-1}(0.5)$, λ_1, λ_2, … λ_6) extracted from the linear fits to paired-electrode responses. Values plotted in Fig. 3.7 are normalized to $f^{-1}(0.5)$, which corresponds to the model prediction for the threshold to stimulation using the primary electrode alone. For RGCs requiring piecewise linear fitting of paired electrode responses, the triplet pattern analysis was restricted to patterns for which both relative secondary electrode amplitudes (I_i/I_0) fell within the region of stimulus space containing the primary-alone stimulus (blue regions in Fig. 3.7).

3.2.13 Axon orientation analysis

A mean axon orientation was calculated for each retinal preparation. First, a set of 3-12 RGCs with clear axonal signals was chosen. A line were then hand-fit to the set of electrodes with the highest-amplitude axonal EI signals for each RGC (Fig. 3.2C) and the mean orientation of the hand-fit lines over the chosen RGCs in a given preparation was calculated. This mean axon orientation was used to determine the relative angle between pairs of stimulation electrodes and axon angle. The angle of each pair of electrodes was defined as the angle of the vector starting from the primary electrode location and ending at the secondary electrode location. Relative angles were constrained to the interval $[0, 180°]$ by reflecting all angles $> 180°$ across the axis defined by $0°$ (x-axis in Fig 3.11A,C).

To quantify the nonuniformity of modulatory effects across relative axon angles, the measured λ values (Eqn. 3.3) of all secondary electrodes for a given electrode spacing were binned into one of three bins according to relative axon angle (0°-60°, 60°-120°, or 120°-180°). An *anisotropy index*, defined as the sum of the squared differences between the mean lambda value in each bin and the mean lambda value over all bins (Eqn. 3.6), was calculated. Because the relationship between axon angle and modulatory effect could depend on the region of the RGC that is being activated, data from the one cell for which the primary electrode in the stimulation pattern did not yield the lowest threshold (i.e., the primary electrode was not located at the region of highest sensitivity to electrical stimulation) were excluded. Anisotropy indices were calculated separately for 30 and 60 μm electrode spacings.

A "random rotation analysis" was performed to assess the significance of any observed trend in the relationship between relative axon angle and modulatory effect of a secondary electrode. For each iteration of the random rotation analysis, a different random angle between 0 and 360° was added to the axon angle of each analyzed cell, and the anisotropy index recalculated. This was iterated 50,000 to generate the distribution of anisotropy indices expected if there was no correlation between relative axon angle and modulatory effect. P-values were calculated as the fraction of anisotropy values generated by random rotation analysis that exceeded the anisotropy values calculated for the original data for each electrode spacing.

3.3 Results

To determine how RGCs respond to spatial patterns of current injection, we stimulated RGCs with a range of current pulse amplitude and polarity combinations applied with spatial patterns of electrodes in an *in vitro* MEA primate retinal preparation.

3.3.1 Threshold modulation with electrode pairs: linear prediction

In the absence of a detailed biophysical model of each RGC to be activated, an approximation that would allow for predictions of RGC responses to arbitrary spatial patterns of current injection would be useful for determining the optimal stimulus pattern for selective activation of a particular RGC. The simplest and most computationally tractable hypothesis for the way in which currents from multiple sources combine to influence the response of a RGC is that they combine linearly:

$$P = f\left(I_0 + \lambda_1 I_1 + \lambda_2 I_2 + \ldots + \lambda_n I_n\right) \tag{3.3}$$

where P is the probability of the RGC response, f describes the nonlinear dependance of response probability on stimulus amplitude, $I_0, I_1, I_2, ..., I_n$ denote the current amplitudes applied by each electrode in a stimulus pattern and $\lambda_1, \lambda_2, ..., \lambda_n$ describe the modulatory effect of each electrode.

3.3.2 Threshold modulation with electrode pairs: test of linearity

This hypothesis was first tested by examining the responses of RGCs to the simplest spatial pattern of stimulus electrodes, pairs of neighboring electrodes. For each target RGC, a “primary” stimulation electrode was chosen (see Section 3.2.8). The RGC responses to simultaneous current injection through each of the 6 neighboring “secondary” electrodes in combination with the primary electrode were then measured. Relative current amplitudes and polarities of the secondary electrodes were systematically varied and the threshold for each pattern was determined. In total, 15 RGCs from 10 retina preparations were investigated, with 6 to 10 current ratios tested on each of 6 electrode pairs for each cell.

As predicted by the linear model, the current passed through the two electrodes of each pair traded off in fixed proportion to influence measured thresholds, at least over a range of relative current amplitudes. Specifically, the threshold, in

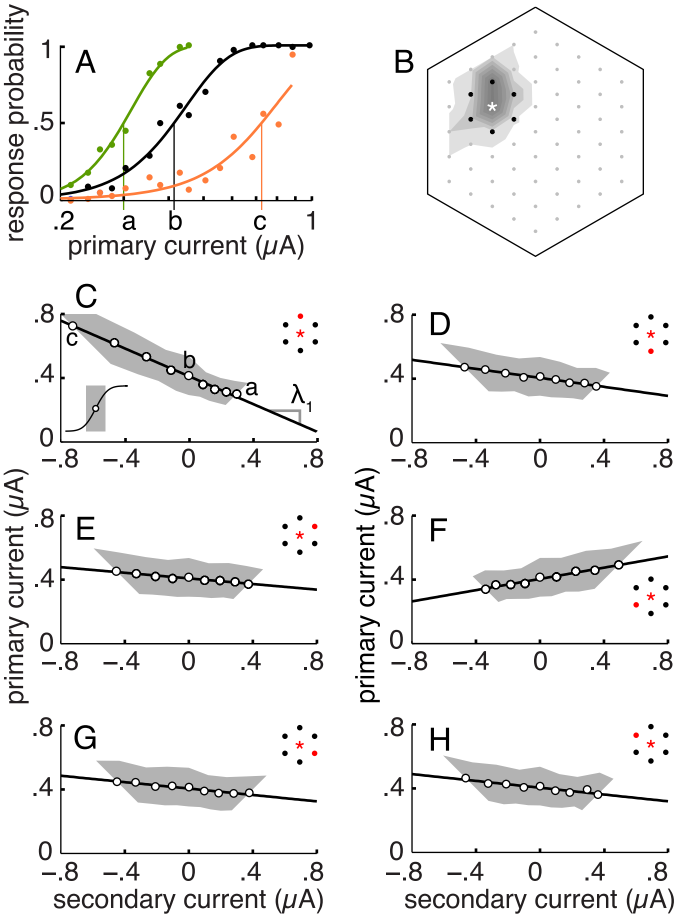

Figure 3.3: Linearity of threshold modulation by simultaneous current injection through pairs of electrodes. (A) Response curves resulting from current injected through the primary electrode alone (black), from equal amplitude, same polarity current passed simultaneously through one secondary electrode (green), and from equal amplitude, opposite polarity current passed through the same secondary electrode (orange). (B) Layout of primary (white asterisk) and secondary (black dots) electrodes relative to EI of RGC (shaded contours). (C) Measured thresholds for each current ratio tested using the electrode pair depicted in A. Grey region indicates dynamic range of the response curve (inset, see Section 3.2.7), and black line depicts linear fit to the measured thresholds (isoresponse contour). Negative secondary currents signify opposite polarity pulses relative to the pulse polarity of the primary electrode. (D-H) Measured thresholds and isoresponse contours for the other 5 secondary electrodes. Inset in each shows corresponding pair of electrodes (red). ©IEEE 2011.

terms of the primary electrode current amplitude, was proportional to the magnitude and sign (polarity) of the current injected through the secondary electrode (Fig. 3.3). However, the constant of proportionality (λ value) was not the same for all electrode pairs for a given cell. The modulatory effect of a secondary electrode was visualized by plotting activation thresholds in terms of the current amplitude on each electrode in the pair, where negative current amplitudes signify opposite polarity stimuli (Fig. 3.3C-H). The fact that the observed thresholds fell on a straight line (isoresponse contour) through this stimulus space reflects the linearity of the modulatory effect, and the different slopes observed for different secondary electrodes illustrate the distinct effect of each secondary electrode.

The line fit to the set of measured thresholds for each secondary electrode (see Section 3.2.9) was used to extract the value of the corresponding λ using the following equation (for secondary electrode 1):

$$I_0 = f^{-1}(0.5) - \lambda_1 I_1 \tag{3.4}$$

Here, $f^{-1}(0.5)$ is the stimulation threshold to current injection through the primary electrode alone (y-intercept of the fit line). The threshold shift resulting from simultaneous injection of current amplitude I_1 through secondary electrode 1 in combination with the primary electrode corresponds to a vertical threshold shift in Fig. 3.3C-H, and the value λ_1 is the negative of the slope of the line fit to the measured thresholds (Fig. 3.3C). In most cases, injecting same-polarity current through a secondary electrode led to a decrease in threshold (positive λ), with opposite-polarity current resulting in an increase in threshold. In some cases the opposite effect was observed (see section 3.4.1), but the dependence of threshold on secondary electrode current remained linear.

Overall, the threshold modulatory effect of the majority of tested secondary electrodes was highly linear. To quantify the linearity of each secondary electrode effect, a nonlinearity index was calculated (see Section 3.2.10). Briefly, this index reflects the sum of squared distances from the observed thresholds to the linear fits. The nonlinearity indices for all 90 tested secondary electrodes are shown as a histogram in Fig. 3.4A, along with 4 example secondary electrodes.

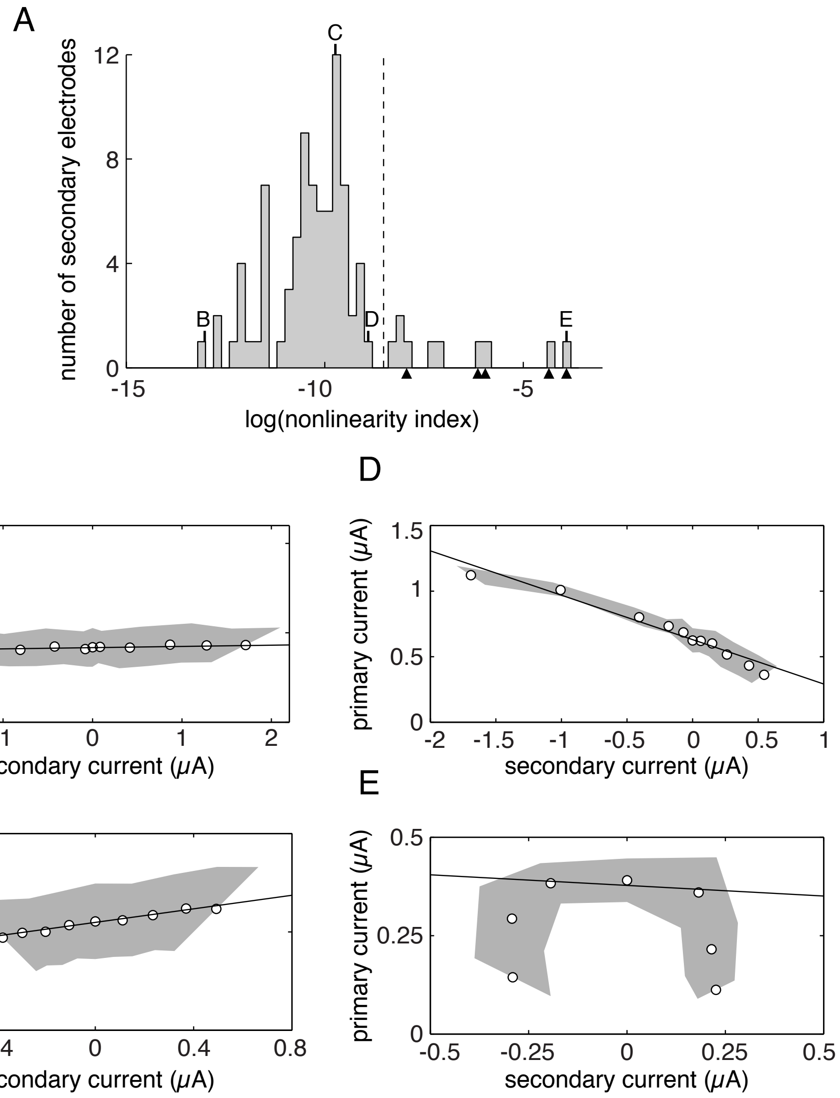

Figure 3.4: Linearity of threshold modulation of all tested electrode pairs. (A) A histogram of all observed nonlinearity indices (see Section 3.2.10). Letters indicate nonlinearity indices of example secondary electrodes shown in B-E, and triangles indicate the nonlinearity indices of the examples in Fig. 3.5. Vertical dashed line indicates the minimum nonlinearity index required to attempt fitting with a piecewise linear model (see Sections 3.2.11, 3.3.3). (B-E) Measured thresholds and linear fits of 4 example electrodes, illustrating the range of observed nonlinearities. Shaded regions indicate dynamic range of response curves (see Fig. 3.3C inset).

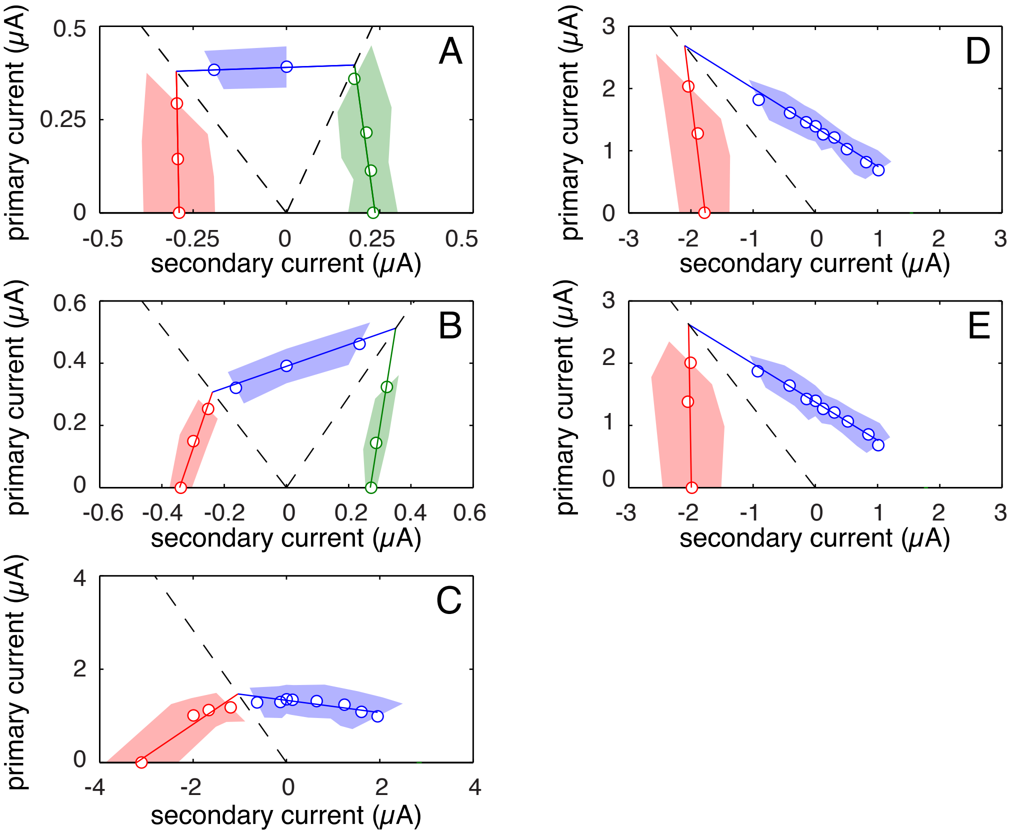

Figure 3.5: Piecewise linear fitting of electrode pairs with nonlinear modulatory effects. Open circles are measured thresholds, colored according to the region of stimulus space to which they are assigned (see Section 3.2.11). Linear model fits are shown as colored lines. Dashed lines indicate boundaries between stimulus space regions. Shaded regions indicate dynamic range of response curve fits (see Fig. 3.3C inset).

3.3.3 Piecewise linear model

A subset of the examined secondary electrodes exhibited highly nonlinear modulatory effects for large secondary electrode current amplitudes. The observed nonlinearities were consistent with a switch between which electrode of the pair provided the main driving force for RGC activation (see Section 3.4.1 for a biophysically-motivated interpretation of this piecewise linearity). If this interpretation is correct, a separate linear model would be expected to exist for each region of stimulus space for which a particular electrode provides the main depolarizing influence. Indeed, the nonlinearities could be accounted for by dividing the stimulus space into regions, with each region containing a separate linear model. This extension of the model also accounted for the observation that in some cases, the targeted RGC could be activated by a secondary electrode alone (Fig. 3.5, points on x-axes).

3.3.4 Threshold modulation with electrode triplets: linear prediction

The predictions of the full linear model (Eqn. 3.3) can be extended to more complex patterns: when currents are injected through more than one secondary electrode along with the primary electrode, the modulatory effects of the secondary electrodes are predicted to be additive. This additivity can be more easily interpreted by considering the shift in threshold, in terms of primary electrode current, that is predicted to occur when applying a combination of currents through multiple secondary electrodes:

$$I_0 = f^{-1}(0.5) - \lambda_1 I_1 - \lambda_2 I_2 - \ldots - \lambda_n I_n \tag{3.5}$$

The threshold shift resulting from a particular set of secondary electrode currents I_1, $I_2 \ldots I_n$ applied simultaneously with the primary electrode should simply be the sum of shifts resulting from each secondary electrode current applied individually in combination with the primary electrode (see Fig. 3.6).

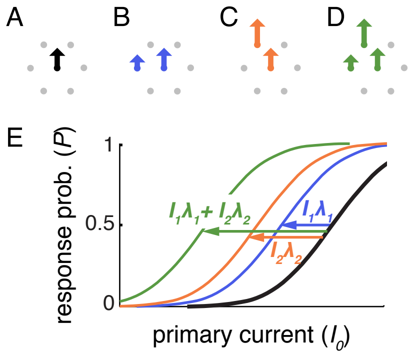

Figure 3.6: Illustration of expected threshold shift produced by a pair of secondary electrodes. (A-D) Schematics of current patterns: stimulation with (A) the primary electrode alone, (B) the primary electrode and secondary electrode 1 with pulse amplitude I_1 (C) the primary electrode and secondary electrode 2 with pulse amplitude I_2, and (D) primary electrode and secondary electrodes 1 and 2 with pulse amplitudes I_1 and I_2 respectively. (E) Expected shifts in response curve from primary-alone stimulation. ©IEEE 2011.

3.3.5 Threshold modulation with electrode triplets: test of linearity

The validity of this model prediction was tested by measuring the responses of RGCs to current passed through triplets of electrodes consisting of the primary electrode and pairs of neighboring secondary electrodes. The resulting thresholds were compared to the thresholds predicted by the model, based on the λ_i values extracted from the linear fits to paired electrode stimulation. Because the λ_i values of the 5 secondary electrodes shown in Fig. 3.5 were only valid within the "central" region of stimulus space (region containing the threshold to stimulation with the primary electrode alone), triplet patterns containing relative secondary electrode current amplitudes outside of this region were excluded from this analysis.

The linear model prediction of responses to electrode triplets was tested in 5 cells. Results are shown in Figure 3.7. Although some deviations from linearity are visible, the measured thresholds show good agreement with the linear model, with coefficients of determination between the linear model and the measured threshold shifts (R^2 values) ranging from 0.72 to 0.91.

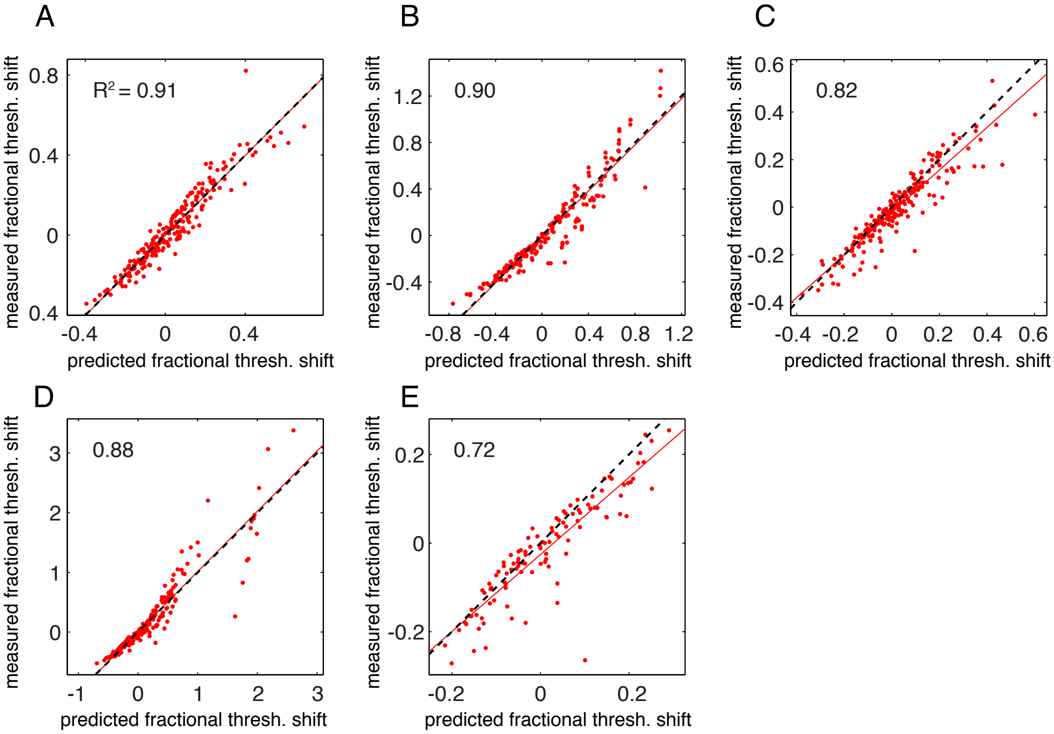

Figure 3.7: Comparison of observed threshold shifts to linear model predictions for stimulation with electrode triplet patterns. Each panel corresponds to one tested RGC. Red points are measured fractional shifts in threshold from $f^{-1}(0.5)$, the model primary-alone threshold, plotted as a function of the threshold shift predicted by the linear model. Dashed black lines indicate 1:1 correspondence between predicted and measured values, and solid red lines depict linear least-squares fits to the data. Coefficients of determination (R^2 values), indicating the proportion of measured variance in the data that is explained by the linear model, are shown in the upper left of each panel.

3.3.6 Example of improved selectivity

To test the whether the linear model could accurately predict a spatial pattern that optimizes selectivity for a particular RGC, the responses of a pair of cells, an ON parasol cell (Fig. 3.8A) and an OFF parasol cell (Fig. 3.8B) that were equally activated by one primary electrode were examined. First, the selectivity achievable using single-electrode stimulation was assessed by examining the responses of each RGC to stimulation with the primary electrode and each of the secondary electrodes used individually. For each of the individual stimulation electrodes that activated one or both of the RGCs within the tested current range, the two RGCs were either activated approximately equally (Fig. 3.8G), or the ON parasol was activated more strongly (Fig. 3.8E,I,F). Thus, single-electrode stimulation was not capable of selectively activating the OFF parasol cell.

Next, the modulatory effects of each secondary electrode ($\lambda_1, \ldots, \lambda_6$) for each cell were determined based on the measured responses to paired-electrode stimulation. The linear model was then used to predict which of the tested 3-electrode stimulation patterns would result in the greatest selectivity of the OFF parasol cell, based on the predicted difference in threshold between the two RGCs. The spatial pattern that was predicted to be optimally selective for the OFF parasol cell did in fact achieve high selectivity, allowing for activation of the OFF parasol cell with 0.9 probability at a current amplitude that only activated the ON parasol with 0.11 probability (Fig. 3.9A, horizontal dashed lines), based on response curve fits to the measured RGC responses. This was a substantial improvement over the best selectivity achievable with a single electrode, in which the ON parasol cell was activated with 0.98 probability at the amplitude required to activate the OFF parasol with 0.9 probability (Fig. 3.9C). The selectivity achieved by the predicted optimal pattern was also nearly identical to the selectivity achieved by the pattern with the largest measured threshold difference (Fig. 3.9B).

The overall performance of the model prediction was assessed by comparing the predicted and measured difference in threshold between the two cells for each pattern. In Fig. 3.9D, the threshold difference predicted by the model is shown (black), ordered from most selective for the OFF parasol to the least (left to

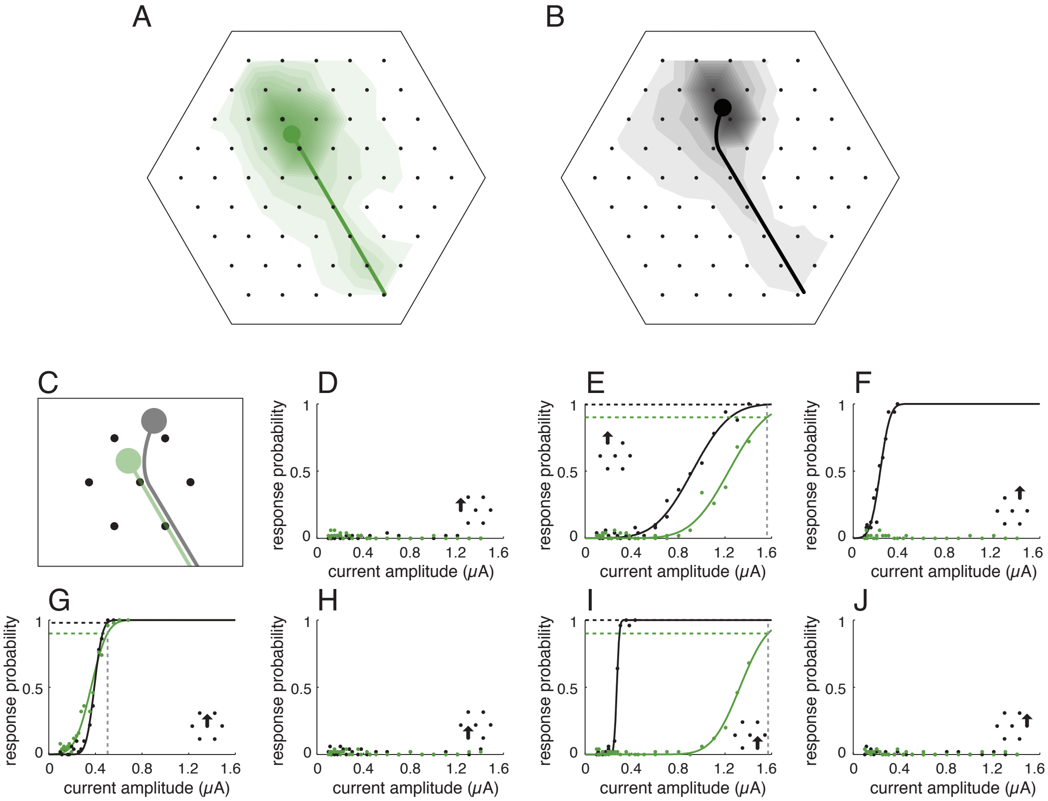

Figure 3.8: Lack of selectivity for one RGC using single-electrode stimulation. Each RGC is depicted as shading based on contours fit to EI amplitudes of the OFF parasol cell (A) and ON parasol cell (B), with an illustration of the inferred soma and axon position. (C) Set of 7 electrodes (primary electrode and 6 secondary electrodes) used in stimulation patterns, relative to inferred RGC positions (OFF parasol in green, ON parasol in grey). (D-J) Response probabilities and response curve fits of the two cells when stimulating with each of the 7 electrodes individually (stimulus electrode indicated by inset). Vertical dashed grey lines indicate current amplitude required to activate the OFF parasol cell (green) with 0.9 probability, and dashed horizontal lines indicate response probability of each cell at this amplitude, based on response curve fits.

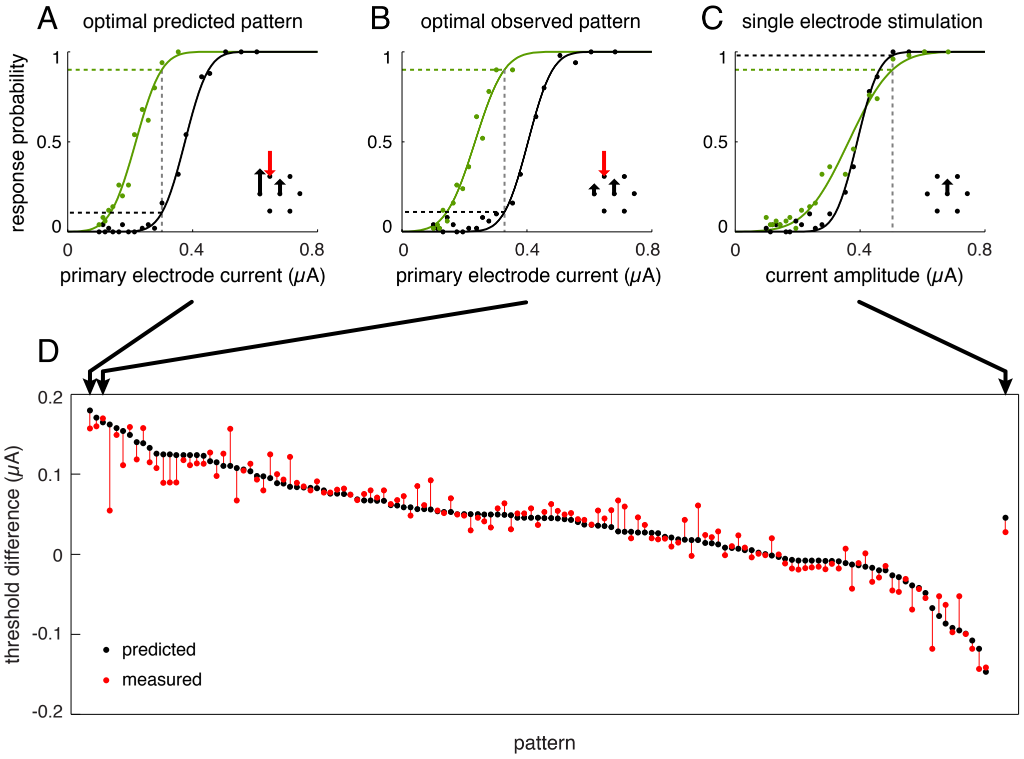

Figure 3.9: Performance of predicted optimal spatial pattern for selective activation. (A) Response probabilities and response curve fits of the ON parasol (black) and OFF parasol cell (green) for the stimulation pattern predicted to be optimal for selective activation of the OFF parasol, in terms of threshold difference, by the linear model. Inset shows stimulus pattern, with arrow lengths representing relative current amplitudes and colors indicating polarities relative to the primary electrode (same polarity in black, opposite polarity in red). Vertical dashed line indicates current amplitude required to activate the OFF parasol cell at 0.9 probability, and horizontal dashed lines show the response probability of each cell at this amplitude, based on the response curve fits. (B) Responses to stimulation with the measured optimal pattern, in terms of threshold difference. (C) Responses to stimulation with the most selective single stimulus electrode. (D) Predicted (black) and measured (red) threshold differences for all spatial patterns, ordered by predicted selectivity. Threshold differences corresponding to single electrode stimulation in C are shown for comparison (rightmost points).

right), and compared to the measured threshold differences for the same patterns (red). Although the measured threshold differences deviated slightly from the model prediction for some patterns, in general the model was a strong predictor of measured selectivity.

3.3.7 Comparison of modulatory effect to EI amplitude

Before RGC responses to arbitrary spatial stimulation patterns can be predicted using the proposed linear model, the model parameters $\lambda_1, \lambda_2, \ldots \lambda_n$ must be determined. Direct measurement of these values, as has been performed here, requires collection and analysis of a significant amount of data, which may be difficult to achieve in a prosthesis. Correlation of these model parameters with a more easily measured quantity could provide a more tractable method. One possibility is the prediction of λ_i from the amplitude of the spike from that cell (EI amplitude) recorded on a given electrode. The EI amplitude might be expected to be predictive of the modulatory effect if the principal determinant of both the modulatory effect and spike amplitude of a particular electrode was the distance from the cell to the electrode, or another aspect of the retinal interface that is common to recording and stimulation, such as the the conductivity of the current path between the electrode and the location on the RGC where spike generation occurs.

The strength of correlation between λ value and EI amplitude was measured by calculating the coefficient of determination between EI amplitude of each secondary electrode, relative to the EI amplitude of the primary electrode, and measured λ values, pooled across RGCs. Because modulatory effects of secondary effects were substantially influenced by electrode spacing, with pairs of electrodes spaced 30 μm apart typically having larger and more positive λ values than pairs spaced 60 μm apart (data not shown), the analysis was performed separately for 30 μm and 60 μm electrode spacing. Only very weak correlations were observed for 30 μm electrode separation ($R^2 = 0.258$, data not shown) and no correlation was present for 60 μm separation ($R^2 = 0.001$, data not shown). Therefore, the amplitude of the voltage signal on a particular electrode generated by a RGC spike is

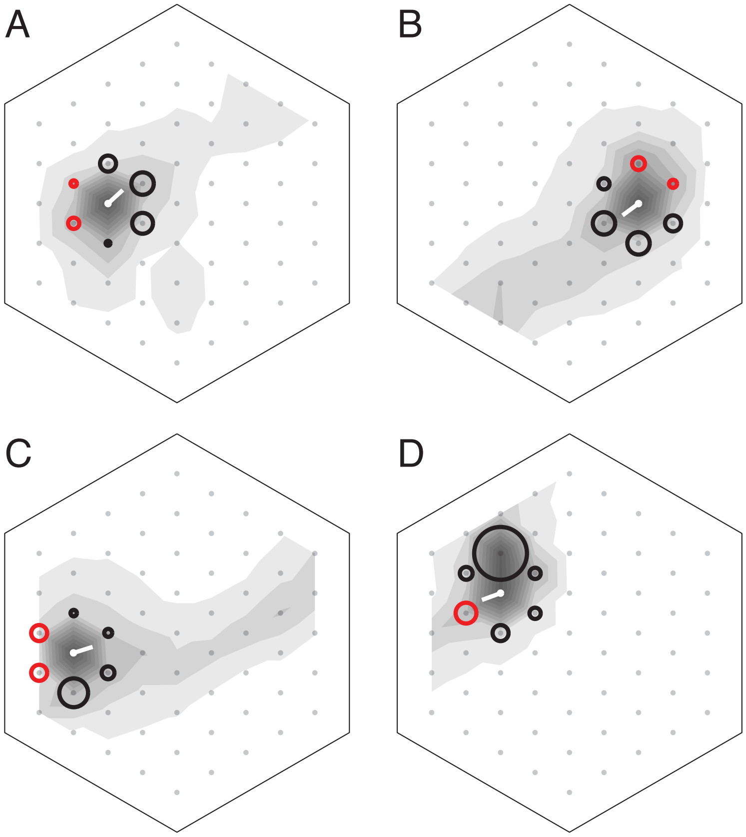

Figure 3.10: Example RGCs illustrating the relationship between modulatory effect and axon direction for 60 μm electrode spacing. (A-D) Four example RGCs. Grey shading depicts contours based on EI amplitudes and reflects the approximate location of the RGC soma and axon. Circles indicate modulatory effect of each secondary electrode (λ), with diameter corresponding to effect magnitude and color indicating effect sign (black for positive λ, red for negative λ). Each primary electrode is marked with a white dot, and white lines extending from the primary electrodes indicate the global axon direction of each preparation (see 3.2.13). RGCs shown in A-C are consistent with the overall trend for secondary electrodes lying opposite the axon direction to have negative λ values, and the RGC shown in D is an exception to this trend.

unlikely to be useful in predicting the modulatory effect of that electrode in spatial stimulation patterns.

3.3.8 Correlation of threshold modulation with axon orientation

Previous modeling and experimental work suggests that the orientation of an anistropic electric field relative to the neural element being stimulated can have a large effect on the response of a neuron [29–31]. In extracellular electrical stimulation of RGCs, the axon initial segment is thought to be the location of RGC spike initiation [32]. Together, these observations suggest that the response of a RGC to current injected through a particular pair of electrodes could be influenced by the orientation of the electrode pair relative to the RGC axon initial segment.

The influence of spatial pattern orientation on RGC responses was examined by comparing the modulatory effects of secondary electrodes to their position relative to the RGC axon. Because the precise orientation of the axon initial segment of each RGC could not be determined from the available data, the average axon direction of each retinal preparation, based on all recorded RGCs in the preparation with clear axon signals (see Section 3.2.13), was used as a proxy for initial segment orientation. Again, electrode pairs spaced by 30 μm and 60 μm were analyzed separately to remove the influence of electrode spacing on modulatory effect. No clear correlation between relative axon orientation and modulatory effect of secondary electrodes was observed for RGCs stimulated with pairs of electrodes spaced 30 μm apart. For RGCs stimulated with electrode pairs spaced 60 μm apart, however, there was a tendency for secondary electrodes located on the side of the RGC opposite the axon direction to have negative λ values (Fig. 3.10, 3.11), i.e., opposite polarity stimulation with these secondary electrodes tended to decrease activation thresholds rather than increase them.

To quantitatively describe the degree to which particular electrode pair orientations corresponded with particular modulatory effects, an index describing the anisotropy of the distribution of λ values as a function of angle between the axon and secondary electrode was calculated (see 3.2.13). Briefly, the λ values were

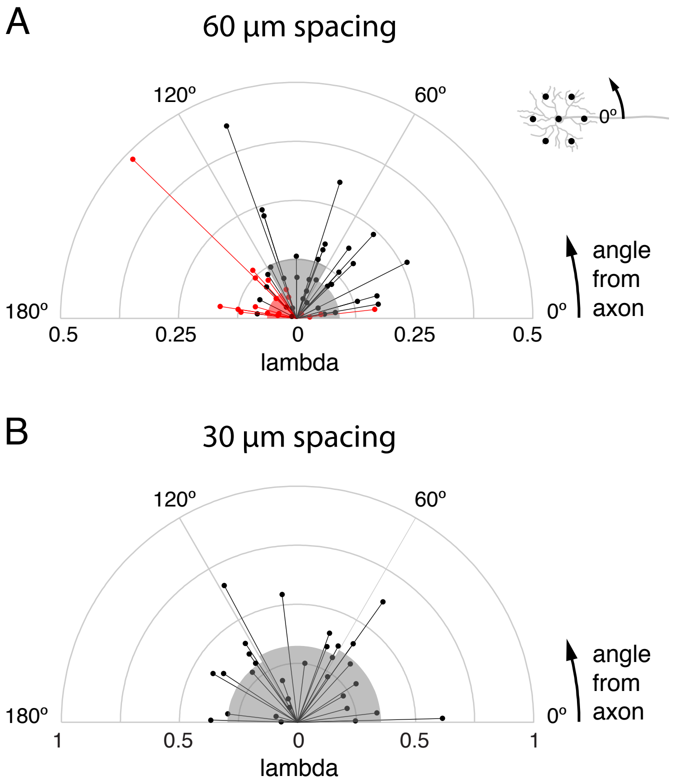

Figure 3.11: Correlation of modulatory effect with relative axon orientation. Modulatory effects (λ) of secondary electrodes observed for 60 μm electrode spacing (A) and 30μm electrode spacing (B), plotted in terms of the relative angle from the axon direction. Angles above 180° are reflected across the horizontal axis. Positive λ values are plotted in black and negative λ values are in red, with distance from the origin indicating the magnitude of the effect. Shaded regions indicate the average λ within each 60° bin.

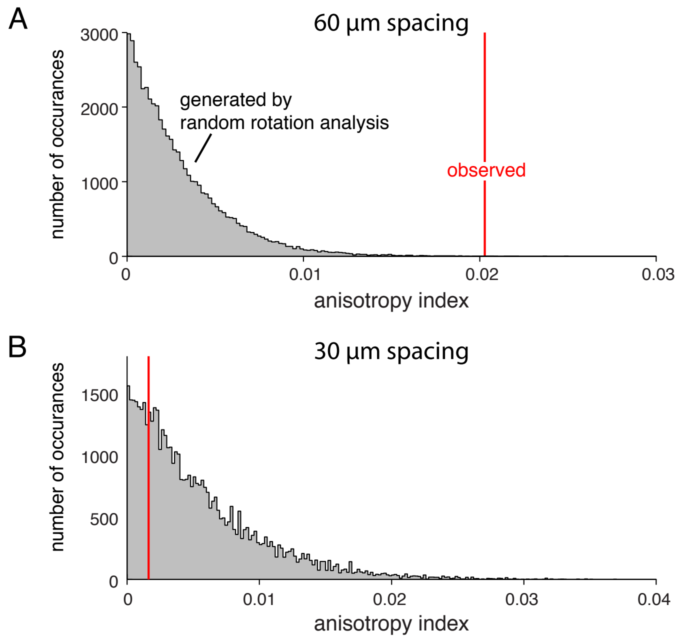

Figure 3.12: Significance of observed correlation between modulatory effect and relative axon orientation. Anisotropy index of observed modulatory effects (red) and distributions (grey) of anisotropy indices (grey) for 60 μm (A) and 30 μm (B) electrode spacing, generated from 50,000 random rotation iterations (see Section 3.2.13).

binned according to the angle between the axon and the corresponding secondary electrode. We defined the anisotropy index as the sum of the squared differences between the mean of the λ values falling in each bin ($\bar{\lambda_i}$) and the mean of λ values across all bins ($\bar{\lambda}$):

$$I_{anisotropy} = \sum_i \left(\bar{\lambda_i} - \bar{\lambda}\right) \tag{3.6}$$

The significance of the calculated anisotropy index was assessed using a random rotation analysis (see 3.2.13), in which the anisotropy index was recalculated after abolishing the relationship between axon orientation and secondary electrode by assigning a random axon angle to each cell. The anisotropy index of the original data was then compared to the distribution of anisotropy indices generated by 50,000 random rotation iterations (Fig. 3.11). This analysis revealed that the correlation between modulatory effect and relative axon orientation was significant for electrode pairs spaced 60 μm apart (p = 0.0028) but not for pairs spaced 30 μm apart (p = 0.7703).

3.4 Discussion

Our measurements show that a simple linear model accurately describes responses of individual RGCs to spatial patterns of current injection, and that these spatial patterns can be used to improve the selectivity of epiretinal stimulation.

3.4.1 Biophysical interpretation of linear modulatory effects

The mechanism by which extracellular current injection activates neurons has been investigated extensively using compartmental models of neurons placed in electric fields [33, 34]. The precise effect of extracellular stimulation on membrane potential at a particular location of a neuron is a complex function of electrode geometry, tissue electrical properties, pulse shape, neuron morphology, and membrane dynamics, and outside the scope of this discussion. However, valuable insight into the potential mechanisms underlying the effects of patterned electrical stimulation can be gained by considering the passive membrane response to the field generated by current injection.

The passive membrane response at any given location is a linear function of the extracellular voltage distribution along the neuron [33, 34]. Because the voltage at each position in space generated by particular pattern of current injection is a linear function of the amplitude of each current source (assuming constant tissue resistivity), the passive membrane response at any given location along the RGC is a linear function of the amplitude and polarity of the current pulse injected by each electrode in spatial pattern. Therefore, if spike initiation is approximated as occurring whenever the peak depolarization within the active region of the RGC (region of membrane capable of generating a spike) exceeds some particular threshold, the stimulus required to achieve this threshold will be a linear function of the current amplitudes on each electrode in the spatial pattern, as long as the location of the peak depolarization doesn't change.

If correct, this framework would explain the observed linear tradeoff between current amplitudes applied by different electrodes in a spatial pattern (Fig. 3.3, 3.7) within a particular region of stimulus space. In addition, the framework explains the potential cause for transitions between regions of stimulus space that can be fit by a single linear model (Fig. 3.5): when the current amplitude of a secondary electrode exceeds some critical value, the location of peak depolarization may change, resulting in a different linear tradeoff of the current amplitudes on spiking threshold (Fig. 3.13C vs. Fig. 3.13D). In effect, for any given region of stimulus space, one of the electrodes in the pattern appears to behave as the main driving force behind spike initiation, generating a large amount of depolarization at a particular location of the RGC. Current injected through other electrodes linearly modulates the depolarization at this location, which in turn linearly modulates the current amplitude of the main driving electrode required to initiate a spike. However, when current in one of the modulatory electrodes is sufficient to shift the site of activation, the tradeoff changes, resulting in a different relationship between current and threshold.

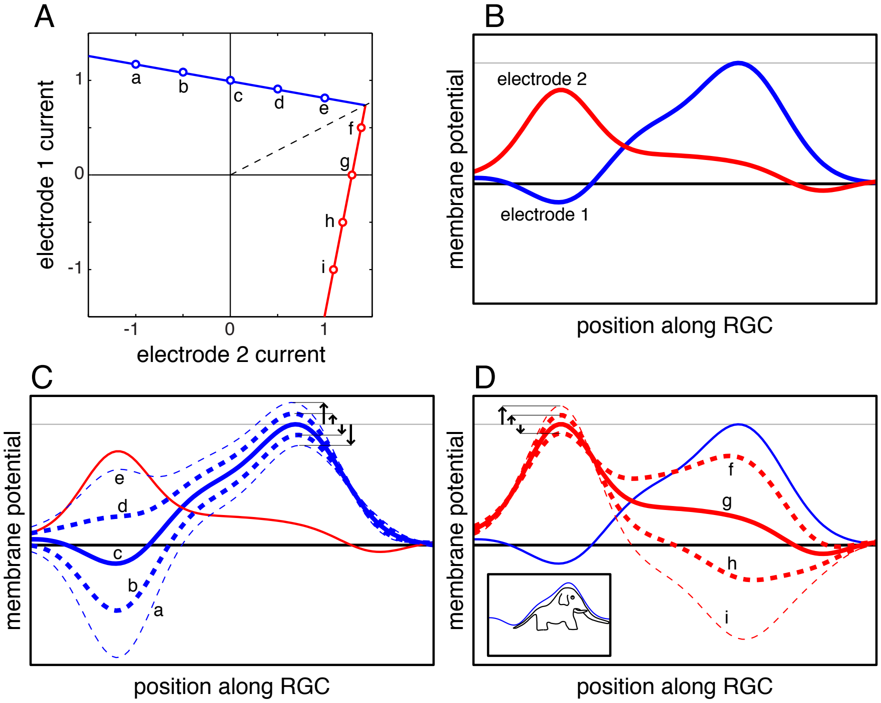

Figure 3.13: Biophysical interpretation of linear model. (A) A hypothetical example of threshold modulation using electrode pairs, including two regions of stimulus space in which different electrodes provide the main depolarizing "drive" for RGC activation. Open circles indicate threshold current amplitudes for a particular stimulus pattern, solid lines are linear fits to thresholds, and dashed line shows the boundary between regions of stimulus space. Lower-case letters indicate corresponding passive membrane responses in (C,D). (B) Hypothetical passive membrane response at the end of a current pulse of unit amplitude injected through electrode 1 (blue) or electrode 2 (red). Grey line indicates hypothetical depolarization threshold for spike initiation. (C) Passive membrane response to current pulse of unit amplitude through electrode 1 in combination with current pulses injected through electrode 2 at various amplitudes (blue solid and dashed): -1, -0.5, 0, 0.5, 1 for a, b, c, d, and e respectively. Response to electrode 2 alone is shown in red for comparison. Arrows indicate shift in peak depolarization, and corresponding shift in current required by electrode 1 to initiate a spike is shown by position of corresponding open circles in (A). (D) Passive membrane response to current pulse of fixed amplitude through electrode 2 in combination with current pulses injected through 1 at various amplitudes (red): 0.5, 0, -0.5, -1 for f, g, h, and i respectively. Response to a unit current injected through electrode 1 alone is shown in blue. Inset depicts an alternative interpretation of the cause of membrane potential fluctuation (adapted from [35]).

This framework also provides a potential reason for the observation of opposite sign modulatory effects, i.e., reduction of thresholds upon opposite polarity current injection rather than increase in threshold (Fig. 3.3F). Modeled responses of neurons to monopolar stimuli in a similar configuration to the single-electrode stimuli used in this study predict that a cathodal stimulus will cause depolarization in some regions and (typically weaker) hyperpolarization in other regions [31, 33, 34]. An opposite sign modulatory effect would be expected to occur if the region of membrane depolarized by a cathodal pulse injected through one electrode overlapped with the region of membrane that was hyperpolarized by a cathodal pulse injected through the other electrode (Fig. 3.13D).

3.4.2 General strategies for avoidance of axon stimulation

Stimulation of RGC axons is a major concern associated with the use of epiretinal prostheses because inadvertent stimulation of passing axons of distant RGCs would be expected to generate percepts in the region of visual space near the somas of the stimulated RGCs rather than (or in addition to) the region of visual space near the electrode. Comparisons of thresholds to electrodes placed near RGC somas and axons in *in vitro* models of epiretinal prostheses [36–40], as well as computational models [41, 42] suggest that while thresholds to axonal stimulation are typically higher than thresholds to stimulation near RGC somas (somatic stimulation), the threshold difference is small. These observations are further supported by the fact that stimulation of passing axons has been shown to preclude selective activation of individual RGCs in a primate model of epiretinal stimulation (see Section 2.3.4).

A study of axon stimulation in isolated rabbit retina has shown that bipolar stimuli applied by electrode pairs spaced 50 μm apart and in a bipolar transverse configuration (Fig. 3.14A) increase axonal thresholds relative to monopolar stimulation, while bipolar axial stimuli (Fig. 3.14B) with electrode pairs oriented along the axon have little effect relative to monopolar stimulation [29]. In another study, modeled responses of RGC axons showed decreased axon activation using elongated electrodes oriented parallel to axons in comparison to those oriented perpendicu-

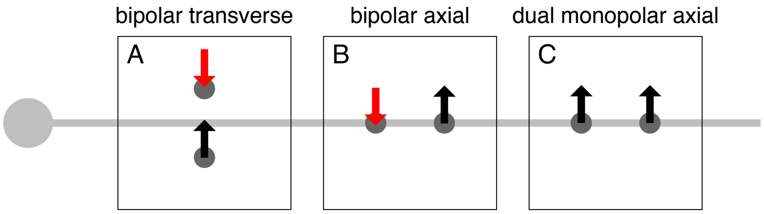

Figure 3.14: Schematic of paired-electrode pattern configurations of axonal stimulation. Horizontal grey bar depicts axon orientation relative to electrodes. Polarity of current is indicated by color and direction of arrows (cathodal in black, anodal in red).

lar to axons [30], suggesting that dual monopolar axial stimuli (Fig. 3.14C) may increase axon thresholds relative to monopolar stimulation.

Both the correlation between relative axon orientation and modulatory effects for electrodes spaced 60 μm apart (Fig. 3.11A) and the lack of correlation for electrodes spaced 30 μm apart (Fig. 3.11B) observed in this study of somatic stimulation suggest potential general strategies to reduce the inadvertent stimulation of bypassing axons in an epiretinal prosthesis. In the case of 30 μm separation, if dual monopolar axial stimulation generates similar results to those predicted in the model of RGC axon responses to elongated electrodes, these spatial patterns could elevate axonal thresholds relative to somatic thresholds. This is because, in contrast to the predicted effect on axonal thresholds, current patterns corresponding to this configuration (Fig. 3.11B, near 0° or 180°) tended to decrease somatic RGC thresholds.

In the case of 60 μm separation, the optimal general strategy for axon avoidance is less clear. While bipolar transverse stimuli tended to increase thresholds of both axons [29] and somas (Fig. 3.11A, near 90°), this stimulation configuration could improve the general selectivity for local RGCs over passing axons if the effect is significantly larger for axons than somas. Alternatively, because bipolar axial stimuli had little effect on axonal thresholds in comparison to monopolar stimuli in the previous rabbit studies, and this configuration tended to decrease somatic thresholds when applied distal to the RGC axon in this study (Fig. 3.11A, near 180°), bipolar axial stimuli may preferentially activate nearby RGCs with axons oriented away from the anodal electrode of the pair (secondary electrode in opposite polarity stimuli tested here).

Because the spacing of electrodes appears to have a large effect on the presence of correlations between axon orientation and effects of different stimulus pattern configurations (Fig. 3.11A vs. 3.11B), the best general strategy for axon avoidance will likely depend on the spacing of electrodes used in the clinical array. Future studies comparing the magnitude and sign of modulatory effects on axonal and somatic stimulation using the same electrode arrays should be performed to determine the best strategy and the expected level of improvement in axon avoidance for a particular electrode spacing.

3.4.3 Requirements for implementation in a retinal prosthesis

It is important to note that a number of technical changes would be required before the linear model proposed in this study could be used to improve stimulation selectivity in a clinical prosthesis. First, determination of model parameters requires the measurement of RGC responses to stimulation with pairs of electrodes. Currently used clinical epiretinal prosthesis do not have the recording capabilities required to measure RGC responses. In addition, an efficient algorithm for automated RGC response detection would be required to quickly extract response curves of each RGC for a large number of stimulus patterns. Second, electrode arrays must have significantly higher densities of electrodes than those currently in use in clinical devices. This is crucial not only for approaching single-cell resolution of electrical stimulation, but for sorting recorded RGC responses according to the cells that generated them. Third, the utility of fine spatial patterns of current injection is likely to require much closer contact between an electrode array and the retina than is achievable with the current method of fixing electrode arrays to the inner retinal surface using a scleral tack [5]. Any gap between the electrode array and retina would be expected to blur the pattern of current injection by providing a low resistance path for transverse current flow, reducing the ability of patterned stimulation to shape the electrical field generated in the retina. Fourth, the implant must be capable of simultaneously driving current pulses of different amplitudes through sets of electrodes. Finally, a simple algorithm is required to determine the stimulus pattern that optimizes selectivity of a target cell or set of cells.

Acknowledgments

This work would not have been possible without the invaluable contributions of my coauthors, including many associated with the Santa Cruz Institute for Particle Physics at the University of California, Santa Cruz. Of special note, Pawel Hottowy designed and tested the electrical stimulation system that was crucial for all of the data presented in this thesis, as well as the Labview software required to run the stimulation and recording system and the core Matlab software to read and sort the electrical stimulation data. In addition, Pawel helped to run several of the early experiments using the system, and has provided valuable input on experiment planning and analysis. Keith Mathieson and Debbie Gunning fabricated the electrode arrays used in all of the electrical stimulation experiments, helped to train me in the use of the stimulation system, helped to install and debug the stimulation system at the Salk Institute, and provided assistance in several experiments.

I would also like to acknowledge Matthew Grivich for software development; Clare Hulse for technical assistance and data analysis; Gaby Cruz for data analysis; Tomasz Fiutowski, Sergei Kachiguine, Andrzej Skoczen and Alexander Sher for technical development; Steve Barry for machining; and Howard Fox, Mike Taffe, Ed Callaway, John Reynolds, and Rich Krauzlis for access to primate retinas.

This work was supported by NEI Grant R01EY021271 (EJC, LHJ), a Sanofi-aventis Discovery Grant (EJC, LHJ), the Salk Institute for Biological Studies (EJC, LHJ), the Joseph Alexander Foundation (EJC, LHJ), the Charles Lee Powell Foundation (LHJ), NIH Grant R21-EB004410 (AL), NSF Grant PHY-0750525 (AL), the McKnight Foundation (EJC, AL), EPSRC Grant EP/E039731/1

(DEG), a Royal Society of Edinburgh fellowship (KM), a RCUK funded SU2P fellowship (KM), EPSRC Grant GR/R89189/01 (KM), and the Polish Ministry of Science and Higher Education (WD).

EJ Chichilnisky is on the scientific advisory boards of Pixium and Nanovision.

Chapter 3, in part, is a reprint, with permission, of the published conference proceedings "Spatially patterned electrical stimulation of the retina for improved specificity." Jepson L.H., Hottowy P., Gunning D.E., Mathieson K., Dabrowski W., Litke A., and Chichilnisky, E.J. *Proceedings of the 5th International IEEE/EMBS Conference on Neural Engineering*, 2011 ©IEEE 2011. The dissertation author was the primary investigator and author of this paper.

Chapter 3, in part, is currently being prepared for submission for publication of the material. Jepson L.H., Hottowy P., Mathieson K., Gunning D.E., Dabrowski W., Litke A., Chichilnisky, E.J. The dissertation author was the primary investigator and author of this material.

3.5 References

[1] Rodieck, R., 1998. The first steps in seeing. Sinauer, Sunderland, MA.

[2] Dagnelie, G., 2012. Retinal implants: emergence of a multidisciplinary field. *Curr Opin Neurol*, 25:67–75.

[3] Fornos, A., Sommerhalder, J., Cruz, L.D., Sahel, J., Mohand-Said, S., Hafezi, F., and Pelizzone, M., 2012. Temporal Properties of Visual Perception on Electrical Stimulation of the Retina. *Investigative Ophthalmology & Visual Science*, 53:2720–2731.

[4] Klauke, S., Goertz, M., Rein, S., Hoehl, D., Thomas, U., Eckhorn, R., Bremmer, F., and Wachtler, T., 2011. Stimulation with a wireless intraocular epiretinal implant elicits visual percepts in blind humans. *Investigative Ophthalmology & Visual Science*, 52:449–455.

[5] de Balthasar, C., Patel, S., Roy, A., Freda, R., Greenwald, S., Horsager, A., Mahadevappa, M., Yanai, D., McMahon, M., Humayun, M., Greenberg, R.,

Weiland, J., and Fine, I., 2008. Factors affecting perceptual thresholds in epiretinal prostheses. *Invest Ophthalmol Vis Sci*, 49:2303–2314.

[6] Hodgins, D., Bertsch, A., Post, N., Frischholz, M., Volckaerts, B., Spensley, J., Wasikiewicz, J., Higgins, H., von Stetten, F., and Kenney, L., 2008. Healthy Aims: Developing New Medical Implants and Diagnostic Equipment. *IEEE Pervasive Computing*, 7:14–21.

[7] Field, G. and Chichilnisky, E., 2007. Information processing in the primate retina: circuitry and coding. *Annu Rev Neurosci*, 30:1–30.

[8] Nanduri, D., Humayun, M., Greenberg, R., McMahon, M., and Weiland, J., 2008. Retinal prosthesis phosphene shape analysis. *Conf Proc IEEE Eng Med Biol Soc*, pages 1785–1788.

[9] Nanduri, D., Fine, I., Horsager, A., Boynton, G., Humayun, M., Greenberg, R., and Weiland, J., 2012. Frequency and amplitude modulation have different effects on the percepts elicited by retinal stimulation. *Invest Ophthalmol Vis Sci*, 53:205–214.

[10] Caspi, A., Dorn, J., McClure, K., Humayun, M., Greenberg, R., and McMahon, M., 2009. Feasibility study of a retinal prosthesis: spatial vision with a 16-electrode implant. *Arch Ophthalmol*, 127:398–401.

[11] Yanai, D., Weiland, J., Mahadevappa, M., Greenberg, R., Fine, I., and Humayun, M., 2007. Visual performance using a retinal prosthesis in three subjects with retinitis pigmentosa. *Am J Ophthalmol*, 143:820–827.

[12] Richard, G., Keserue, M., Feucht, M., Post, N., and Hornig, R., 2008. Visual Perception After Long-Term Implantation of a Retinal Implant. *ARVO Meeting Abstracts*, 49:1786.

[13] Ahuja, A., Dorn, J., Caspi, A., McMahon, M., Dagnelie, G., Dacruz, L., Stanga, P., Humayun, M., and Greenberg, R., 2011. Blind subjects implanted with the Argus II retinal prosthesis are able to improve performance in a spatial-motor task. *Br J Ophthalmol*, 95:539–543.

[14] Humayun, M., Dorn, J., da Cruz, L., Dagnelie, G., Sahel, J., Stanga, P., Cideciyan, A., Duncan, J., Eliott, D., Filley, E., Ho, A.C., Santos, A., Safran, A., Arditi, A., Del Priore, L., and Greenberg, R., 2012. Interim results from the international trial of Second Sight's visual prosthesis. *Ophthalmology*, 119:779–788.

[15] Bonham, B. and Litvak, L., 2008. Current focusing and steering: modeling, physiology, and psychophysics. *Hear Res*, 242:141–153.

[16] Townshend, B. and White, R., 1987. Reduction of electrical interaction in auditory prostheses. *IEEE Trans Biomed Eng*, 34:891–897.

[17] Butson, C. and McIntyre, C., 2008. Current steering to control the volume of tissue activated during deep brain stimulation. *Brain Stimul*, 1:7–15.

[18] Martens, H., Toader, E., Decre, M., Anderson, D., Vetter, R., Kipke, D., Baker, K., Johnson, M., and Vitek, J., 2011. Spatial steering of deep brain stimulation volumes using a novel lead design. *Clin Neurophysiol*, 122:558–566.

[19] Field, G., Sher, A., Gauthier, J., Greschner, M., Shlens, J., Litke, A., and Chichilnisky, E., 2007. Spatial properties and functional organization of small bistratified ganglion cells in primate retina. *J Neurosci*, 27:13261–13272.

[20] Sekirnjak, C., Hottowy, P., Sher, A., Dabrowski, W., Litke, A., and Chichilnisky, E., 2008. High-resolution electrical stimulation of primate retina for epiretinal implant design. *J Neurosci*, 28:4446–4456.

[21] Hottowy, P., Dabrowski, W., Skoczen, A., and Wiacek, P., 2008. An integrated multichannel waveform generator for large-scale spatio-temporal stimulation of neural tissue. *Analog Integrated Circuits and Signal Processing*, 55:239–248.

[22] Litke, A., 1998. The retinal readout system: an application of microstrip detector technology to neurobiology. *Nucl Instrum Methods Phys Res A*, 418:203–209.

[23] Litke, A., Chichilnisky, E., Dabrowski, W., Grillo, A., Grybos, P., Kachiguine, S., Rahman, M., and Taylor, G., 2003. Large-scale imaging of retinal output activity. *Nucl Instr and Meth A*, 501:298–307.

[24] Sekirnjak, C., Hottowy, P., Sher, A., Dabrowski, W., Litke, A., and Chichilnisky, E., 2006. Electrical stimulation of mammalian retinal ganglion cells with multielectrode arrays. *J Neurophysiol*, 95:3311–3327.

[25] Hottowy, P., Beggs, J., Chichilnisky, E., Dabrowski, W., Fiutowski, T., Gunning, D., Hobbs, J., Jepson, L., Kachiguine, S., Mathieson, K., Rydygier, P., Sher, A., Skoczen, A., and Litke, A., 2010. 512-electrode MEA System For Spatio-Temporal Distributed Stimulation and Recording of Neural Activity. *7th Int Meeting on Substrate-Integrated Microelectrode Arrays*, pages 327–330.

[26] Chichilnisky, E., 2001. A simple white noise analysis of neuronal light responses. *Network: Computation in Neural Systems*, 12:199–213.

[27] Litke, A., Bezayiff, N., Chichilnisky, E., Cunningham, W., Dabrowski, W., Grillo, A., Grivich, M., Grybos, P., Hottowy, P., Kachiguine, S., Kalmar, R.,

Mathieson, K., Petrusca, D., Rahman, M., and Sher, A., 2004. What does the eye tell the brain? Development of a system for the large scale recording of retinal output activity. *IEEE Trans Nucl Sci*, 51:1434–1440.

[28] Petrusca, D., Grivich, M., Sher, A., Field, G., Gauthier, J., Greschner, M., Shlens, J., Chichilnisky, E., and Litke, A., 2007. Identification and characterization of a Y-like primate retinal ganglion cell type. *J Neurosci*, 27:11019–11027.

[29] Grumet, A.E., 1999. Electric stimulation parameters for an epi-retinal prosthesis. Ph.D. thesis, Massachusetts Institute Of Technology, Cambridge, MA.

[30] Rattay, F. and Resatz, S., 2004. Effective electrode configuration for selective stimulation with inner eye prostheses. *IEEE Trans Biomed Eng*, 51:1659–1664.

[31] Rattay, F. and Resatz, S., 2007. Dipole distance for minimum threshold current to stimulate unmyelinated axons with microelectrodes. *IEEE Trans Biomed Eng*, 54:158–162.

[32] Fried, S., Lasker, A., Desai, N., Eddington, D., and Rizzo, J.r., 2009. Axonal sodium-channel bands shape the response to electric stimulation in retinal ganglion cells. *J Neurophysiol*, 101:1972–1987.

[33] McIntyre, C. and Grill, W., 1999. Excitation of central nervous system neurons by nonuniform electric fields. *Biophys J*, 76:878–888.

[34] Rattay, F., 1999. The basic mechanism for the electrical stimulation of the nervous system. *Neuroscience*, 89:335–346.

[35] de Saint Exupery, A., 1943. The Little Prince, trans. Reynal & Hitchcock, New York.

[36] Behrend, M., Ahuja, A., Humayun, M., Chow, R., and Weiland, J., 2011. Resolution of the epiretinal prosthesis is not limited by electrode size. *IEEE Trans Neural Syst Rehabil Eng*, 19:436–442.

[37] Behrend, M., Ahuja, A., Humayun, M., Weiland, J., and Chow, R., 2009. Selective labeling of retinal ganglion cells with calcium indicators by retrograde loading in vitro. *J Neurosci Methods*, 179:166–172.

[38] Jensen, R.J., Rizzo, J.F., Ziv, O.R., Grumet, A., and Wyatt, J., 2003. Thresholds for activation of rabbit retinal ganglion cells with an ultrafine, extracellular microelectrode. *Invest Ophthalmol Vis Sci*, 44:3533–3543.

[39] Jensen, R.J., Ziv, O.R., and Rizzo, J.F., 2005. Thresholds for activation of rabbit retinal ganglion cells with relatively large, extracellular microelectrodes. *Invest Ophthalmol Vis Sci*, 46:1486–1496.

[40] Freeman, D., Eddington, D., Rizzo, J.r., and Fried, S., 2010. Selective activation of neuronal targets with sinusoidal electric stimulation. *J Neurophysiol*, 104:2778–2791.

[41] Greenberg, R.J., Velte, T.J., Humayun, M.S., Scarlatis, G., and de Juan, E., 1999. A computational model of electrical stimulation of the retinal ganglion cell. *IEEE Trans Biomed Eng*, 46:505–514.

[42] Schiefer, M. and Grill, W., 2006. Sites of neuronal excitation by epiretinal electrical stimulation. *IEEE Trans Neural Syst Rehabil Eng*, 14:5–13.

Chapter 4

Future Work

There are a number of potential extensions to the research presented in this thesis.

4.1 Axon stimulation

The stimulation of bypassing axons is one of the major concerns associated with the epiretinal stimulation approach. Previous *in vitro* [1–5] and computational studies [6, 7], along with the analysis of selectivity described in Section 2.3.4, have shown that axon stimulation is likely to significantly reduce the spatial selectivity achievable with single-electrode epiretinal stimulation. Several questions remain regarding that degree of inadvertent axon stimulation that occurs *in vivo* and potential strategies to avoid axon stimulation.

4.1.1 Thresholds vs. distance from soma

It is currently unclear whether there is a systematic change in axon activation threshold as a function of distance from the soma. In the work presented in this thesis, the region of retina that could be analyzed was limited to ∼500 μm in diameter. Therefore, it was impossible to determine whether axon stimulation thresholds change at distances beyond 500 μm from the RGC soma. This is of interest to retinal prosthesis design, because it influences the expected distance of potentially activated cells from the location of current injection, and could provide an estimate of the degree of unobserved axon stimulation that may be occurring in *in vitro* experiments with limited recording areas.

This issue could be addressed by performing electrical stimulation experiments using more extensive electrode arrays. An electrical stimulation system identical to the one used here, but with 512 electrodes and capable of recording from a ∼1 x 2 mm region of retina, has been developed and tested [8]. This stimulation system would allow for measurement of axon activation thresholds at distances sufficient to determine whether stimulation of the axons of distant RGCs is likely to occur upon epiretinal electrical stimulation.

4.1.2 Linear model and electrode pair orientation

Previous modeling [9] and experimental work [10, 11] suggest that oriented electric fields could be used to reduce activation of bypassing axons (see Section 3.4.2). These observations point toward multielectrode stimulation strategies that could elevate axon activation thresholds relative to near-soma activation thresholds. It is currently unclear, however, whether the magnitude of the orientation effects will be sufficiently different for axonal and near-somatic stimulation to provide a blanket strategy to reduce unwanted axon stimulation. In addition, it is unclear how dependent such axon stimulation effects will be on electrode spacing.

To determine whether oriented paired-electrode stimuli could sufficiently elevate axon stimulation thresholds relative to somatic stimulation thresholds, responses of RGCs to stimulation near axons and somas to electrode pairs with different polarity combinations should be performed using identical electrode arrays (see Fig. 4.1 for preliminary results). The dependence of paired electrode stimulation on relative axon orientation could then be analyzed in both cases, revealing whether any particular orientation and polarity combination would lead to greater selectivity of somas over axons for a particular electrode spacing.

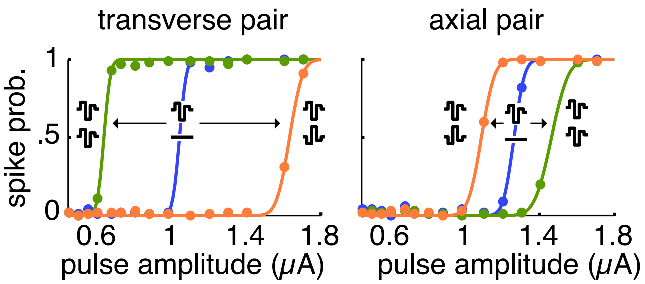

Figure 4.1: Example of axonal stimulation threshold shifts from paired-electrode stimulation. Stimulation of a rat RGC axon was performed with different combinations of pulse polarities on a pair of electrodes spaced 60 μm apart and oriented roughly perpendicular to the axon (left) or parallel to the axon (right). Blue curves indicate responses to stimulation with the single electrode of the pair that resulted in the lower threshold. Same-polarity stimulation (green) decreased threshold for the transverse electrode pair and increased threshold for the axial electrode pair, while opposite-polarity stimulation (orange) had the opposite effect for the respective electrode pair orientations.

4.2 Spatial selectivity

4.2.1 Array density

The spatial selectivity analysis presented in this dissertation (Section 2.3.4) was performed using arrays with 60 μm electrode spacing. Higher density arrays would be expected to achieve greater spatial selectivity, but it is unclear how much of an improvement would be possible. For example, the existence of RGCs with low thresholds and broad spatial regions of sensitivity to electric stimulation would make it difficult to achieve single-cell selectivity of nearby RGCs with higher thresholds, even using arrays with much higher electrode density. This question could be addressed by performing a similar selectivity analysis with higher density arrays.

4.2.2 Eccentricity

Spatial selectivity has thus far only been analyzed in the peripheral retina, where RGC density is relatively low. However, retinal prostheses are typically implanted in the central retina, which has much higher RGC density [12, 13]. As a result, the spatial selectivity achievable with electrical stimulation would be expected to be lower in the central retina. Future experiments at a range of eccentricities could be performed with a constant electrode density to determine the magnitude of this effect. In addition, selectivity at different eccentricities using arrays with different electrode densities would allow one to determine whether these increases in cell density could be simply compensated for with a matched increase in electrode density.

4.3 Further testing of piecewise linearity

The piecewise linearity observed for electrode pairs (Section 3.3.3) could only be tested in a small subset of the total number of electrode pairs. This was likely the result of only testing a limited range of relative current amplitudes on the primary and secondary electrodes. A larger range of relative amplitudes should be tested, including combinations with cathodal-anodal-cathodal current pulses applied by the primary electrode, to determine whether the piecewise linearity truly describes the responses of RGCs over the full stimulus space.

4.4 Cell type classification in the absence of visual responses

One of the primary motivations for achieving single-cell spatial resolution is to allow for independent control of different RGC types. Before each RGC can be activated in a way that generates the spiking responses appropriate for its type, however, the prosthesis must be able to determine the type of each targeted RGC. In this dissertation work, RGC types were determined using the visual response properties of the recorded cells (see Section 2.3.1). These measurements would be impossible in a degenerate retina, which lacks visual responses altogether. Therefore, an alternative method for cell type classification based on other cell type-specific properties is required.

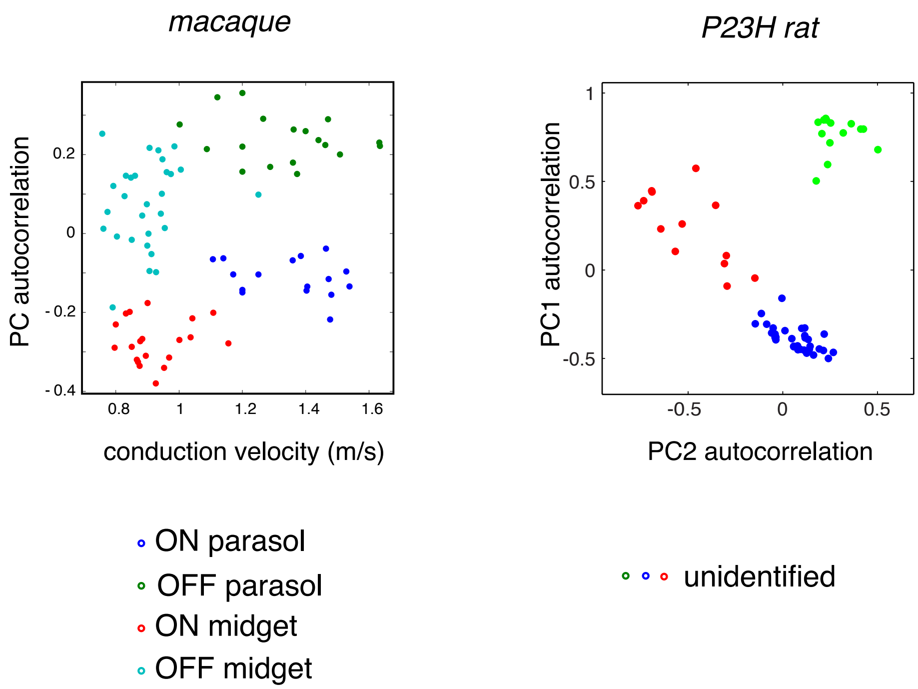

Figure 4.2: Cell type classification in the absence of visual response properties. Retinal ganglion cells in a single macaque retina preparation (left) are plotted as a function of two intrinsic RGC properties: the first principal component of the spontaneous spike train autocorrelation and the axon conduction velocity. Points are colored according to known cell types, based on measured light response properties. Clustering of points corresponding to different cell types indicates that intrinsic properties could be used as an alternative method for cell type classification. Retinal ganglion cells in a degenerated rat preparation (P23H, right) show similar clustering when plotted in terms of the first two principal components of the spike train autocorrelations, suggesting that intrinsic RGC properties might provide a cell type identification method in degenerate retina. Points are colored according to tentative cell types.

Preliminary work suggests that non-visual characteristics that reflect the intrinsic membrane properties of RGCs, such as the temporal structure of spontaneous spike sequences and the shapes of recorded spike waveforms, may be used to separate recorded RGCs into different cell types (see Fig. 4.2). Further work is required to determine which characteristics are optimal for this task and whether this strategy could be used to consistently identify cell types across different retinal preparations. Because spiking patterns have been shown to change during the course of retinal degeneration in several animal models [14–22], cell-type classification should also be tested in a model of retinal degeneration to see whether these changes preclude the use of this strategy.

Acknowledgments

I would like to acknowledge current and former members of the Systems Neurobiology Laboratories, EJ Chichilnisky lab at the Salk Institute for Biological studies for data used to generate Fig. 4.2, and Martin Greschner for assistance in generating it.

4.5 References

[1] Behrend, M., Ahuja, A., Humayun, M., Chow, R., and Weiland, J., 2011. Resolution of the epiretinal prosthesis is not limited by electrode size. *IEEE Trans Neural Syst Rehabil Eng*, 19:436–442.

[2] Behrend, M., Ahuja, A., Humayun, M., Weiland, J., and Chow, R., 2009. Selective labeling of retinal ganglion cells with calcium indicators by retrograde loading in vitro. *J Neurosci Methods*, 179:166–172.

[3] Jensen, R.J., Rizzo, J.F., Ziv, O.R., Grumet, A., and Wyatt, J., 2003. Thresholds for activation of rabbit retinal ganglion cells with an ultrafine, extracellular microelectrode. *Invest Ophthalmol Vis Sci*, 44:3533–3543.

[4] Jensen, R.J., Ziv, O.R., and Rizzo, J.F., 2005. Thresholds for activation of rabbit retinal ganglion cells with relatively large, extracellular microelectrodes. *Invest Ophthalmol Vis Sci*, 46:1486–1496.

[5] Freeman, D., Eddington, D., Rizzo, J.r., and Fried, S., 2010. Selective activation of neuronal targets with sinusoidal electric stimulation. *J Neurophysiol*, 104:2778–2791.

[6] Greenberg, R.J., Velte, T.J., Humayun, M.S., Scarlatis, G., and de Juan, E., 1999. A computational model of electrical stimulation of the retinal ganglion cell. *IEEE Trans Biomed Eng*, 46:505–514.

[7] Schiefer, M. and Grill, W., 2006. Sites of neuronal excitation by epiretinal electrical stimulation. *IEEE Trans Neural Syst Rehabil Eng*, 14:5–13.

[8] Hottowy, P., Beggs, J., Chichilnisky, E., Dabrowski, W., Fiutowski, T., Gunning, D., Hobbs, J., Jepson, L., Kachiguine, S., Mathieson, K., Rydygier, P., Sher, A., Skoczen, A., and Litke, A., 2010. 512-electrode MEA System For Spatio-Temporal Distributed Stimulation and Recording of Neural Activity. *7th Int Meeting on Substrate-Integrated Microelectrode Arrays*, pages 327–330.

[9] Rattay, F. and Resatz, S., 2004. Effective electrode configuration for selective stimulation with inner eye prostheses. *IEEE Trans Biomed Eng*, 51:1659–1664.

[10] Grumet, A.E., 1999. Electric stimulation parameters for an epi-retinal prosthesis. Ph.D. thesis, Massachusetts Institute Of Technology, Cambridge, MA.

[11] Grumet, A.E., Wyatt, J. L., J., and Rizzo, J.F., 2000. Multi-electrode stimulation and recording in the isolated retina. *J Neurosci Methods*, 101:31–42.

[12] Rodieck, R., 1998. The first steps in seeing. Sinauer, Sunderland, MA.

[13] Dacey, D., 2004. Origins of perception: retinal ganglion cell diversity and the creation of parallel visual pathways. In M.S. Gazzaniga, editor, The Cognitive Neurosciences, pages 281–301. MIT Press, Cambridge, MA.

[14] Margolis, D., Newkirk, G., Euler, T., and Detwiler, P., 2008. Functional stability of retinal ganglion cells after degeneration-induced changes in synaptic input. *J Neurosci*, 28:6526–6536.

[15] Margolis, D. and Detwiler, P., 2011. Cellular origin of spontaneous ganglion cell spike activity in animal models of retinitis pigmentosa. *J Ophthalmol*, 2011.

[16] Borowska, J., Trenholm, S., and Awatramani, G., 2011. An intrinsic neural oscillator in the degenerating mouse retina. *J Neurosci*, 31:5000–5012.

[17] Stasheff, S., 2008. Emergence of sustained spontaneous hyperactivity and temporary preservation of OFF responses in ganglion cells of the retinal degeneration (rd1) mouse. *J Neurophysiol*, 99:1408–1421.

[18] Stasheff, S.F. and Andrews, M.P., 2010. A Subpopulation of Retinal Ganglion Cells Sustains Spontaneous Hyperactivity Through Non-Synaptic Mechanisms in Mice With Retinal Degeneration. *ARVO Meeting Abstracts*, 51:5798.

[19] Sekirnjak, C., Jepson, L., Hottowy, P., Sher, A., Dabrowski, W., Litke, A., and Chichilnisky, E., 2011. Changes in physiological properties of rat ganglion cells during retinal degeneration. *J Neurophysiol*, 105:2560–2571.

[20] Goo, Y., Ye, J., Lee, S., Nam, Y., Ryu, S., and Kim, K., 2011. Retinal ganglion cell responses to voltage and current stimulation in wild-type and rd1 mouse retinas. *J Neural Eng*, 8:035003.

[21] Pu, M., Xu, L., and Zhang, H., 2006. Visual response properties of retinal ganglion cells in the royal college of surgeons dystrophic rat. *Invest Ophthalmol Vis Sci*, 47:3579–3585.

[22] Kolomiets, B., Simonutti, M., Sahel, J.A., and Picaud, S., 2008. Functional Properties of Retinal Ganglion Cells in P23H Homozygote Rat Model of Retinitis Pigmentosa During Photoreceptor Degeneration. *6th International Meeting on Substrate-Integrated Micro Electrode Arrays*, page 203.